Self-Standing Silicon Nanostructures Fabricated Using Chemical/Electrochemical Technique: Application in Gas Field Ionization Tunneling Sensor

Parsoua Abedini Sohi

A Thesis
In the Department
of
Electrical and Computer Engineering

Presented in Partial Fulfillment of the Requirements
For the Degree of
Doctor of Philosophy (Electrical and Computer Engineering) at
Concordia University
Montreal, Quebec, Canada

February 2019

CONCORDIA UNIVERSITY

SCHOOL OF GRADUATE STUDIES

This is to certify that the thesis prepared

By: Parsoua Abedini Sohi

Entitled: Self-Standing Silicon Nanostructures Fabricated Using Chemical/Electrochemical Technique: Application in Gas Field Ionization Tunneling Sensor

and submitted in partial fulfillment of the requirements for the degree of

Doctor Of Philosophy (Electrical and Computer Engineering)

complies with the regulations of the University and meets the accepted standards with respect to originality and quality.

Signed by the final examining committee:

_____ Chair
Dr. Ciprian Alecsandru

_____ External Examiner
Dr. Kamal Al-Haddad

_____ External to Program
Dr. Javad Dargahi

_____ Examiner
Dr. Asim Al-Khalili

_____ Examiner
Dr. Irina Stateikina

_____ Thesis Supervisor
Dr. Mojtaba Kahrizi

Approved by

Dr. Mustafa K. Mehmet Ali, Graduate Program Director

April 5, 2019 _____

Dr. Amir Asif, Dean
Gina Cody School of Engineering & Computer Science

Abstract

Self-Standing Silicon Nanostructures Fabricated Using Chemical/Electrochemical Technique: Application in Gas Field Ionization Tunneling Sensor

Parsoua Abedini Sohi, Ph.D.
Concordia University, 2019

The air surrounding us may contain different amount of hazardous gases or atmospheric pollutants. As the public health and safety is the prime priority, therefore it is very essential to have a reliable detector to distinguish the presence of these pollutions.

So far, different gas sensing technologies have been invented. However none of the traditional sensors, which are mostly based on chemical reaction between the gas and detector material, could fulfill all the requirements such as sensitivity, selectivity, reversibility, durability and fast recovery time. Therefore, it is worth investigating contemporary sensors for the detection of different target gases. An ingenious approach would be to use the ionization characteristics of distinct gases to uniquely identify the gas type. Gas ionization sensors contain two parallel electrodes separated by a narrow gap. Applied electric field between the electrodes ionizes the target gas. Ionization energy is a unique amount of energy required for the gaseous atoms to discharge electrons. In these sensors the discharge characteristics are used as a calibrating data, which provides excellent selectivity. In addition, because this technique does not involve adsorption or desorption of the gases, the sensor exhibits fast response and high reversibility and recovery. In planar parallel electrode structures the applied electric field is uniform. Applying nanostructures as one of the electrodes creates nonlinear electric field, enhanced at the vicinity of the tips of the structures. In these structures the ionization initiates at lower voltages.

There are two different types of gas ionization sensors. One is based on measuring the breakdown voltages of the gases, which is extensively discussed in the literature. The second one is an innovative concept for nanostructure-based gas ionization sensors. These devices, which are studied in this work, is based on tunneling field ionization characteristics of the gases. In this phenomenon an electron from the gas tunnels into the vacant energy levels of a semiconductor employed as the anode.

The fabrication technique of the anode involves the growth of p-type silicon nanostructures through a mask-less chemical/electrochemical etching technique. The technique and the fabrication of the silicon nanowires used in the structure of the device are described in detail. Prior to the fabrication process, the mechanism of nanowires formations was modeled for 2D and 3D structures and simulated using COMSOL multiphysics. Our studies showed that the positive carriers (holes) current greatly influences the etching rate of the silicon during the electrochemical etching process. Our experiments showed that growth process of the nanostructures fits very well with our analytical model and helped us to adjust the fabrication parameters to control the characteristic as well as the density and concentration of the nanostructure arrays.

Finally, a miniaturized gas sensors based on the grown nanostructured was fabricated. I-V characteristics of the sensor was measured for various gases like Ar, N_2, O_2, and He. Charge transport mechanisms are explained based upon the gathered data.

The sensor was tested for 200 μm and 50 μm inter-electrode distances. Charge transport mechanism is explained based upon the gathered data for both devices. The fabricated devices are capable to characterize several gas species including inert gases. Gas ionization voltages were much lower compared to those, reported in the literature using devices fabricated by metallic nanostructures.

Acknowledgements

I would first like to express my sincere gratitude to my supervisor Dr. Mojtaba Kahrizi. His guidance and supports were not merely limited to my graduate studies. He steered me in the right direction whenever/wherever he thought I needed it. He is my life-coach and I owe it all to him.

I would also like to thank the supervisory committee who were involved in the validation of this research project through their invaluable constructive criticism, feedbacks and comments during the project.

I have enjoyed the company of my colleagues in "Solid-state Devices" group, Navjot, Kaveh, Salman and Mehrnegar. I wish to thank them all for their friendship and support. Furthermore, I would like to thank Mahsa Moosavi for her valuable suggestions and assistance during the process of defense.

Finally, I must express my very profound gratitude to my dear husband, Nima, for providing me with unfailing support and continuous encouragement throughout my years of study and through the process of researching and writing this thesis. Definitely, this accomplishment would not have been possible without him.

To Nima

TABLE OF CONTENTS

LIST OF FIGURES

LIST OF TABLES

LIST OF ACRONYMS

AAO	Anodized Aluminum Oxide
ATR	Attenuated Total Reflection
CNT	Carbon Nanotubes
DC	Direct Current
DFB	Distributed Feedback Laser
DI	Deionized
FI	Field Ionization
FE	Field Emission
GIS	Gas Ionization Sensor
GFIS	Gas Field Ionization Sensor
GFITS	Gas Field Ionization Tunneling Sensor
GFIBS	Gas Field Ionization Breakdown Sensor
HDL	Helmholtz Double Layer
IBE	Ion Bombardment Etching
LED	Light Emitting Diode
MWCNT	Multi-Walled Carbon Nanotube
NW	Nanowire
PAA	Porous Anodic Alumina
ppm	Particle per million
PE	Plasma Etching
PS	Porous silicon
SEM	Scanning Electron Microscope
SMU	Source Measurement Unit
SPP	Surface Plasmon Polariton
SPR	Surface Plasmon Resonance
TIR	Total internal reflection
US	Ultra Sonicator
VLS	Vapor-Liquid-Solid

LIST OF SYMBOLS

α	Townsend's primary ionization coefficient	[cm^{-1}]
β	Geometrical field enhancement factor	------
ϕ	Work function	[eV]
ϕ_s	Surface band bending	[eV]
χ	Electron affinity	[eV]
γ	Townsend's third ionization factor	------
λ	Wavelength	[m]
n_{metal}	Refractive index of metal	------
n	Refractive index of material	------
E	Electric field	[Vcm^{-1}]
E_{app}	Applied electric field	[Vcm^{-1}]
E_{loc}	Local electric field at the sharp tips	[Vcm^{-1}]
E_F	Fermi energy	[eV]
E_C	Minimum energy level of the conduction band	[eV]
E_V	Maximum energy level of the valence band	[eV]
x_c	Tunneling critical distance	[cm]
q	Electron Charge	[C]
n_e, n_i	Concentration of electrons and ions	[cm^{-3}]
μ_e, μ_i	Electron and ion mobility	[$cm^2V^{-1}s^{-1}$]
U_I	Ionization Potential	[eV]
k_x	Wave vector at x direction	[m^{-1}]
k_{sp}	Wave vector of surface plasmon	[m^{-1}]

Chapter 1
Introduction

1.1 Classification of Gas Sensing Methods

There are several natural and artificial chemical species in the air, some of which are toxic and combustible gases, which can be considered as potential hazard to the health [1], [2]. Gas sensors helps to prevent these hazards and play an important role in places with the risk of potentially harmful substances specifically in industrial processes and manufacturing plants.

According to the principal of the operation, gas sensor devices can be classified into two distinct categories: chemical gas sensors and physical gas sensors. Merely, considering electrical transduction mechanism, chemical gas sensors are based on chemical reaction between gas and sensing materials, resulting in change of conductivity of the detector material. In this method gases in different combinations could produce the same net-change in conductance and as a result, distinguishing between a gas and its mixtures is impossible. These types of sensors are very sensitive to changes in moisture, temperature and gas pressure. Their other drawback is that chemical reactions could cause irreversible changes in detector materials [3].

Physical type sensors have overcome the disadvantages of chemical type sensors. The following section describes several transduction-based physical type gas sensors and the mechanism of their operation in detail.

1.2 An overview of transduction-based physical gas sensors

1.2.1 Surface Plasmon Resonance based gas sensors

Surface plasmon polaritons (SPP) are electromagnetic waves that propagate at the interface of a metal and dielectric. The excitation of SPP is known as surface plasmon resonance (SPR). By solving Maxwell equations it is found that these resonant oscillations are supported at the interface between the materials with positive dielectric constant and the materials with negative dielectric constants such as gold (Au), Silver (Ag) and aluminum (Al) [4], [5].

To excite SPP, the wave vector of the electric field at the interface ($\mathbf{k}_x$) should be along the direction of wave vector of the surface plasmon ($\mathbf{k}_{sp}$). In the other word, at resonance condition, the frequency of the incident light matches the frequency of the oscillations of the electrons at the metal surface [6]. To match the wave vectors (k_x and k_{sp}) a special arrangement is required. Kretschmann configuration [7] is the most suitable setup to study the profile of plasmon modes. This configuration is shown in figure 1.1. To excite SPP, it is needed to have a component of electric field at the metal-dielectric interface. If the light traveling inside the prism is incident to metal layer and undergo a total internal reflection[1] (TIR), evanescent waves are formed in the metal layer. To ensure that the evanescent wave reaches the metal-dielectric boundary and couple to a surface plasmon mode, the thickness of the metal layer should be in range of few tens of nanometer. Figure 1.1 shows the coupling of the oscillations at the metal-dielectric interface.

At resonance condition the plasmon wave is generated due to the absorbance of photon energy by metal layer. Consequently, the intensity of reflected light reduces significantly at resonance response curves. The resonance condition is studied based on either angle or wavelength of the incident beam [4].

[1] TIR occurs when incident angle θ_i is greater than the critical angle θ_c. θ_c is the angle of incidence for which the reflection angle is 90º.

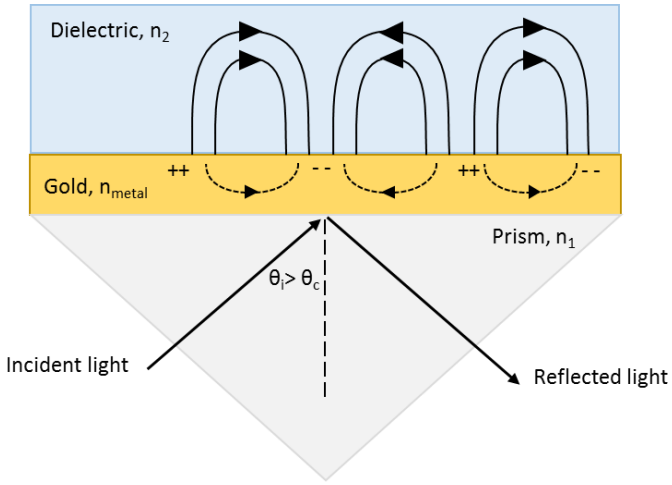

Figure 1. 1 Coupling state of oscillations at the interface of gold-dielectric in Kretschmann configuration

In spectral interrogation, the wavelength of a broadband light source is swept at a fixed angle, and the resonance response curve is monitored [8]. At the resonance wavelength, there is a strong absorption in the output spectrum. This loss is due to reduction of the reflected light from the metal-dielectric interface and it is strongly dependent on the refractive index of the dielectric medium [9]. A red shift in the output spectrum can be observed as the refractive index of the medium is increased [10].

In angular interrogation, the incident angle of light is swept while monitoring the resonance response curve. The excitation of the surface plasmon occurs at the angles greater than critical angle as the wave vector of the evanescent wave produced at the interface, matches the wave vector of surface plasmon (since the wave vector of the plasmon is bound to metal surface). The wave vector of light traveling in prism with refractive index n_1 with incident angle of θ_i and wavelength of λ, could be tuned by varying the value of θ as

$$k_x = \frac{2\pi}{\lambda}(n_1)(\sin\theta_i) \quad (1)$$

The wave vector of the plasmon (k_{sp}) depends on the refractive index of the metal (n_{metal}) and the testing medium (n_2):

$$k_{sp} = \frac{2\pi}{\lambda} \frac{(n_{metal} \times n_2)}{(n_{metal}{}^2 + n_2{}^2)^{1/2}} \quad (2)$$

Hence for a given λ of incident light, SPR could be seen as a reduced intensity of the reflected light at a specific angle of incident [11].

Agbor *et al.* [12] reported the SPR gas sensing measurements in Kretschmann configuration using nickel/silver coated glass microscope slides. According to their results, the SPR curves were influenced by 50 ppm of NO_2 and H_2S at room temperature.

Maharana *et al.* [13] reported a numerical study on a high performance SPR sensor based on graphene coated silver on wide range of refractive indices of gases. Graphene is widely used in SPR based gaseous detection systems, as its refractive index is highly sensitive to the absorbed gas molecules. Furthermore, graphene is robust against the oxidation and the layer of graphene in SPR sensors (in presence of noble metals) prevents oxidation of the silver layer.

Nooke *et al.* [14] studied the SPR gas sensing measurements in Kretschmann configuration using gold (Au) coated glass for combustible, toxic and greenhouse gases. They also reported that the gas detection limit is related to the rate of gas adsorption, which is defined by polarizability of the gases.

1.2.2 Fiber optic Based Gas Sensors

The very first fiber optic based sensor was reported in 1965 with the application in clinical cardiac characterization. However the gas sensing application of the fiber optic sensor was developed in 1980s [1].

Fiber optic is a waveguide for optical frequencies and the sensing measurement is essentially based on changing the features of transmitted light along the fiber. Transmitted light can be modified in response to external medium properties.

1.2.2.1 SPR fiber optic gas sensors

The light passes through the optical fibers based on total internal reflections. Consequently, the evanescent wave is present in optical fibers at the core-cladding interface (component of electric field at the plane of incidence, required for SPR). Therefore, by replacing the cladding with a thin layer (in the range of few tens of nanometer) of metal, SPR-based fiber optic sensors are designed. In these sensors it is hard to reach the sensitivity similar to Kretschmann configuration due to complexity in controlling the incidence angle of light, impossibility to control the wave polarization and an excessive number of reflections. In these sensors the spatial-frequency bandwidth of their angular spectrum is wider in comparison with other types of SPR sensors [9], [15]. However, some noticeable advantages like low cost, flexibility, compatibility with human tissue and blood vessels, small sample volume, reusability, and simple structure have made the SPR fiber optic approach very attractive.

1.2.2.2 Extrinsic/intrinsic fiber optic gas sensors

According to the principal of the operation, fiber optic gas sensor devices can be classified into two distinct categories: extrinsic and intrinsic [1], [16].

In extrinsic fiber optic gas sensors, light exits the fiber and interacts with the medium before continuing propagation inside the core again. As it is shown in figure 1.2 light propagates through the input fiber optic toward a microcell containing the unknown gas. The output signal is guided to

a spectrometer using the output fiber optic, which is accurately aligned with the input one.

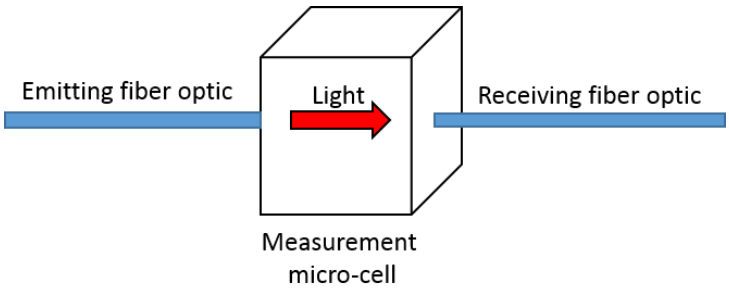

Figure 1. 2 Extrinsic optical fiber sensor. Modified from [16]

This provides the unknown gas detection by comparing the input interrogating wavelength and the absorption spectrum of the gas [16]. This technique can be only used for the gases whose spectral absorption is in the range of telecommunication window so the fiber can be successfully employed.

Stewart *et al.* [17] reported a design of fiber optic methane sensor using a microcell and DFB laser source. The theoretical modeling of the designed sensor was in a good agreement with experimental results and both showed a single absorption line for the methane gas.

Shemshad *et al.* [18], [19] investigated the absorption band of methane and stated that absorbance spectrum of methane is 1620-1700 nm which is suitable for fiber optic detection sensors. As methane is released during coal extractions, they also studied the cross sensitivity of methane with other mine gases and according to their results the absorbance spectrum of methane does not interfere with other mine gases.

In intrinsic fiber optic gas sensors, light propagates inside the core continuously without any external interaction. When a light is propagating through fiber optics, at the core-cladding boundary it undergoes total internal reflection (TIR). During each TIR it penetrates in to the

cladding region, which is known as evanescent wave. The amplitude of the evanescent wave decays exponentially in the cladding region. Therefore, the cladding (with lower refractive index) absorbs a small portion of propagating light energy and this process is known as attenuated total reflection (ATR). If an absorbing chemical or testing sample is present with the evanescent field region, the propagating light will be attenuated (as the reflection coefficient is less than unity) as it travels along the fiber. Since the energy levels associated with an atom or molecules are unique, the absorption spectrum serves as a "fingerprint" identification of the chemical species [1].

To increase the sensitivity of such sensors the cladding can be manufactured to be sensitive to specific organic vapors [20] or an unclad fiber can be coated with sensitive coatings [21]. Another alternative way is diminishing the cladding thickness, which results in a more fragile but more sensitive sensor [16], [19].

1.2.3 Gas Ionization Sensors

These kinds of physical type sensors are based on fingerprinting the ionization characteristics of the gases. These sensors are calibrated based on either breakdown voltages (gas ionization breakdown sensors, GIBS) or tunneling currents (gas field ionization tunneling sensors, GFITS) [22].

The structure of GIBS consists of two parallel electrodes. Applying potential between these electrodes create electric field between them. In relatively low electric fields, ionized gases generate ions and electrons. The electrons migrate to the anode, while ions move toward the cathode electrode; they will be neutralized through external circuit. By increasing the applied electric field, repelled electrons are travelling toward the anode with a very high velocity, causing ionization of other atoms (known as secondary ionization), which will result in a self-sustaining

discharge current (known as breakdown). The method of operation of GIBSs is based on measuring breakdown voltages, which is a unique value for each gas at a constant pressure and temperature according to Paschen's Law. Paschen's Law predicts the breakdown voltages of the gases and states that for uniform fields the ionization breakdown voltage for a specific gas is proportional to the product of the surrounding gas pressure, P, and the electrode spacing, d, i.e. $V_b = f(P \times d)$ [23]. For small values of P.d (<1 Torr-cm) the breakdown voltage is estimated to be in range of thousand volts. However in later experimental studies, it was revealed that Paschen's Law is applicable when the electrode separation is in cm range (large scale systems) and the breakdown voltage is lower (several hundred-volt range) than Paschen's Law for microgap devices [24]–[26]. As high voltage sensing is impractical, having 1D nanostructures instead of parallel flat electrodes leads to nonlinear electric field near the tips of the structures, which results in enhancement of electric field and consequently lowers the breakdown voltages.

Modi *et al.* [27] employed carbon nanotubes grown by chemical vapor deposition (CVD) on SiO_2 substrate as the anode of a two parallel electrodes. The new device showed that the breakdown voltage of air was decreased to 346 V (compared to 960 V detected when a two electrodes were made of flat plates). Hui *et al.* [28] showed that employing anodized aluminum oxide template (AAO) coated with multiwall carbon nanotubes (MWCNT) as the anode reduces the breakdown voltages of air to 200-400 V (as a function of inter-electrode distances between 20 to 160 μm) compared to flat parallel aluminum plates which is 300-1100 V for the same inter-electrode distances.

Other nanostructures like ZnO [29], [30], gold [31] and silver nanowires [32] are used to develop GIBS devices. The breakdown voltages of different gases in different pressures are reported over 200 V, which is still very high for practical gas sensing applications.

Other phenomenon that is used to identify gases in lower bias voltages is field ionization tunneling current (GFITS). The gas atoms are polarized near the positively biased nanowire tip and by the field gradient an electron from gas atom tunnels into the nanowire tip. As ionization voltage and tunneling is specific to any gas molecules, the resulted tunneling current can be used to fingerprint the unknown gas type.

Quantum tunneling occurs when valence electron of gas atoms could escape the atom by tunneling through the nucleuses' potential barrier with a certain probability, due to high ambient electric field. The valence electrons of a neutral atom are trapped inside the potential well and are not able to escape the atom. As it is shown in figure 1.3, atomic potential is distorted toward anode by the strong electric field, and electron can tunnel through the remaining potential barrier.

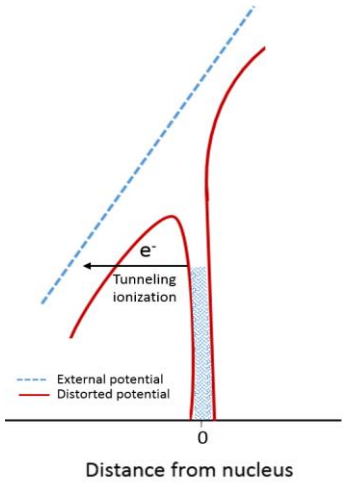

Figure 1. 3 Distorted atomic potential in vicinity of a strong electric field.

Tunneling occurs at a critical distance (X_c) from the electrode surface, since electrons can only tunnel into unoccupied state of the host. As it is shown in figure 1.4, at this separation gap, the ground state energy of the atom is equal to Fermi level of the nanowire [33].

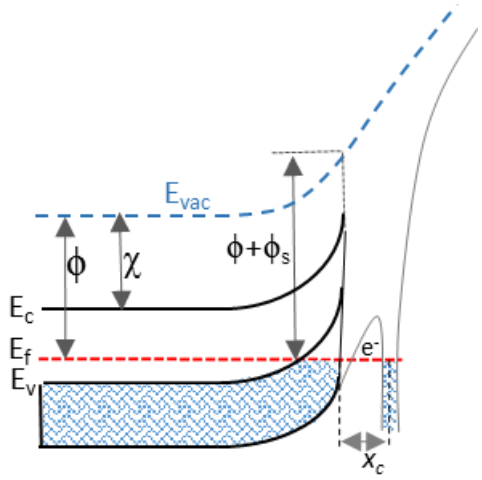

Figure 1. 4 (After Abedini Sohi and kahrizi [34]). Degenerate p-type at surface after upward band bending. Atomic potential deformed at external field. Electrons tunnel through the distorted potential barrier, when the ground state of the electron is equal to Fermi level of the nanowire. Electrons may occupy available energy states in valence band above E_f [35].

Critical distance [36] from semiconductor surface is defined as:

$$X_c = \frac{(U_I - (\phi + \phi_s))}{E} \tag{1.1}$$

in which U_I is ionization potential of atom, ϕ is the semiconductor work function and ϕ_s is the amount of band bending due to field penetration. $\phi+\phi_s$ is effective work function at the surface of semiconductor since in semiconductors the work function is sensitive to the doping level of the surface which is controlled by field penetration (band bending at surface). χ is the electron affinity which is a fixed value and is independent of doping.

The work function of the semiconductor can be written as

$$\phi = E_{vac} - E_F \tag{1.2}$$

while the electron affinity is:

$$\chi = E_{vac} - E_c \tag{1.3}$$

if ϕ_s is the band bending then the effective work function is

$$\phi_{eff} = \phi + \phi_s = \chi + \phi_s - (E_c - E_F) \tag{1.4}$$

The tunneling probability is a function of X_c, and it will increase as X_c decreases. Hence, for p-type semiconductor nanowires, the upward band bending at the surface reduces X_c and as a result increases the tunneling probability. As it is shown in figure 1.4, bending of the energy bands upward make the semiconductor p-type degenerate and electrons may tunnel into valence band above E_f.

To fabricate gas sensors based on tunneling currents, Spitsina *et al.* [37] employed Ag doped ZnO nanowires as the anode which resulted in tunneling currents for N_2, O_2, Ar and He at less than 35 V applied voltage for gas pressures smaller than 0.5 Torr.

Sadeghian *et al.* [36] fabricated template based Au nanowires using porous anodic alumina (PAA) and observed tunneling currents in the samples that PAA template is not removed completely after the fabrication of the structures. According to their results, the ionization was governed by tunneling into the surface states of semiconductive anodic alumina that remains on the Au NW tips due to incomplete dissolution of PAA.

1.3 Objective of the Research

The goal of this research is to fabricate and characterize a gas ionization tunneling sensor using free-standing p-type Si nanostructures. These structures are fabricated using three steps of consecutive chemical and electrochemical etching. Since 2009, after preliminary observations of M. E. Fard [38] on the consecutive etching steps, our research group has been investigating the formation mechanism of the free-standing p-type Si nanostructures and instructions to control the

geometry of the fabricated structures. There have been several experimental studies since then [39], [40] in which the effect of etching parameters are investigated. In this study, for the first time, analytical studies is carried out to identify the mechanism of the formation and evolution of the structures. Experimental work is also conducted to evaluate the effective parameters during the development.

Three etching steps to fabricate nanostructures are:

1) Silicon texturing which is anisotropic etching of (100) silicon wafer in TMAH containing solutions in order to generate pyramidal hillocks on the wafer surface. The effect of the existence of surfactant (IPA) as well as etchant concentration (TMAH) and etchant/surfactant combinations (TMAH/IPA) are reported in this work.

2) Isotropic electrochemical etching of the textured silicon wafers results in formation of the nanowires with arrow shape tips. COMSOL Multiphasic simulation tool is used to model the formation mechanism of the structures. The effect of non-uniform hole current density as a function of electric filed distribution is responsible for establishing these structures.

3) Fine anisotropic etching in diluted TMAH to remove unexpected residuals between the structures.

Currently among the materials which are used in gas ionization sensors, carbon nanotubes (CNTs) are suffering from reversibility issues with the certain gases [3]. Furthermore, ZnO based GITSs are suffering from repeatability issue due to their instable doping properties [41]. In this work ever-lasting p-type Si nanostructures is used as the anode to induce tunneling currents at low voltages. The structures can be a very good replacement for above mentioned materials due to its cost effective fabrication technique, durability and reversibility.

1.4 Organization of the thesis

There are six chapters in this dissertation which are organized in the following format:

Chapter II briefly describes the available silicon nano-fabrication techniques and emphasizes on the theoretical background of the etching steps employed in this work.

In *chapter III* the technique to fabricate silicon nanostructures with a great freedom in controlling the characteristics of the structure is discussed in detail. The experimental results are discussed and supported by analytical studies via modeling and COMSOL simulation tool.

Chapter IV provides a literature review on the operation of Gas Ionization Sensors and the field enhancement effect of applied nanostructures in those devices.

In Chapter V the optimum condition of the morphology of the nanostructure for Gas Ionization Sensor applications is determined. The sensor fabrication process and its characterization method including the results are discussed in this chapter.

In *chapter VI* conclusions are summarized and suggestions for future research are given.

Chapter 2
Literature Review: Techniques to Fabricate Silicon Nanowires

2.1 Silicon Nanostructure fabrication Techniques

Vertical metallic and semiconductor nanorods/wires have provided a powerful platform for diverse electronics, and sensing applications. They are being used in variety range of devices such as pn junctions, LEDs, bipolar junctions and even computational circuits. Si is known as chemically stable, nontoxic, and biocompatible. Si exhibits a number of properties that make it a competitive material in fabrication of solar cells [42], batteries, nanoelectronic devices [43], [44], sensing structures [45], [46], as well as health care applications [47]. For each specific application mentioned above, a particular nanowire structure may be needed; therefore, it is very important to fabricate nanowires with controlled density and morphology.

Silicon nanowire can be fabricated using both *top-down* and *bottom-up* techniques. An example of top-down Si nanowire fabrication is metal assisted electrochemical etching [48]–[50]. In this method Si atoms under metal ion are oxidized and etched much faster due to the injection of holes by noble metals to the Si surface. An example of bottom-up Si nanowire growth is VLS mechanism, in which Si nanowires are growing based on chemical vapour deposition onto a gold/silicon catalyst droplet [51]–[53]. To achieve uniform and well-ordered nanowires, template based VLS mechanism can be employed. In this technique porous anodic alumina (PAA) is utilized as a mask for depositing gold catalyst seeds [54].

Other method to fabricate Si NWs is using several steps of isotropic and anisotropic etchings of silicon wafers. To describe the method we first review the nature of anisotropic and isotropic etching of silicon in details in the following section.

2.1.1 Isotropic and anisotropic etching

One of the processes in nano-manufacturing is removing particles, at the scale of atoms, from the surface of bulk materials using etching techniques. Etching is done either using chemical reaction between etchant and the material, called wet etching, or by bombarding the surface of bulk materials with energetic ions or atoms, called dry etching. In Dry etching material particles are removed selectively by either plasma assisted ion bombardment etching (IBE) or chemical plasma etching (PE) in which chemical etchant atoms in the plasma (as an etchant supplier) diffuses into substrate surface and etching occurs [55].

Wet etching is a subtractive process that removes atoms from the surface of materials (such as Si) with a pure chemical reaction. The etchant solutions are either alkaline or acidic and the process can be isotropic or anisotropic which refers to the orientation dependency of the etching rate [55]. Figure 2.1 illustrates the difference between isotropic and anisotropic etched surfaces of Si wafer.

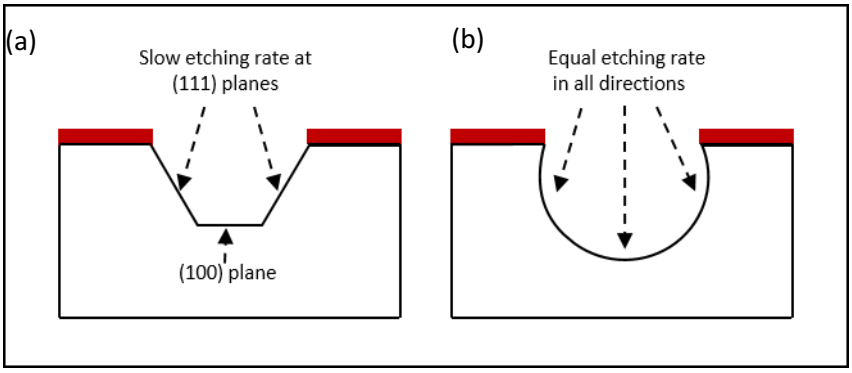

Figure 2. 1 Si etching in a rectangular opening mask. a) Anisotropic etching of (100) Si generates inverted pyramids due to slow etching rate of (111) planes compared to (100) planes, b) Isotropic (100) Si etching.

The difference in etching rate of various planes of Si can be explained by its diamond cubic structure and the energy of Si-Si back bonds. As it can be seen in figure 2.2 Si atoms on {100} family planes have only two back bonds and it is easier than {111} family planes to be etched away as Si atoms on 111 plane have only one available dangling bond and is strongly associated to the crystal by three Si-Si back bonds. {111} Family plane is called a non-etching orientation as a result of highest atom-packing density.

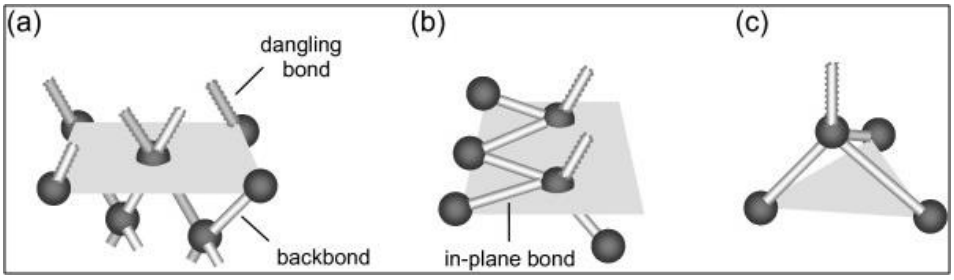

Figure 2. 2 (Adopted from Yu *et al.* [56]) Each Si atom is covalently bonded to four Si atoms. The concentration of dangling bonds, back-bonds and in-plane bounds are shown for a) 100 plane, b) 110 plane and c) 111 plane.

Figure 2.3 compares the results of anisotropic etching along (100) and (110) planes. Anisotropic etching of silicon along (100) generates an angle of $\theta_{(100),(111)}$ equal to 54.74° and etching along (110) generates angles of $\theta_{(110),(111)}$ 32.65°, 90° and 144.74°.

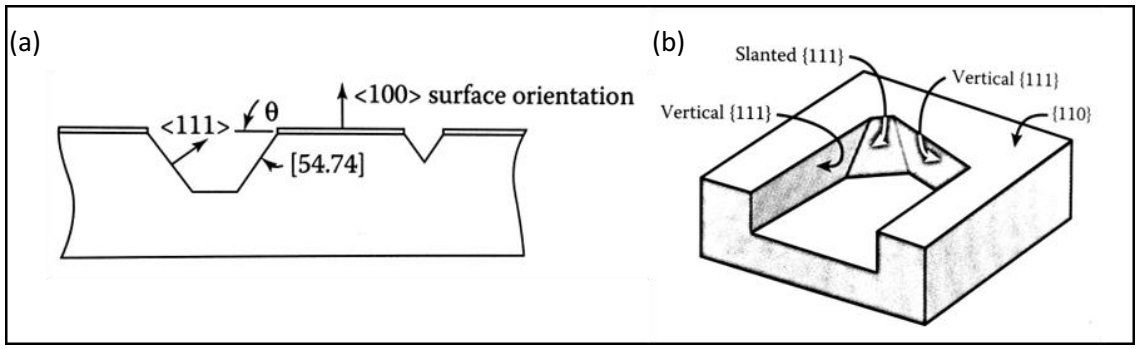

Figure 2. 3 (Adopted from Madou *et al.* [57]**)** Si etched by a rectangular mask a) (100) plane b) (110) plane; Slanted (111) refers to 32.65° and 144.74°, and vertical (111) refers to 90°.

2.1.2 Si anisotropic etching using TMAH

Tetramethylammonium hydroxide ($N(CH3)_4^+OH^-$/ TMA^+OH^-), known as TMAH, is an anisotropic etchant of silicon. TMAH is widely used as anisotropic etchant as it is neither toxic nor harmful. Due to the large selection ratio of (100) /(111) etching rate, pyramidal hillocks are produced during anisotropic etching of (100) silicon samples in diluted TMAH solutions. The tips of the pyramid are the points that the formation of the hillocks initiates. The non-etching texture of the tips can be attributed to wafer surface defects or existence of oxide particles. [58]

TMAH is highly soluble in water as H_2O molecule is a highly polar solvent (electron density is not equally distributed in water molecule) so the molecule is partially negative and partially positive. This property leads to formation of a layer of water molecule around ionic compounds, which is known as hydration. Hydration of TMAH is shown in figure 2.4.

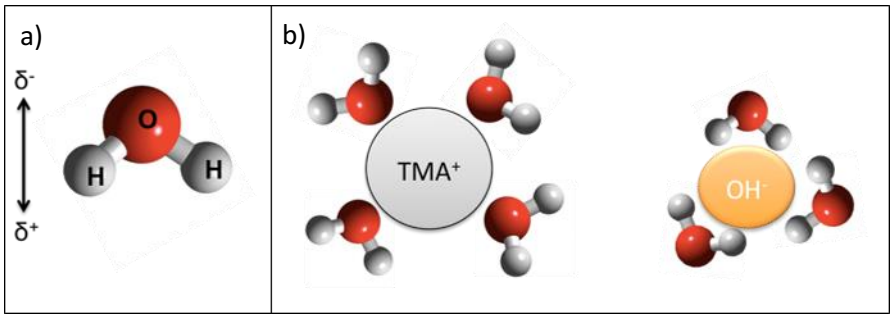

Figure 2. 4 Solvation power of water; a) Water electron density. b) TMAH hydration

Si wafers, exposed to air, are normally covered by a thin layer of native oxide (hydrophilic). Before etching process this oxide layer is etched away by a HF: NH_4F solution, at this point the surface dangling bonds are terminated by hydrogen (H), which makes the surface hydrophobic.

According to Re 2.1, in alkaline medium Si-H bond is replaced by OH^-. The released hydride (H^+) reacts with hydrogen in water molecule, as they are not strong covalent bonds, and creates hydrogen gas (H_2). So the role of water is to prepare hydrogen pair, for any released hydrogen atom and to create excess hydroxyl (OH^-).

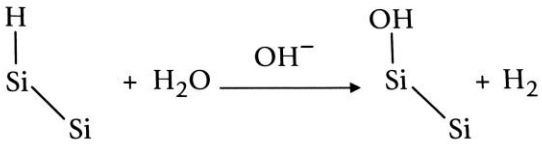

(Re 2.1)

According to Re 2.2, covalent bond with hydroxyl group polarizes the Si-Si back-bond, makes it susceptible for H attacks. The back-bond breaks and surface atom forms new covalent bond with another OH.

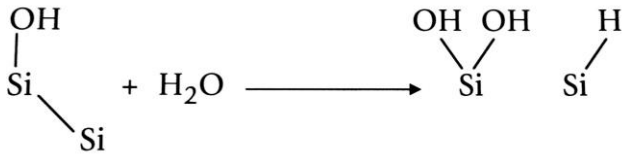

(Re 2.2)

Reactions 2.1 and 2.2 are only showing the reaction of Si surface atoms with hydride and hydroxide. But the number of back bonds is dependent to its surface plane orientation. This process also explains the low etch rate of 111 planes. At the beginning of the process (111) has monohydride termination at the surface and three Si back bonds while at 100 planes the surface Si atom has dihydride termination, which is less stable than monohydride.

Lysko et al. [59] explained the mechanism of silicon anisotropic etching (in KOH anisotropic etchant) based on electrostatic charges on sample-etchant interface and Helmholtz double layer. The crystal surface terminates by Si atoms with one, two and even three unsatisfied bond. A Helmholtz double layer (HDL) occurs at a surface where the surface of solid contacts with a fluid. Figure 2.5 shows Helmholtz model, which comprises two planar sheets of induced charges. One is due to the negative OH^- ions in solution adsorbed at the surface of unsatisfied Si atoms; the other is due to the ions of opposite charge attracted by adsorbed ions. The coulomb energy estimated between Si dangling bonds and negative charge of OH^- is about 2.65 eV which is higher than breaking Si-Si bond (2.15 eV). The difference between planes' etching rate is their surface dangling bond density or in other word, their back-bond densities.

Hydroxide ions at inner Helmholtz layer directly react with Si atoms. The excess hydroxide ions in the electrolyte do not have any effect on the etching as the OH^- layer formed on the surface, repels them. This explains why by increasing the etchant concentration, the etching rate will not increase.

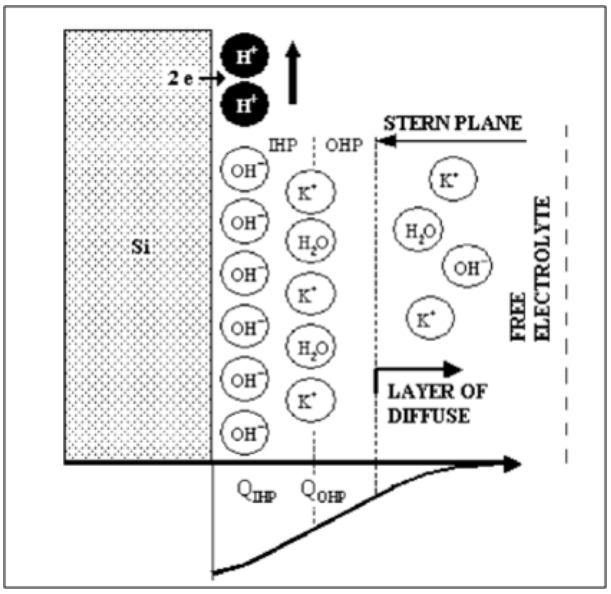

Figure 2. 5 (Adopted from Lysko *et al.* [59]) There is a layer of aligned ions as the first layer, which is one particle thick and then immediately next to that, free solution.[59]

Important parameters in formation and evolution of pyramidal hillocks are; TMAH concentration, etching time and etching bath temperature. Tabata *et al.* [60] attempted to compare the etching rates of (100) Si crystal plane in various TMAH concentrations from 5 - 40% at 60 – 90 °C. According to their results shown in figure 2.6, the etch rate decreases with increasing TMAH concentration. They also observed that the roughness of the etched surface decreased in higher than 22 wt% concentrations.

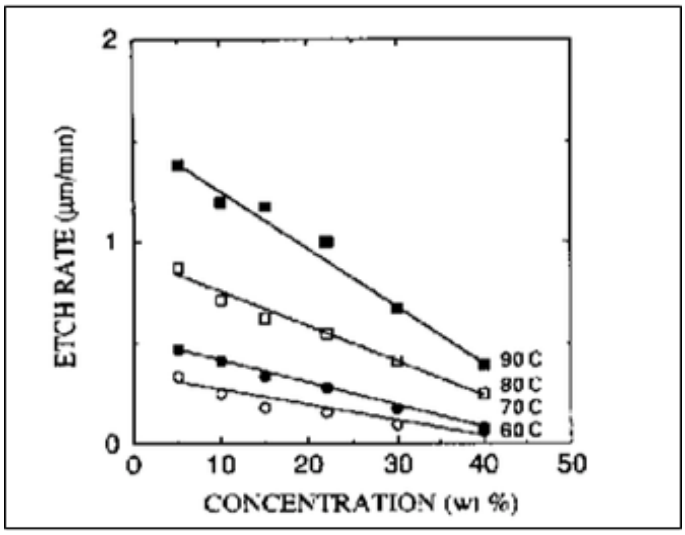

Figure 2. 6 (Adopted from Tabata *et al.* [60]) (100) etch rates dependence on concentration and temperature of the etchant.

Merlos *et al.* [61] research also confirmed that the quality of the pyramid surfaces are dependent on TMAH concentration. Their results showed that for 25 wt% TMAH concentrations the hillocks surface are very smooth. To fix the roughness of the etched surface in low concentrations they proposed IPA (isopropyl alcohol) addition as a surfactant. They concluded that IPA does not have any effect on pyramid density but improves the size and morphology of the hillocks by reducing the formation of micro pyramids on the pyramid sides.

The main reason of the roughness in the produced pyramids is explained by Papet *et al.* [62]. They used pure diluted TMAH in different temperatures and etching time. Their results indicated that hydrogen bubbles form and stuck on the Si surface and eliminate the etching process and as a result the distribution and the size of the pyramids is managed by hydrogen molecules, so the resulting structure is neither uniform nor reproducible. To avoid hydrogen bubble formation they tried two solutions. Firstly they added IPA surfactant to increase hydrophobic nature of Si

surface. Secondly they applied agitation by ultra sonicator (US). The use of US resulted in a reproducible and uniform texture on the wafer surface shown in figure 2.7.

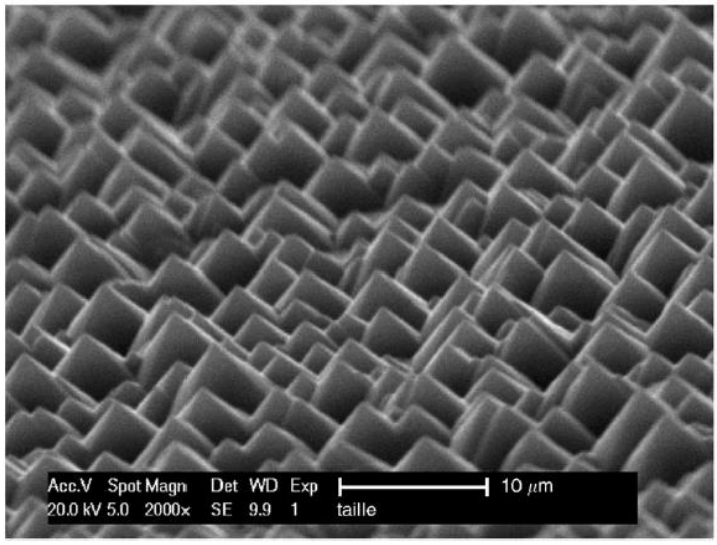

Figure 2. 7 (Adopted from Papet *et al*. [62]) Uniform textured silicon surface etched by 20 min US followed by10 min without agitation, in 2% TMAH: 10% IPA, 80°C.

Generally wet chemical etching has three main processes: 1) movement of etchant ions to the sample surface, 2) chemical reaction between wafer and solution and 3) movement of soluble etched particles away from the sample. To reach a uniform and well-controlled etching rate agitation is used to supply etchant and to remove etched products from the surface.

The effect of time on evolution as well as dissolution of hillocks is noted in the experiments of Thong *et al.* [58]. In their work Si samples were etched at 4 wt% TMAH with various etching durations. Based on their results, initiation, formation and dissolution of the hillocks take place simultaneously and it is not possible to observe the sample in specific stage although overetching finally gives rise to collapsing pyramids, merging into the surface and leaving a rough patch

instead. Figure 2.8 shows the proposed etching mechanism in which dissolution starts from the tip of the pyramid and 100 terraces at the sides. Landsberger *et al.* [63] noted that the pyramids have four bowed faces, near (111) planes. As shown in figure 2.9 (110) ledges and (100) terraces are the points for dissolution initiation.

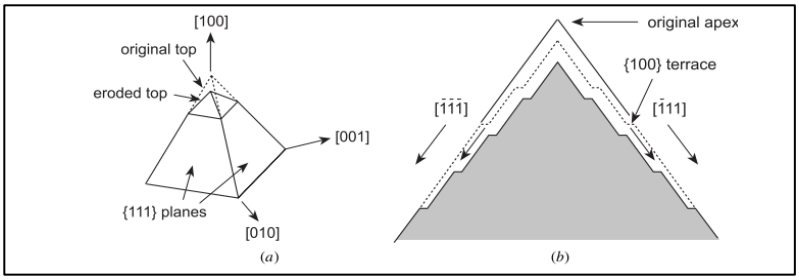

Figure 2. 8 (Adopted from Thong *et al.* [58]) Dissolution mechanism of the hillocks (a) Etching of the top portion of a pyramid. (b) Proposed etching mechanism due to existence of {100} terraces as anisotropic etchants work much faster in the mentioned direction compared to {111} family planes.

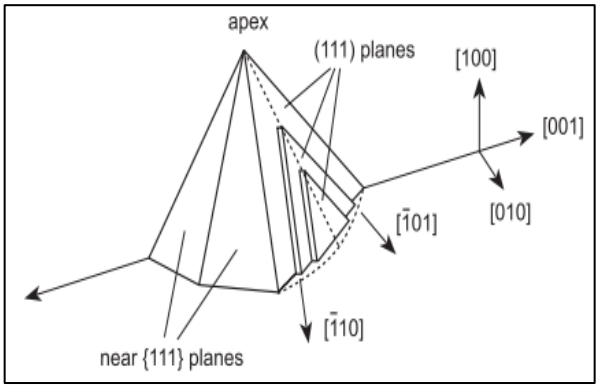

Figure 2. 9 (Adopted from Landsberger *et al.* [63]) Dissolution mechanism of the hillocks due to existence of fast-etching {100} and {110} family planes.

2.1.3 Si isotropic etching using HF electrolytes

Isotropic Si etching occurs in HF based acidic electrolyte, which can be done either chemically or electrochemically.

2.1.3.1 Chemical isotropic etching (wet isotropic etching)

Isotropic etching of Si is performed in HF based electrolytes. The solubility of Si in pure hydrofluoric acid (HF) is very low. On the other hand HF dissolves silicon oxide very fast, (the etch rate selectivity, $\frac{SiO_2}{Si} > 100$). As a result, the isotropic chemical etching of silicon in HF-based electrolytes must happen through two successive processes. In the first reaction (Re 2.3), silicon should be oxidized to generate a layer of silicon dioxide then in the second reaction (Re 2.4) silicon dioxide layer will be etched away by dissolving in HF. Therefore, the etch rate and the generated final structure of porous silicon is very depended on the first reaction (oxidation of the silicon sample).

$$Si + 2H_2O + 4h^+ \rightarrow SiO_2 + 4H^+ \quad \text{(Re 2.3)}$$

$$SiO_2 + 6HF \rightarrow SiF_6^{2-} + 2H_2O + 2H^+ \quad \text{(Re 2.4)}$$

As shown in Re 2.3 four positive carriers/holes ($4h^+$) at the interface of the semiconductor and electrolyte, break the back-bond of silicon which causes the oxidation of the sample [55].

As HF is not a good oxidizer (hole provider), it is necessary to add an oxidizer agent to the electrolyte to enhance the oxidation rate. Among oxidizer agents, nitric acid, which is a very strong oxidizer, is used to mix with HF to promote oxidation of silicon samples. DI water or acetic acid can be used as diluting agents to adjust the etching rate.

In this method the final structure of the etched surface, depends on the ratio of HF and oxidizer concentrations. In high HF concentrations, etching rate is low and Si surface becomes rough with sharp corners and edges. High oxidizer concentration increases the etching rate and results in a smooth surface [55].

2.1.3.2 Electrochemical isotropic etching

In electrochemical etching [64], applying forward bias to p-type samples provides more holes at semiconductor/electrolyte interface. In this case there is no need to add any oxidizer agent to the electrolyte (The oxidizer in the electrolyte is replaced by positive bias). Porous silicon is generated from electrochemical etching of the p-type Si in an HF based electrolyte. Figure 2.10 shows the porous Si fabricated by electrochemical anodic etching of p-type Si using a constant applied current density.

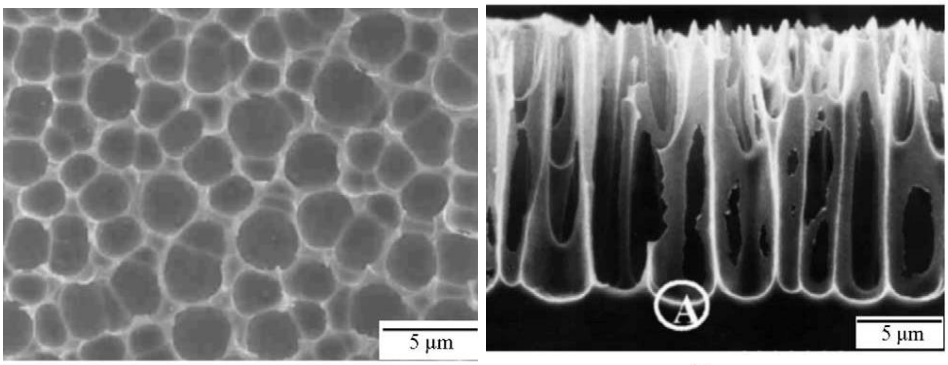

Figure 2. 10 (Adopted from Kim *et al.* [64]). a) Top view and b) Cross section of the samples prepared by electrochemical anodic etching of p-type Si wafers at 50 mA/cm^2 for 10 min in HF/Ethanol/water =1:2:1.

Chapter 3
Synthesis and Characterization of Silicon Nanostructures

3.1 Fabrication of Silicon nanowires

In this work arrays of silicon microstructure with sharp nanosize tips are fabricated using a low-cost chemical/electrochemical etching method. The technique consists of consecutive chemical and electrochemical etching steps. Contrary to most methods reported in the literature, this technique will cut the cost and the time of the fabrications significantly. In this mask-less and non-lithographical approach, we first texture the surface of a silicon wafer using anisotropic wet etching in TMAH solution to generate pyramidal shape seeding points. The subsequent fabrication stage consists of electrochemically etching to generate the wires. As final physical properties such as structures, shapes, sizes, aspect ratio, and their morphologies are dependent on several fabrication parameters, the fabrication mechanism is studied as the structures were developed. For this, we have fabricated the structures in several steps considering various parameters during the experimental works to check the effect of each parameter on the structure formation.

3.1.1 Texturing silicon by anisotropic etching

Samples of p-type/boron doped (100) silicon wafer, with the thickness of 380±20 μm and 5-10 Ω.cm resistivity (bought from Silicon Materials Inc.) were cut in 2×2 cm^2 pieces and cleaned using RCA technique before starting the etching process. Samples are etched in a solution of anisotropic etchant of diluted TMAH. A flux lid with running cold water was used to cover the

container of the etchant, in order to keep the etchant concentration constant during the experiment. The temperature of the solution was controlled using an oil bath system. According to the previous studies on the effect of the temperature of the etchant on the etching rate [40] , 90° C is considered for Si texturing in all experiments, which gives rise to the most suitable etch rate under the time frame of the process.

3.1.1.1 Effect of IPA on surface coverage

During anisotropic etching of silicon hydrogen molecules are released. Hydrogen bubbles stick on the Si surface and eliminate the etching process. Adding IPA to the etchant solution increases hydrophobic nature of Si surface and consequently liberates accumulated H_2 molecules from the Si surface. Figure 3.1 compares Si samples etched in TMAH for 20 minutes at 90°C, with and without adding IPA to the solution. As it can be seen in figure 3.1.a (samples are etched in 5 wt% of TMAH) the surface coverage of the pyramids is about 5%. Figure 3.1.b shows that the surface coverage is increased to 100% once we added 5 wt% IPA to the solution.

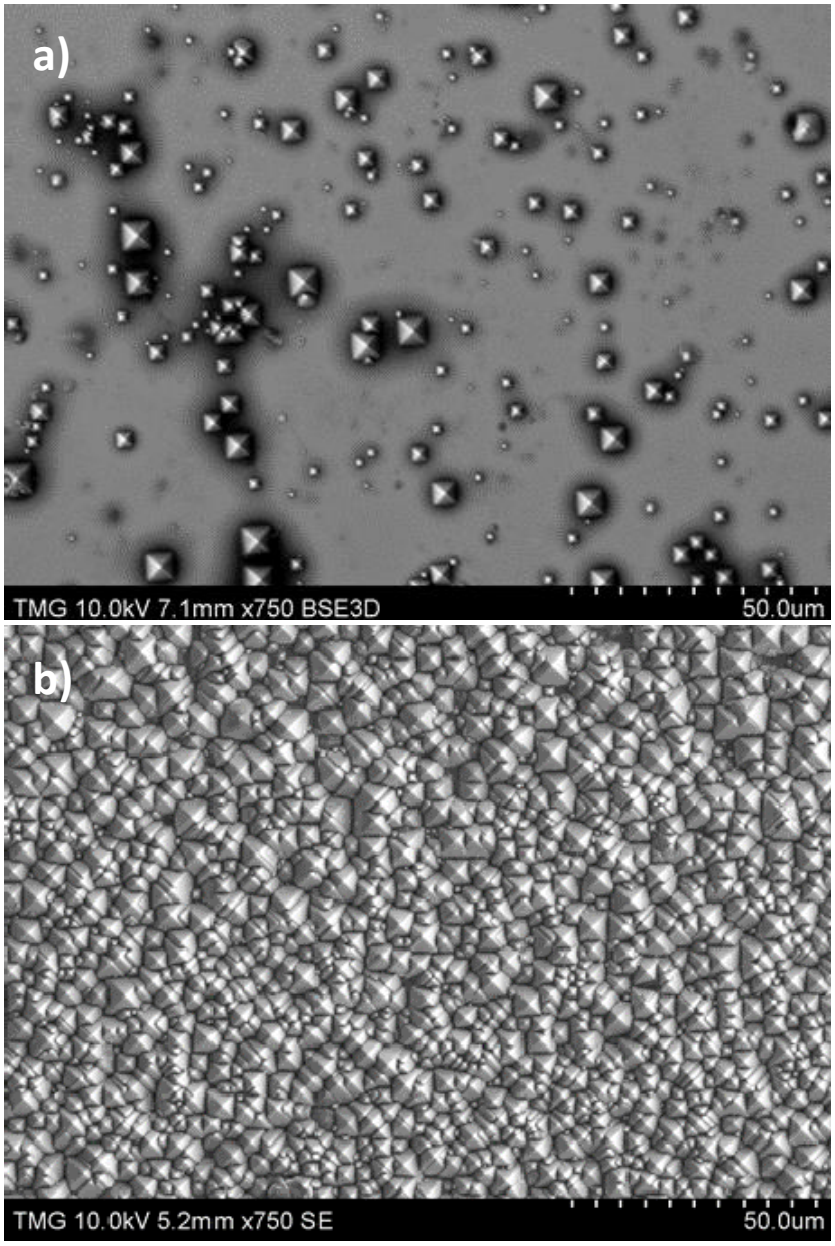

Figure 3. 1 (After Abedini Sohi and Kahrizi [65]) (100) silicon wafer etched in 5 wt% TMAH for 20 minutes at 90 °C, a) Without IPA b) With 5 wt% IPA. Added IPA results in high concentration of hillocks.

3.1.1.2 Effect of etching duration on hillocks morphology

Due to the anisotropic etching of Si in TMAH, pyramidal hillocks are produced caused by point defect on the surface of the silicon sample. As the point defects may be distributed on various layers close to the surface of the silicon, the hillocks are generated at various stages during the etching process. As a result, the silicon surface is covered with pyramidal hillocks with various sizes at the end of the etching process. As the etching is a continuous process, when the various layers of silicon surface are exposed to the etchant, new hillocks are generated while the older ones may be etched away and disappeared. Consequently, the size, shape, and the concentration of the hillocks (surface coverage) are dependent not only on etchant solutions, but the period of etching plays significant roles in this process. To inspect the effect of etching time three experiments were carried out using 5 wt% TMAH, in absence of IPA (no additive), at 90 °C for etching durations of 20, 30 and 40 minutes.

As figure 3.2 shows after 30 minutes the samples are over-etched and it was observed that the shapes of the hillocks were changed. Most of the hillocks etched in 30 or 40 minutes have neither sharp tips nor squared-base structure anymore.

In this work, after several experiments, it is found out that etching samples for around 20 minutes considering other parameters produces relatively a proper pyramidal shape and surface coverage under any circumstances.

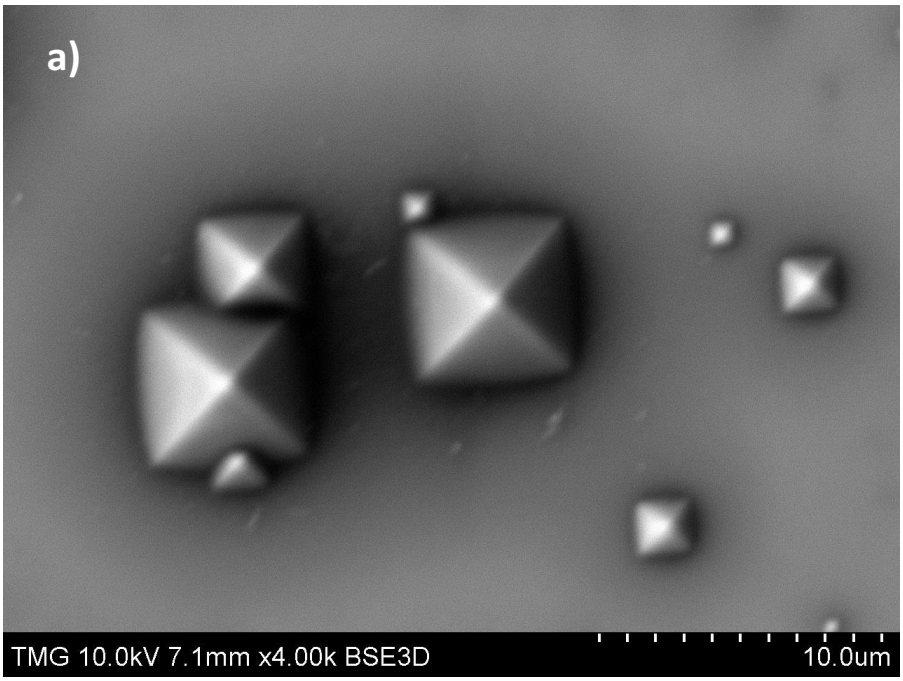
a)
TMG 10.0kV 7.1mm x4.00k BSE3D
10.0um

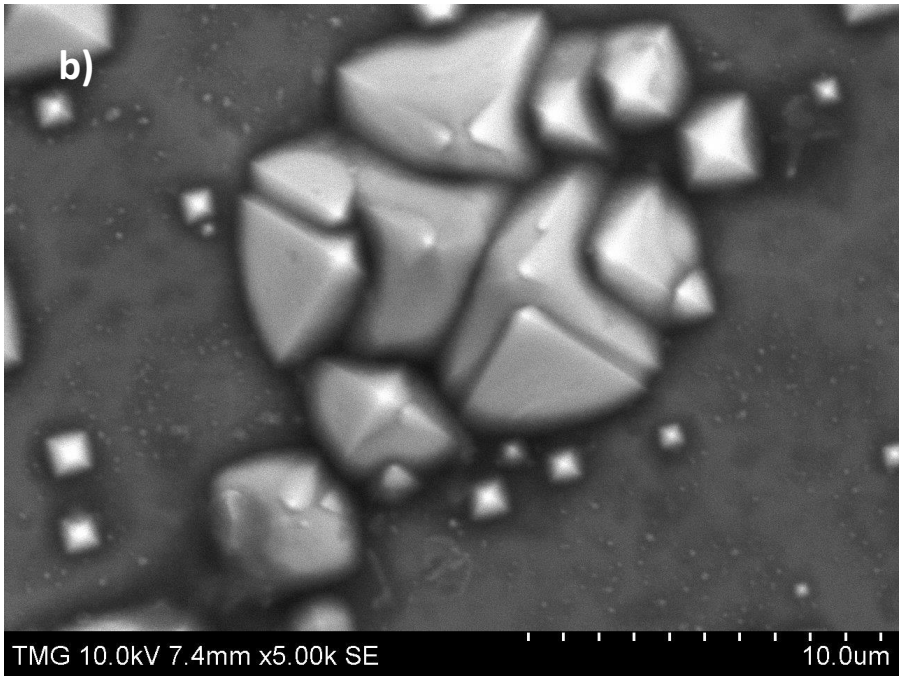
b)
TMG 10.0kV 7.4mm x5.00k SE
10.0um

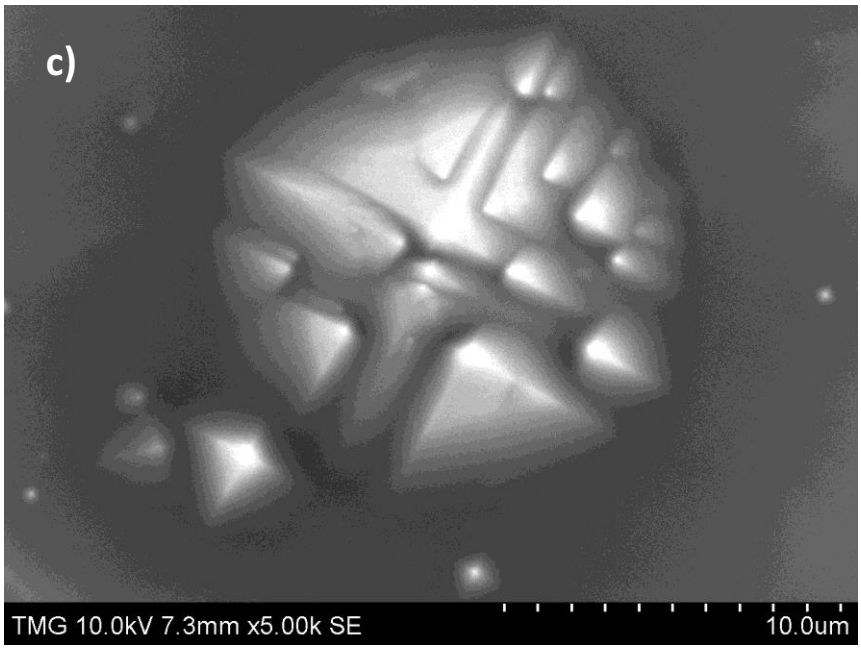

Figure 3. 2 a) Proper pyramidal shape after 20 minutes of etching, b) Over etched pyramids after 30 minutes and c) Over etched pyramids after 40 minutes etching.

3.1.1.3 Effect of TMAH / IPA concentration on hillocks morphology

Anisotropic etching of (100) Si in TMAH solution results in forming pyramids with random sizes. The average size and concentration of the pyramids are very dependent on the etching solution (combination of TMAH and IPA).

Various etchant combinations were considered in this study. Figure 3.3 shows the SEM images of (100) Si surface etched in various combinations of TMAH/IPA solution at 90°C for 20 minutes.

Surface of a silicon sample etched in 1 wt% TMAH and 1 wt% IPA solutions is shown in figure 3.3.a. As it is seen, low concentration of the solution generates a non-uniform and unfinished coverage of the surfaces.

Our studies show that adding IPA to the etchant solution not only changes the concentrations of hillocks but it also affects the size of the pyramids due to diluting the etchant. Figure 3.3.b shows the image of a sample etched in 1 wt% TMAH and 2 wt% IPA solution. By increasing the amount of IPA in the solution, the surface coverage is improved but the average size of the pyramids is reduced as TMAH is now more diluted. Here TMAH concentration is not enough and the resulting structure is not uniform in term of size and concentration. Furthermore, although 2 wt% of IPA in the solution has improved the concentration of the hillocks but the results shows that still the concentration of IPA is not enough to achieve a full coverage of surfaces. Our studies showed that we need at least 3 wt% of IPA in the solution in order to produce samples with the surfaces entirely covered with pyramids. Figure 3.3.c shows the sample etched in 5 wt% TMAH and 3 wt% IPA solution. Clearly 3 wt% IPA results in surfaces completely covered by hillocks. As the concentration of TMAH is higher the average size of the pyramids are also very large (in the range of 10-20 μm). Figure 3.3.d shows the result of etching samples in a solution of 3 wt% TMAH and 3 wt% IPA solution. Under this condition, surfaces with high concentration of hillocks with average perimeter size of 2 μm are generated. Once the concentration of etchant solution is increased to 5 wt%, the average size of the pyramids increases to 5 μm. The SEM image of one of these samples is shown in figure 3.3.e. Figure 3.3.f shows the SEM image of a sample etched in 10 wt% TMAH and 10 wt% IPA solution. Here, high TMAH concentration resulted in a surface with fragmented pyramids, mostly with round tips. In other words, the samples are over- etched.

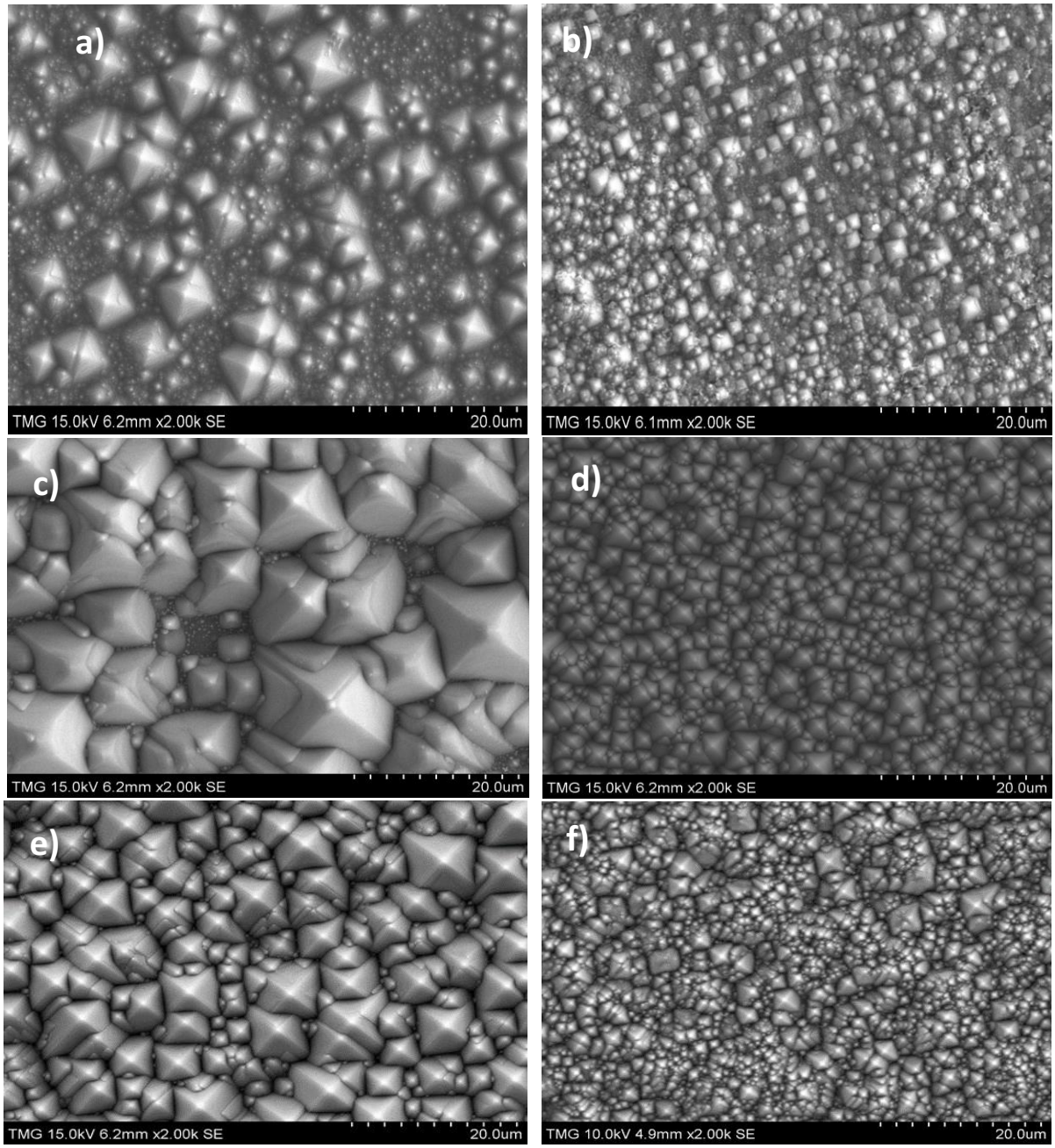

Figure 3. 3 (After Abedini Sohi and Kahrizi [66]) Anisotropic etching of p-type silicon at 90°C for 20 minutes, a) 1 wt.% TMAH and 1 wt.%IPA resulted in unfinished and irregular coverage, b) With 1 wt.% TMAH and 2 wt.%IPA solution surface coverage improved but structures are smaller due to lack of TMAH, c) 5 wt% TMAH and 3 wt% IPA d) 3 wt% TMAH and 3 wt% IPA resulted in smaller pyramids. e) 5 wt% TMAH and 5 wt% IPA, f) 10 wt% TMAH and 10 wt% IPA resulted in over-etched samples.

3.1.2 Electrochemical etching of the textured silicon

3.1.2.1 The etching solution

Porous silicon is generated by electrochemical etching of Si samples in an electrolyte containing HF in a electrochemical cell. An anodic current monitored by a galvanostat is applied between the working electrode (the sample) and platinum counter electrode. Cyclic voltammogram of the etching process is shown in figure 3.4. The graph drawn by triangles shows the current versus potential curve of silicon etching process in aqueous HF (1:3 HF to DI water ratio), which is compatible with typical curve of Si etching in the literature. The curve shows that the properties of the final etched structure are highly affected by applied voltages.

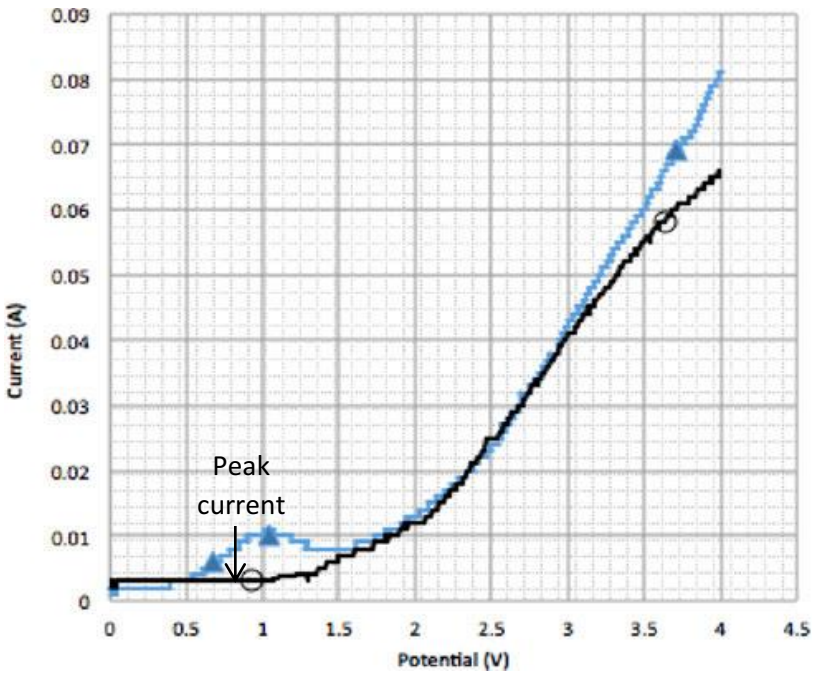

Figure 3. 4 (After Abedini Sohi and Kahrizi [66]) Cyclic voltammetry curves of electrochemical etching of Si in aqueous and anhydrous electrolytes. HF:DI water electrolyte is shown by the blue triangle-line. The exponential trend of the curve at voltages bellow the peak current refers to pore formation. At voltages over the peak current (1 V) electropolishing takes place. In HF:Ethanol curve shown with the black circle-line the exponential trend at any bias refers to pore formation regardless of bias.

Electropolishing of the samples occurs at voltages above the peak-current voltage while porous silicon formation occurs at voltages below the peak-current [67], [68]. In electro-polishing region (high applied voltage) in a two-step reactions Si samples will be etched uniformly. In Re 3.1, silicon is oxidized first (at the present of water molecules), then in the second step, Re 3.2, the oxide layer will be etched away. The holes ($4h^+$) in Re 3.1 are generated by applied forward bias.

$$Si + 2H_2O + 4h^+ \rightarrow SiO_2 + 4H^+ \quad \text{(Re 3.1)}$$

$$SiO_2 + 6HF \rightarrow SiF_6^{2-} + 2H_2O + 2H^+ \quad \text{(Re 3.2)}$$

On the other hand, under low voltage biased system (for the voltages below peak-current) lower concentrations of holes carriers are generated and we have Re 3.3, between the silicon samples and electrolyte solution, which generate porous silicon.

$$Si + 6F^- + 2H^+ + 2h^+ \rightarrow SiF_2^{-6} + H^2 \quad \text{(Re 3.3)}$$

The curve shown by circles in Figure 3.4, demonstrates the variation of current versus potentials when the silicon samples are etched in an etchant containing HF and ethanol, when no water added to the solution. This curve shows that current changes exponentially as the applied voltage changes, which means in anhydrous electrolytes, porous silicon will be generated regardless of biased voltage [68].

For this reason, in this work, as it is our purpose to create pores over the textured silicon samples prepared under anisotropic condition, anhydrous ethanol is used to dilute the electrolyte containing HF so, porous silicon will be developed based on the Re 3.3. Figure 3.5 illustrates a sample of developed silicon nanowires. Textured Si (shown in figure 3.3.e) is anodically etched in 1: 3 HF-ethanol electrolyte for 20 minutes in 80 mA/cm^2 anodic current. As it can be seen free

standing nanowire arrays with sharp tips and aspect ratio of almost 20 are developed under this condition. The nanowires are separated with 5 μm interval on the whole surface of the sample.

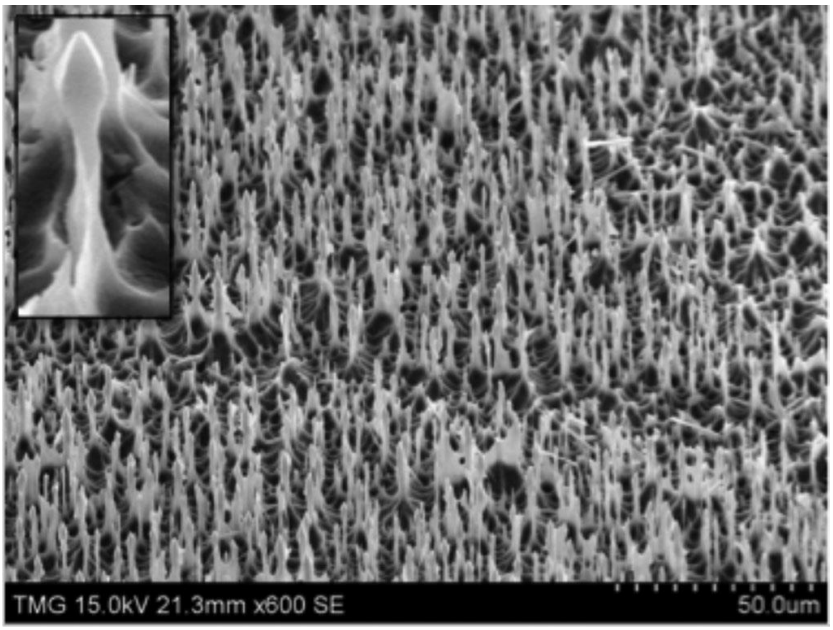

Figure 3. 5 (After Abedini Sohi and Kahrizi [66]) Fabricated freestanding nanowires after two step etching process (texturing Si by anisotropic etching followed by isotropic electrochemical etching).

3.1.2.2 Formation Mechanism; Analytical and experimental Results

A good understanding of the mechanism of nanowires growth helps us to adjust our developing technique to control the size, shape, configuration and concentration of the nanowires. For this, we tried to analyze the growth of the nanowires analytically, using modeling and simulation of electric currents (due to the hole carriers inside the silicon samples) and distribution of the electric field at the interface of silicon and electrolyte. The effects of these parameters on the structures' pattern are investigated. Then we compared the results with what we have observed experimentally to develop nanowires in several steps under various etching

parameters.

According to chemical reactions given in Re 3.1– Re 3.3, electrochemical dissolution of Si is highly influenced by availability of holes (positively charged carries) at the surface of the samples. So, the hole current at the interface of the silicon/electrolyte plays an important role to develop porous silicon. Due to the non-uniformly textured silicon surfaces (pyramidal structure), the current is not uniform at the interface. As a result, the etching rate is not uniform over the surface of the samples and different areas are experiencing different level of dissolution during the anodic etching.

To check the distribution of hole carriers at Si and electrolyte boundary, semiconductor module *(semi)* of COMSOL multhiphysics is used to simulate hole current density at the anode (textured silicon). 2D-pyramidal structure is considered as the simulation geometry. Voltage is applied to the backside of the textured Si as it is shown in figure 3.6.a. Figures 3.6.b and 3.6.c show the results of simulated electric current between the electrodes due to the positive carriers (hole drift current). As it is clearly shown, the hole current density is much higher at pyramid edges. Hole drift current in semiconductors can be found by,

$$J_p = q.p.\mu_p.E\ (\frac{A}{cm^2}) \tag{3.1}$$

where q is electric charge (1.6×10^{-19} coulomb), p is the concentration of holes / cm^3, μ_p is the hole mobility (cm^2/V.s) and E is the applied electric field (V/cm).

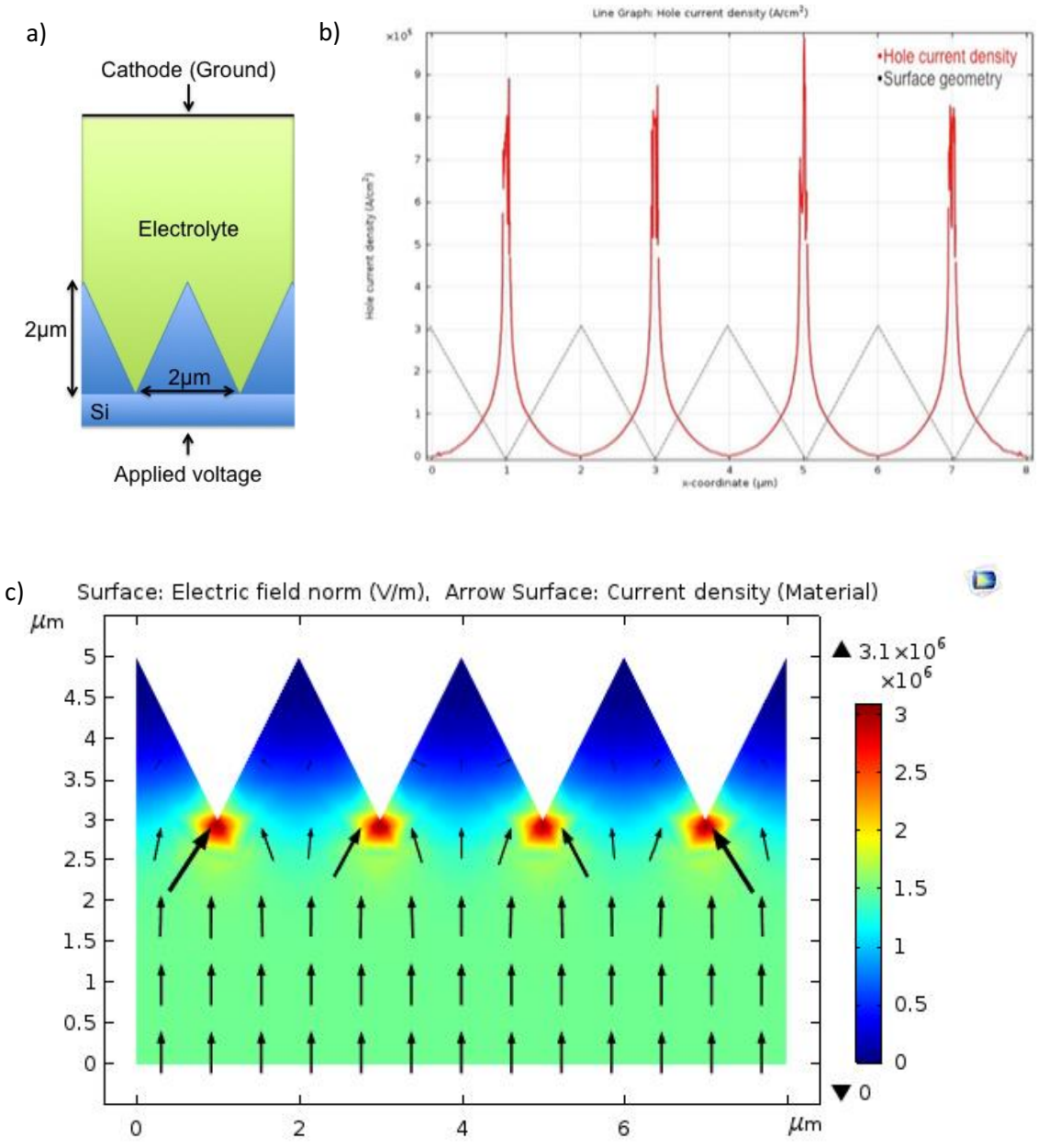

Figure 3. 6 a) schematic 2D geometry of the model. b) (after Abedini Sohi and Kahrizi [66]) Hole current density at semiconductor-electrolyte boundary simulated by 2D COMSOL semiconductor physics interface. c) Geometry of the pyramids of the textured silicon is shown by triangles. Maximum current happens at the pyramid perimeters due to higher electric field at the intersection of the pyramids. In this figure arrows are showing the direction of the current and it is proportional to current density strength.

As the carrier drift current in a semiconductor is due to the applied electric field (equation 3.1), we have also modeled and simulated electric field intensity generated at textured Si (anode) utilizing COMSOL. Figure 3.7 shows the electric field distribution (contour/surface) for 2D and 3D structures calculated by voltage gradient (2V is applied to the bottom boundary of p-type Si). As it is shown, the electric field has the highest intensity at pyramid perimeters, which can be explained by edge effect, and as we move toward the vertex the electric field is decreasing.

To study the evolution mechanism we have considered the 2D schematic geometry and initial electric field distribution shown in Figure 3.7.b. COMSOL deformed geometry (dg) physics interface is applied to all domains and a prescribed mesh velocity is assigned to the boundary between Si and electrolyte (pyramidal texture) and a prescribed mesh displacement is assigned to all other boundaries. Moving mesh velocity is defined proportional to electric field.

a)

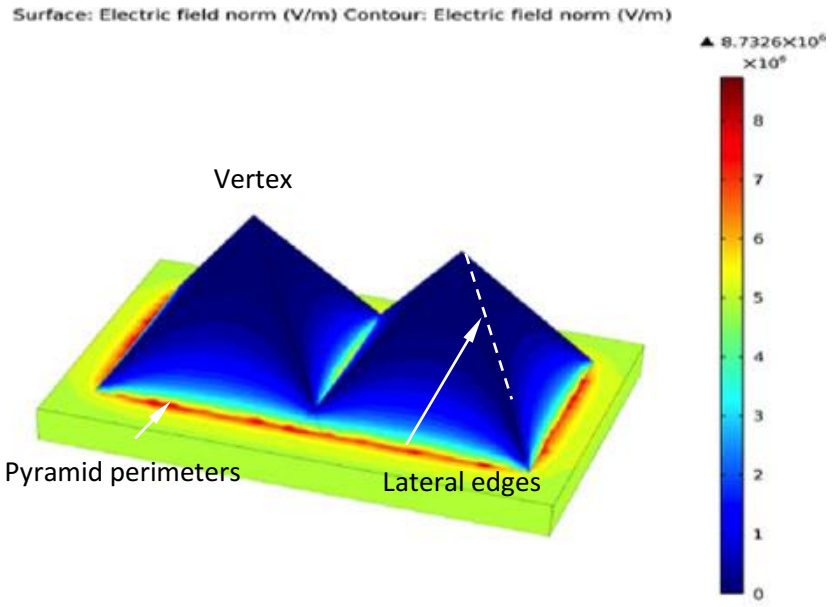

b)

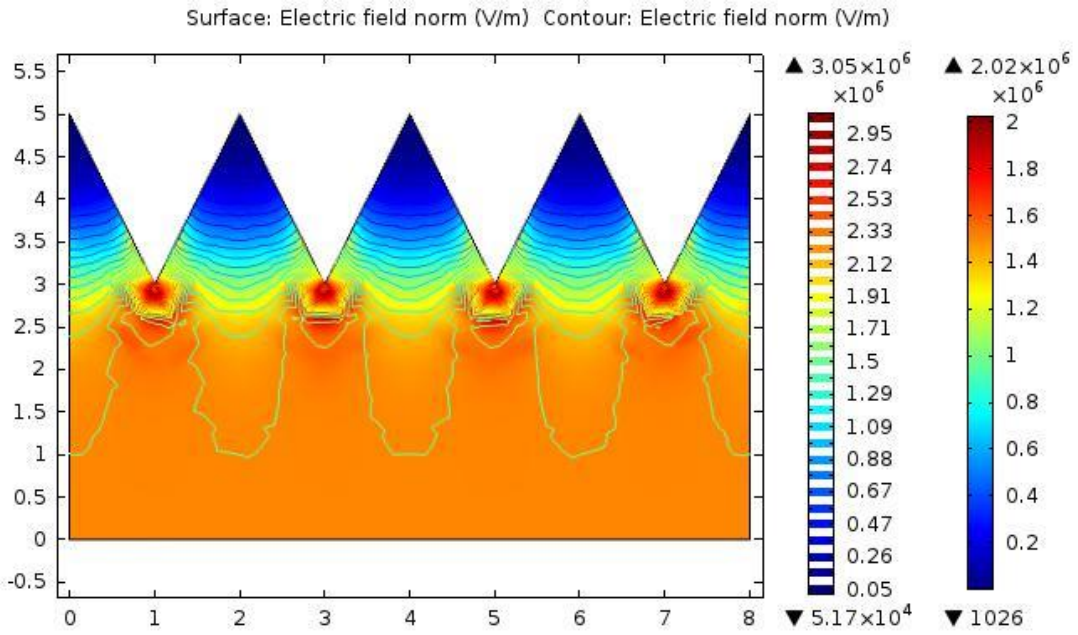

Figure 3. 7 Distortion of the electric field in textured Si. (a) 3D, (b) 2D. The electric field strength is not uniform and the lowest belongs to vertex and sides and the highest will be at pyramid perimeters.

Figure 3.8 clearly shows that the etching and developing porous silicon start at the edges of the pyramids bases where the electric field has maximum value.

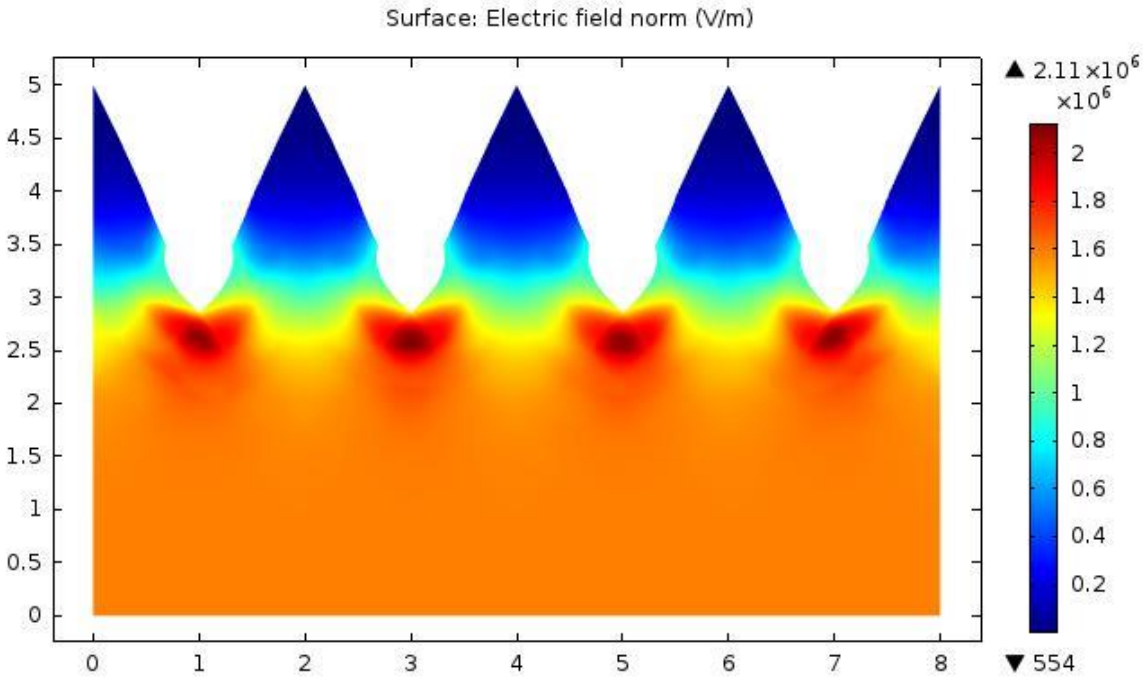

Figure 3. 8 (After Abedini Sohi and Kahrizi [66]) Resulting geometry and electric field distribution at the beginning of the etching process. Etching starts from the pyramid perimeters due to high electric field.

As etching continues the depth and the width of the pores become larger (Figure 3.9.a) and generates cavities around the pyramid bases. At this point arrow shape tips starts to form. The diameter of the nanostructures gets smaller as the etching continues (Figure 3.9.b).

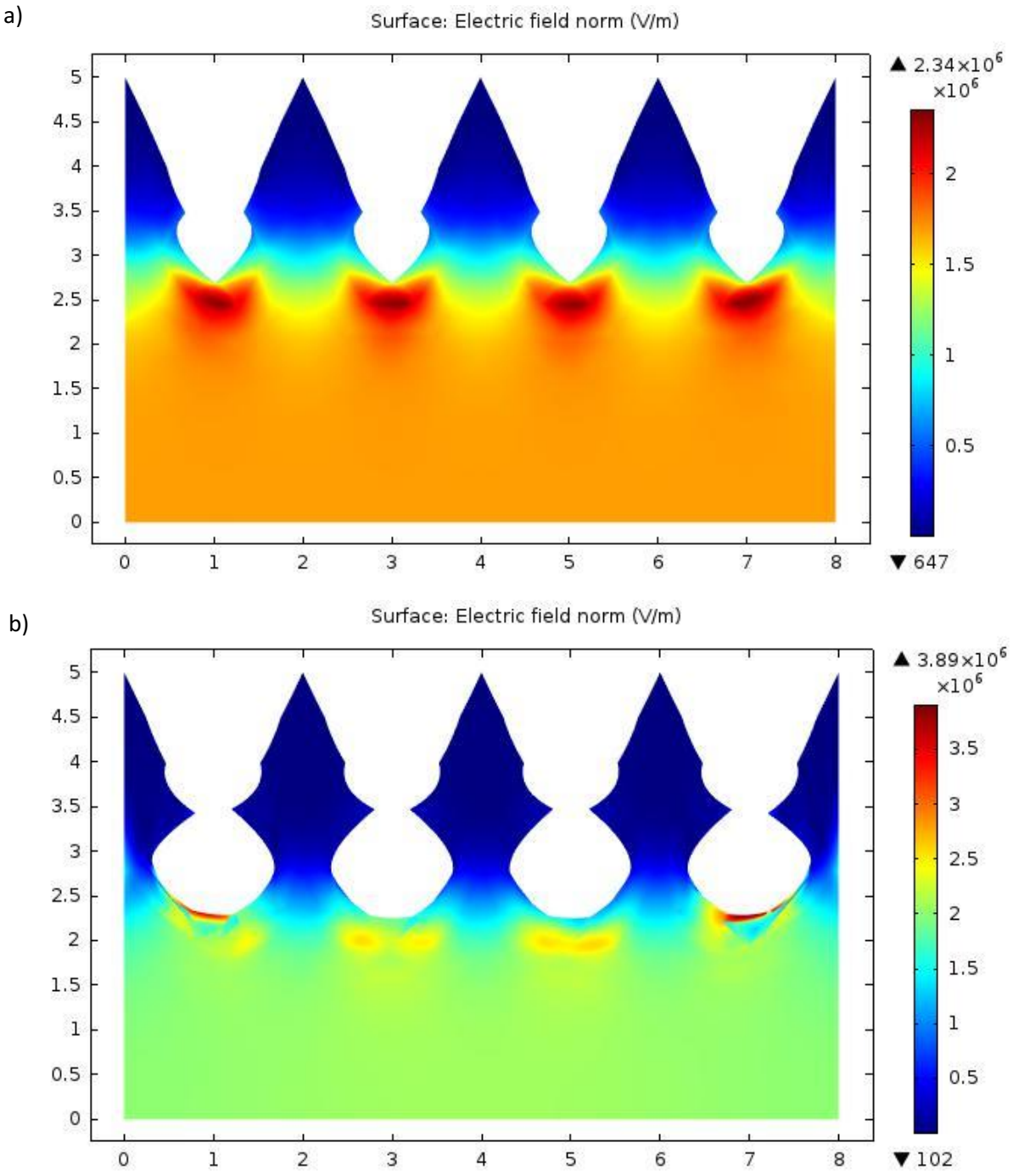

Figure 3. 9 (After Abedini Sohi and Kahrizi [66]) a) Resulting geometry and electric field distribution after 10 minutes etching. At this stage the arrow shape tips are formed, b) Resulting geometry and Electric field distribution at the final stage.

To study the evolution of nanowires experimentally, textured silicon samples shown in Figure 3.3.e, are subjected to a very slow electrochemical dissolution with a low anodic current density (10 mA/cm^2), in 1:3 HF to ethanol ratio, for etching periods of 20, 40 and 60 minutes. As it is shown in Figure 3.10, etching starts from the bases of the pyramids creating cracks at the hillocks intersections. The observations are in good agreement with our analytical results shown in Figure 3.8.

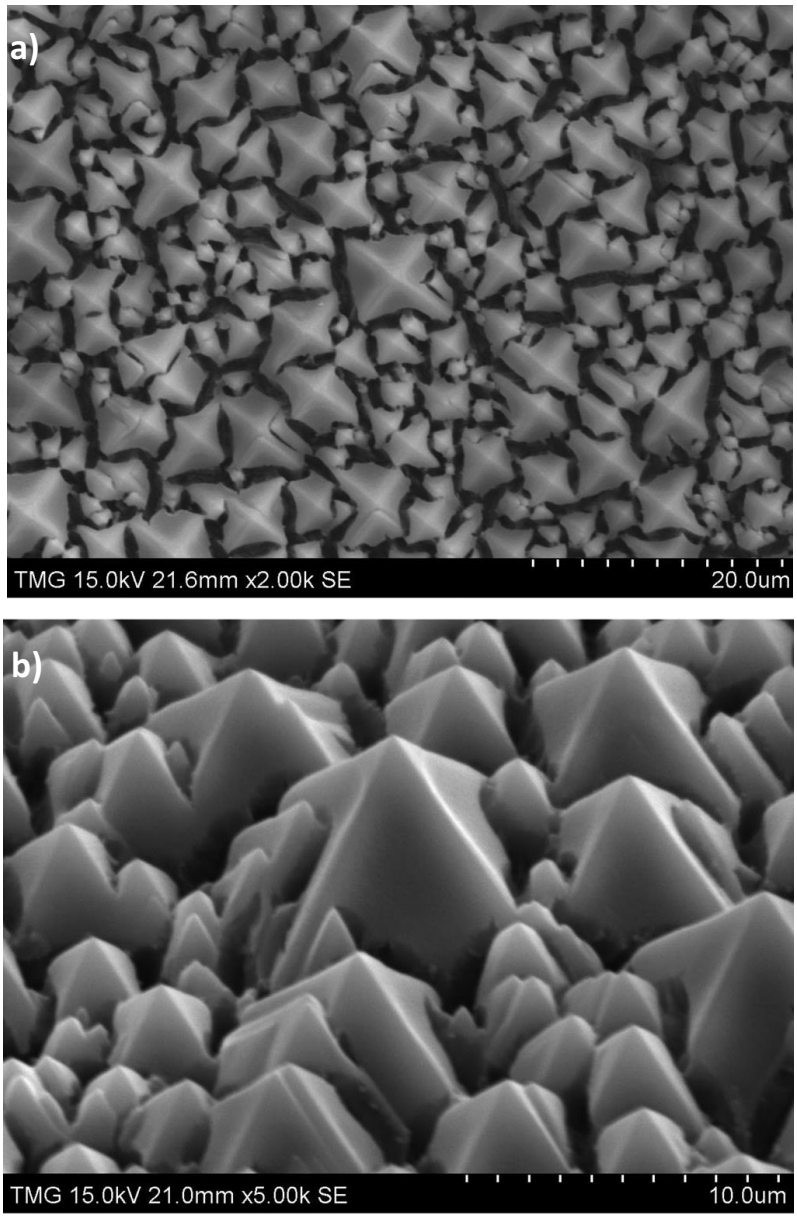

Figure 3. 10 Textured Si etched for 20 minutes in 10 mA/cm^2, (a) Top view (b) 50 degree tilted view. Etching started at pyramid edges resulted in a wide crack.

Figure 3.11 shows that by increasing the etching time to 40 minutes the separation between the pyramids became wider and pyramid faces started to dissolve while vertex remain unetched. Arrow-shape tips of nanowires in Figure 3.9.a can be clearly seen in experimental results shown in Figure 3.11.

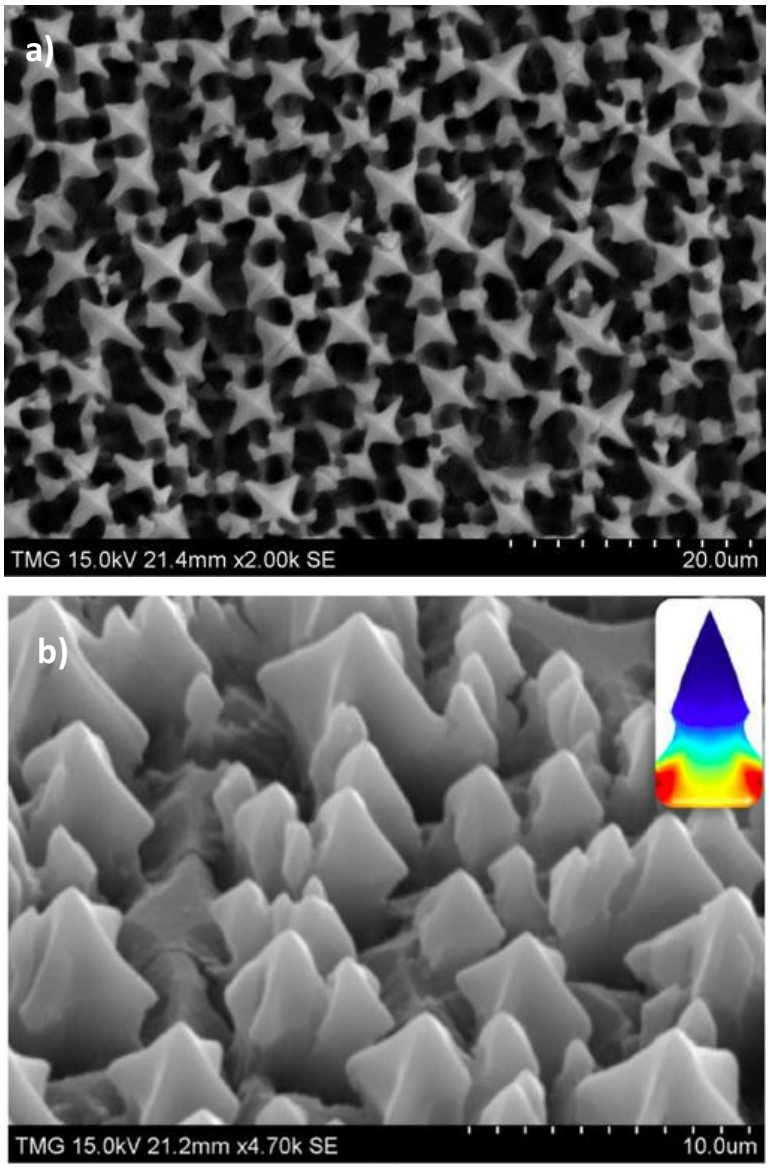

Figure 3. 11 (After Abedini Sohi and Kahrizi [66]) Textured Si etched for 40 minutes using a current density of 10 mA/cm^2 , (a) Top view(b) Tilted view, the inset shows the simulated partially etched structure which is comparable with experimental results.

Figure 3.12 shows the developed nanowires after 60 minutes etching structurally compatible with simulation results as it is shown in the inset of the figure. Obviously the longer the etching time the larger the aspect ratio of the nanowires however, as the etching continues the nanowires diameters get narrower particularly at the bottom of the structures and some of the nanowires

will break and fall down, reducing the concentration of the nanowires. As a result there must a limit to the etching time if the concentration of the nanowires (for specific applications) is a matter of concern.

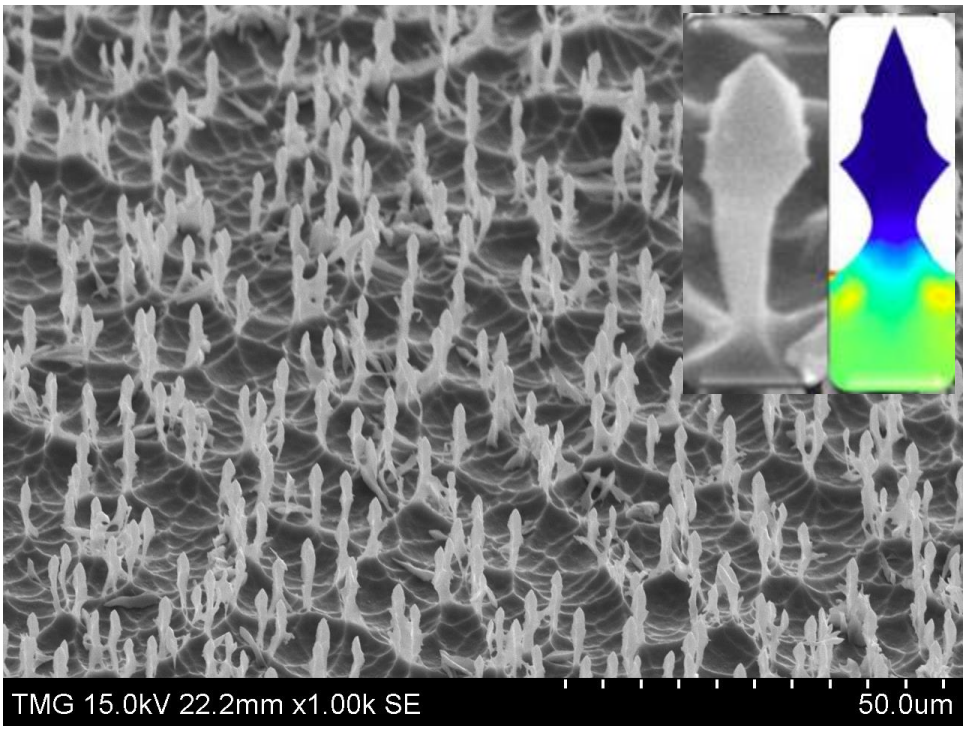

Figure 3. 12 Tilted view of developed nanostructures the inset shows the simulated etched nanowire to compare with experimental result.

There is always a trade off between the nanowires aspect ratio and their concentrations. The nanowire arrays shown in figure 3.12 are achieved by anodic etching of the textured silicon samples (shown in figure 3.3.e) for 60 minutes. Considering the concentration of the large pyramids shown in figure 3.3.e, and their separation intervals, one can say that they are comparable with those of the nanowires shown in figure 3.12. So, it can be concluded that the large pyramids are eventually developed to nanowires during the anodic etching, and smaller

pyramids were completely etched away during the fabrication. For this reason the density of the nanowires, their sizes and the separation distance between them can be controlled by the pyramidal structure of the samples developed during the first step of the fabrication. As a result, the textured samples grown in the first step of the fabrication has significant effects on the final structures of the nanowires. The more uniformity of the pyramids (in terms of size and distribution), generates structures with more uniform geometries.

3.2 Formation mechanism of the structures: 3-dimensional

A 3D analytical study has been carried out to better understand the abiding property of the lateral edges. A 3D structure containing several pyramids with various sizes is considered as the simulation geometry. Equation 3.1 confirms the dependence of the etching rate with the electric field strength. Here due to uneven textured Si surfaces, the electric field is not uniform at the interface. As a result, the hole drift current density is not uniform over the surface of the samples and different areas are experiencing different dissolution rates during the anodic etching.

The initial electric field distribution is shown in figure 3.13, when voltage is applied to the backside of the textured Si. Simulation results show that the electric field is lowest at the tips and lateral edges of the pyramids, and has the highest strength at the pyramid perimeters.

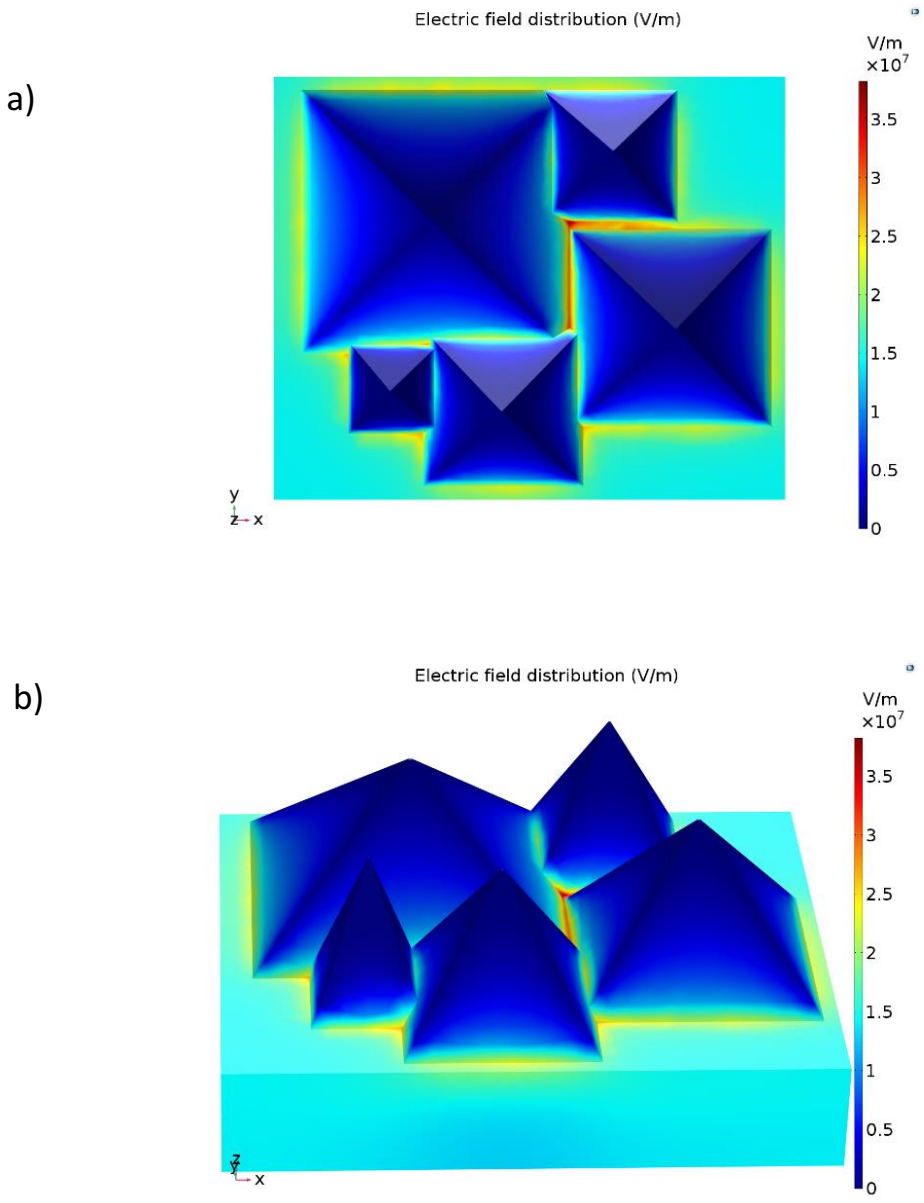

Figure 3. 13 (After Abedini Sohi and Kahrizi [69]) Distribution of electric field in the textured Si surface is simulated by COMSOL electrostatics module. a) top view and b) tilted view of the 3D structures shows that the electric field strength is not uniform and the lowest belongs to vertex and sides (shown by dark blue) and highest is for pyramid perimeters (shown in yellow/red).

To present the development of the structures, COMSOL deformed geometry (dg) physics interface is applied to all domains. A prescribed mesh velocity is assigned to the boundary between Si and electrolyte (pyramidal texture) and a prescribed mesh displacement is assigned to boundaries all around the block. Moving mesh velocity is defined proportional to electric field.

Figure 3.14 clearly shows that the etching and developing porous silicon start at the edges of the pyramids bases where the electric field has the maximum value.

As the etching extends, pyramid faces are etched away while lateral edges remain as connecting walls between the pyramids. Figure 3.15 clearly illustrates the residual walls between the structures.

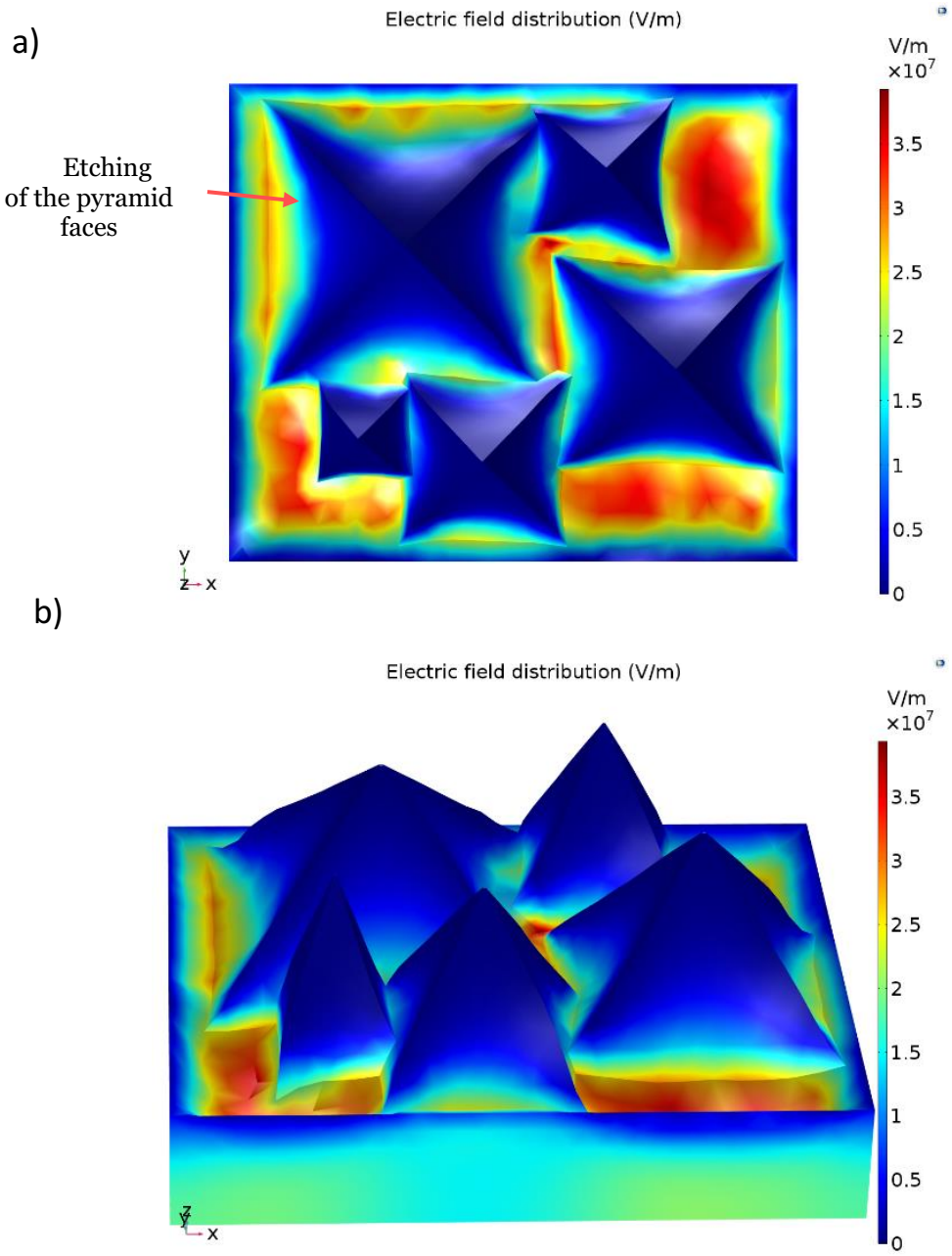

Figure 3. 14 (After Abedini Sohi and Kahrizi [69]) a) Top view and b) Tilted view of COMSOL deformed geometry. The figures show that as the etching starts, pyramid perimeters are experiencing higher etching rates due to higher electric filed strength.

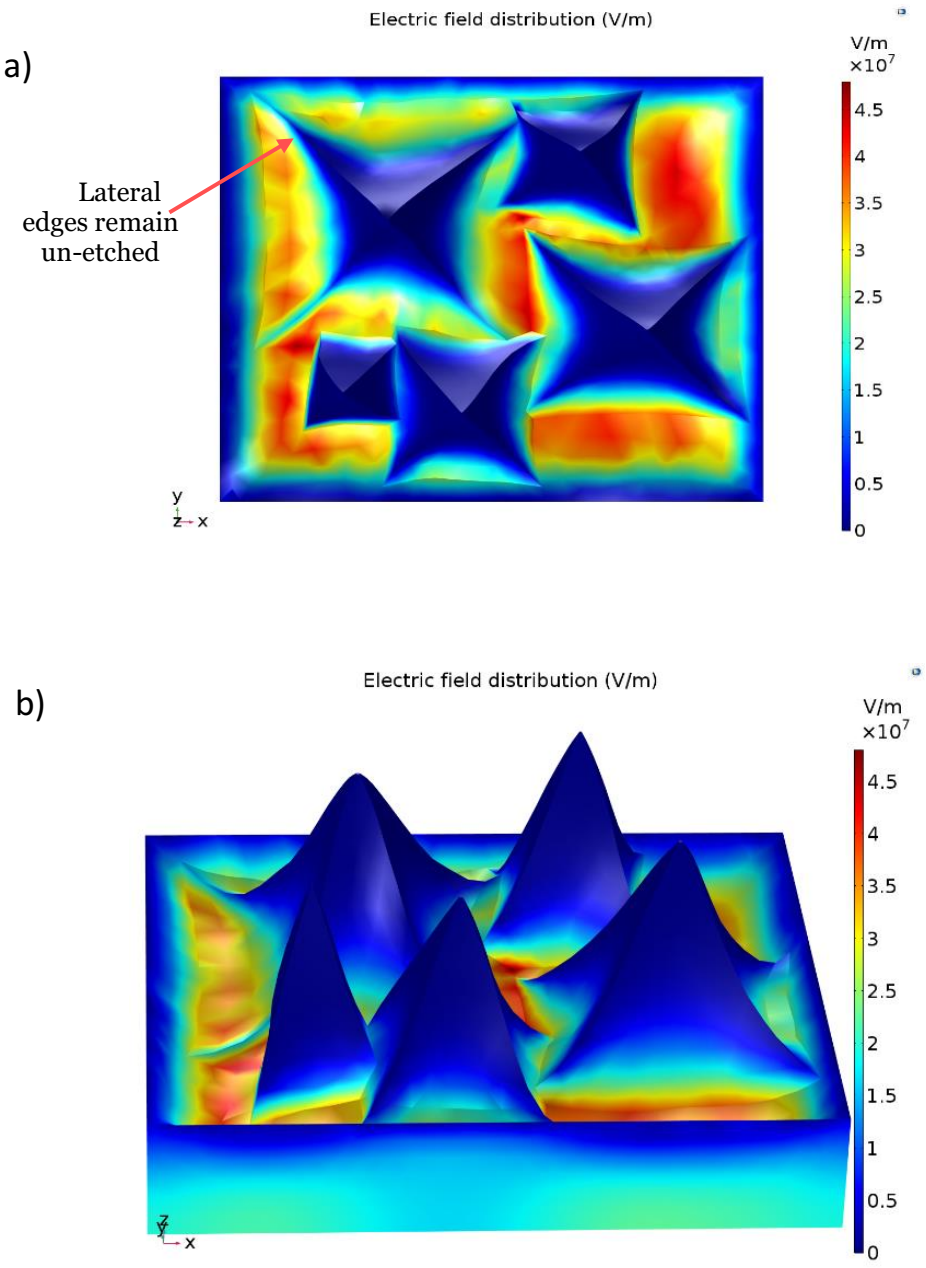

Figure 3. 15 **(**After Abedini Sohi and Kahrizi [69]) COMSOL deformed geometry shows that the extended etching results in residual walls around the structures, while pyramid faces are etched away. a) Top view, b) Tilted view.

3.3 Controlled growth of freestanding silicon nanostructures

3.3.1 Isotropic etching current density

As it is explained in section 3.1, to fabricate the nanostructures, textured samples, which are prepared in the first step during anisotropic etching process, will be exposed to isotropic electrochemical etching process.

Porous silicon is formed by electrochemical silicon etching in HF solutions under anodic polarization. Porosity of silicon depends on anodization conditions such as HF concentration, current density and resistivity of the sample [67], [68]. It is found that the average pore diameter depends on applied current density and it increases with increasing current density [70]. In this work to obtain the nanostructures, Si samples covered by pyramids (etched under anisotropic condition in the first stage) are isotropically etched in 1:3 HF-ethanol solutions. As it is explained in section 3.1 the pores formation starts at the edges of the pyramids due to the higher hole current density at those places. The diameters of the generated pores are dependent on the applied current density. For example, in figure 3.16 we show the SEM images of the pores generated on a sample like the one shown in figure 3.3.d, for various applied current density. In figure 3.16.a, we show a sample that was etched applying 50 mA/cm^2 anodic current density for 12 minutes, while figure 3.16.b shows the result of etching a similar sample when we applied 10 mA/cm^2 for 60 minutes. As one can see, although the total charge density, $Q = I \times t$ remained the same but the size of the pores in two cases are not comparable.

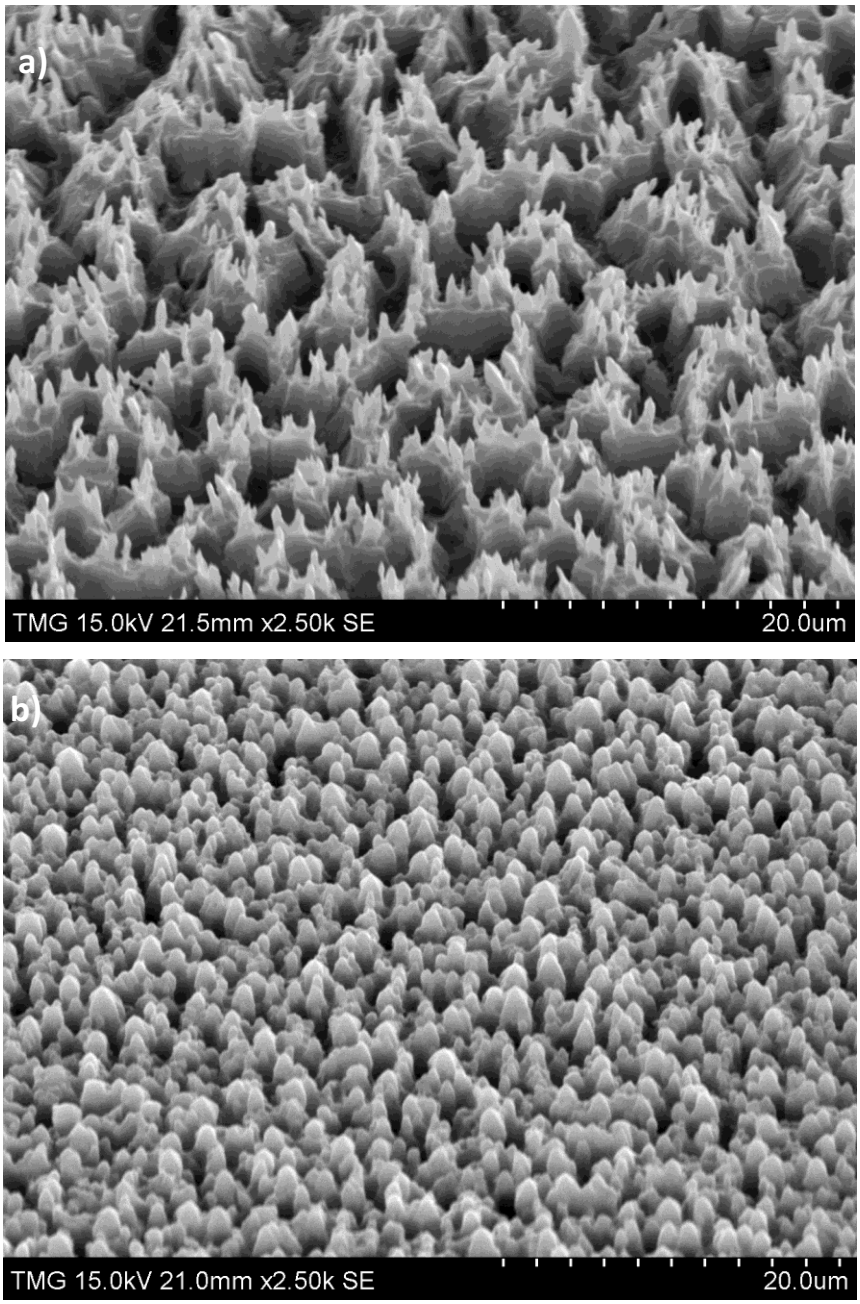

Figure 3. 16 (After Abedini Sohi and Kahrizi [65]) a) Large pore formation at high current densities (about 7-8 µm) which eliminates the formation of NWs. b) proper pore size comparable to pyramids perimeters which results in formation of nanowires eventually.

Our studies show that larger current density produces larger pores around the structures. As the large pores may completely have wiped out the pyramids, we have found that in order to generate free standing nanostructure at the end of the process we should apply a current between the two electrodes proportional to the size of pyramids. Our experiments show that to keep the pyramids with base dimensions smaller than 2 μm we should not apply a current density more than 5 mA/cm^2 (it should be mentioned that this value depends on the wafer resistivity). Applying higher current densities may eliminate most of the pyramids during this etching process. It is also found out that current density applied on the samples covered with pyramids with average size of 2-3 μm, and 5 μm should be around 10, and 15 mA/cm^2 respectively.

Samples, which are anisotropically etched and shown in figure 3.3.e, are now exposed to isotropic etching in HF/ethanol solution when we applied a current density of 15 mA/cm^2 on the sample for 30 minutes. Figure 3.17 shows the top view of the etched sample. The inset figure shows the early stages of pore formation around the pyramids with diameters in range of pyramids' perimeters. As it can be seen, etching starts from the pyramid edges and continues toward pyramid faces. The tips of the pyramids remain unetched and form the tip of the structures.

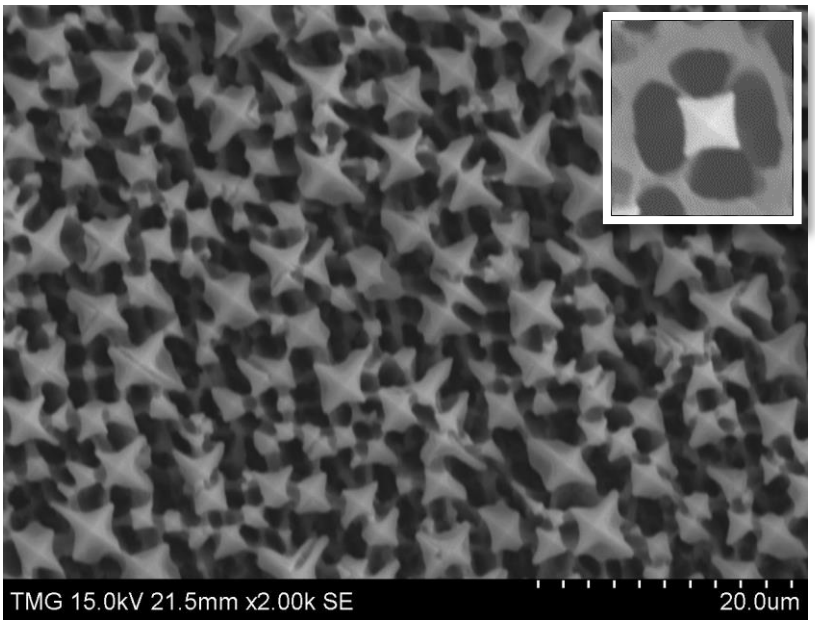

Figure 3. 17 Top view of the etched samples with 15 mA/cm^2 for 30 minutes. Inset figure shows that the pore sizes are comparable with smallest pyramid perimeters due to proper current density**.**

As the process of etching continues, (the etching time is extended to 60 minutes), the pores become wider and the thickness of separating wall between the pores becomes smaller. Etching is continued until the connecting walls between the most pores are etched away (as it is seen some of the walls between the larger pyramids are still remained intact, to remove them we will proceed to step 3 of the process). Figure 3.18 compares isotropically etched samples with large and small pyramids (the samples that are shown in figure 3.3.e and 3.3.d respectively) for 60 minutes in 15 and 10 mA/cm^2 respectively. As it can be seen the density and the tip-to-tip separation of the nanostructures correlates with the pyramids.

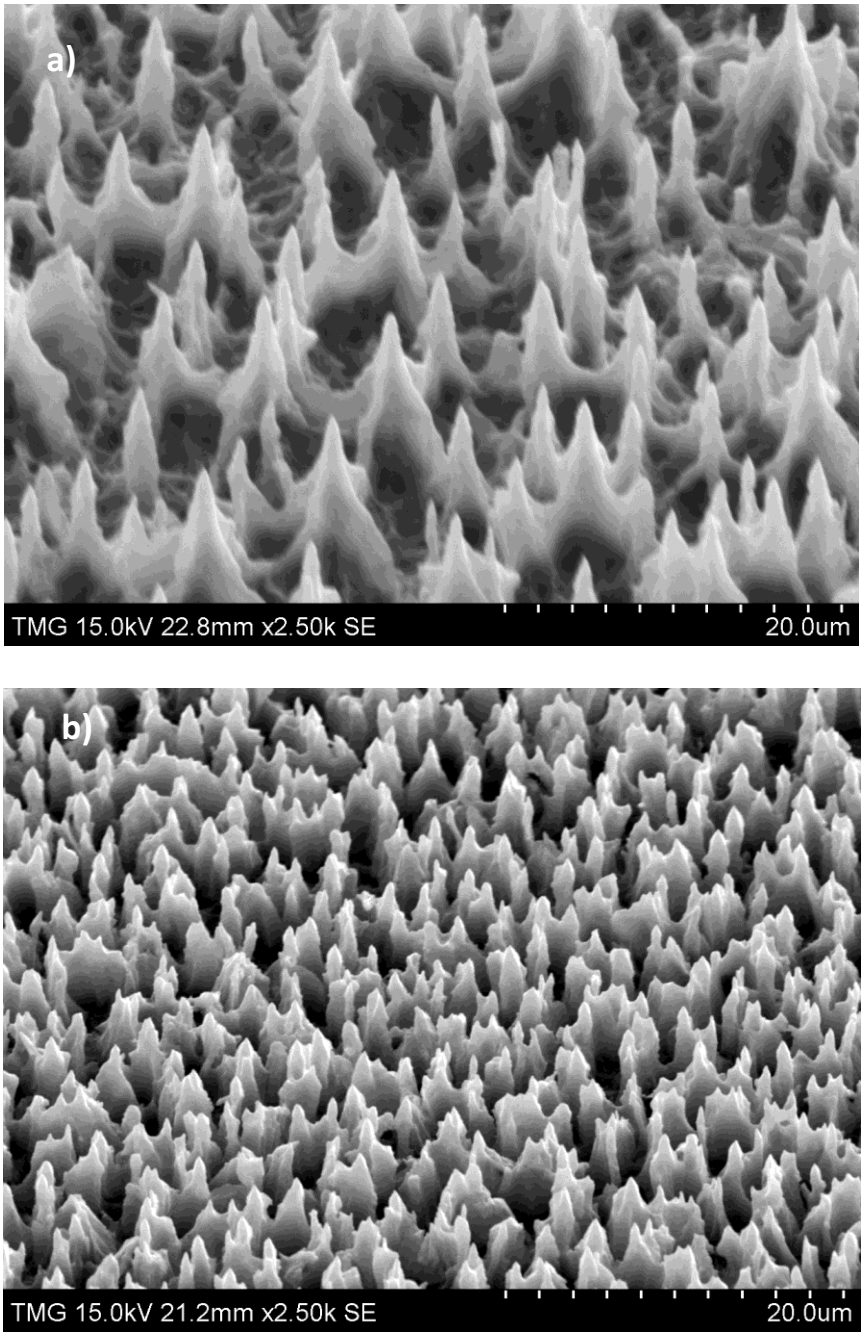

Figure 3. 18 (After Abedini Sohi and Kahrizi [65]) Second step of the growth process (electrochemical etching in 1:3 HF/Ethanol solution for 60 minutes). a) Using large pyramids shown in figure 3.3.e etched under applied 15 mA/cm^2 b) using small pyramids shown in figure 3.3.d etched under applied 10 mA/cm^2.

3.3.2 Fine anisotropic chemical etching

To remove the connecting walls and residual between the structures shown in figure 3.18.a and 3.18.b, samples are subjected to another anisotropic etching in a weak etchant (low concentration of 1wt% of TMAH and 1wt% of IPA) for 2 minutes. The results are shown in figure 3.19.a and 1.19.b respectively. As it can be seen the tip-to-tip separation between the structures remains the same in all steps (see the sample with large pyramids, processed in various steps that are shown in figure 3.3.e, 3.18.a and 3.19.a, and also the sample with small pyramids, structures shown in figures 3.3.d, 3.18.b and 3.19.b).

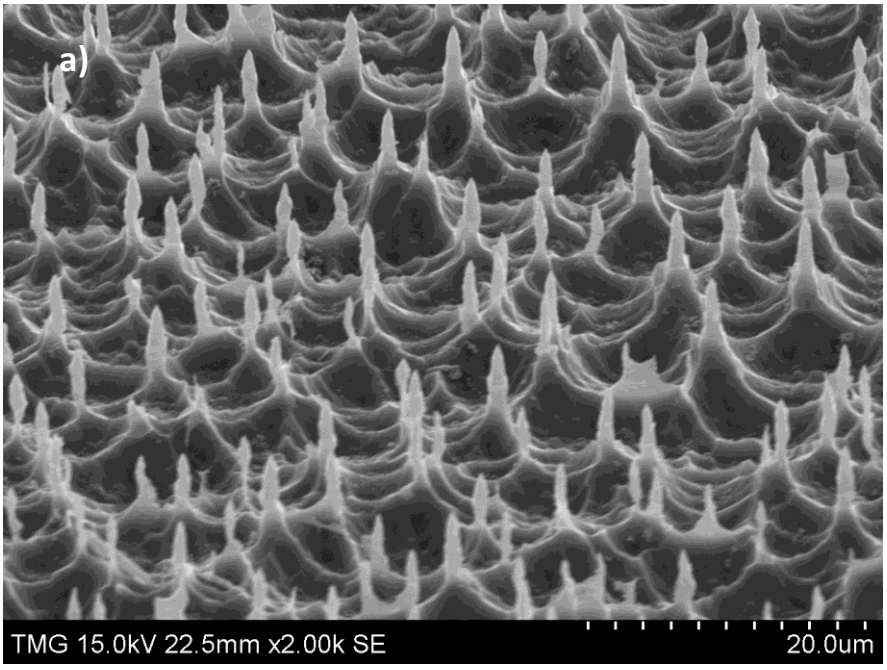

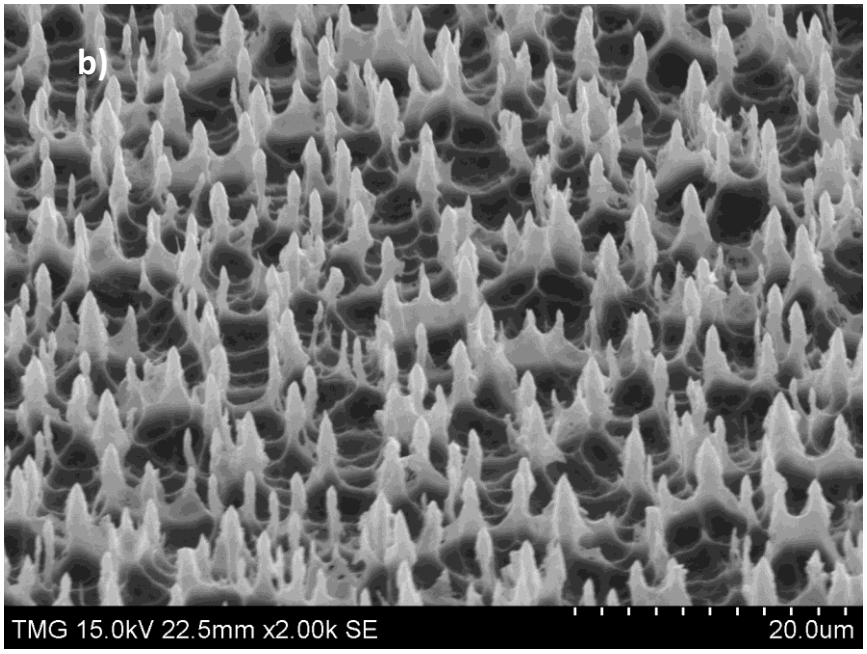

Figure 3. 19 a) Sample shown in figure 3.18.a etched in 1/1 wt% TMAH/IPA solution for 2 minutes. b) Sample shown in figure 3.18.b etched in 1/1 wt% TMAH/IPA solution for 2 minutes.

It should be mentioned here that period of etching in this step is very important. Structures shown in figure 3.19.b are generated when we etched the samples in this step for 2 minutes while sample shown in figure 3.20 is etched for 3 minutes.

Increasing etching duration results in a much thinner and lower concentration of nanostructures (as smaller structures are etched away). Longer etching process may eliminate most or all the nanostructures.

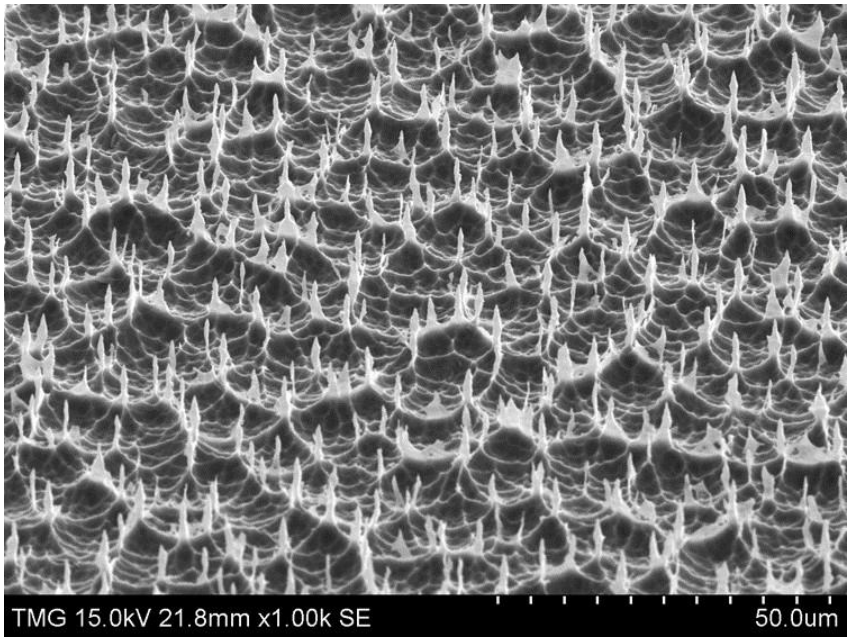

Figure 3. 20 Longer etching duration in the last stage results in lower concentration of nanowires and thinner structures.

3.4 Conclusion

In this chapter we described development of silicon nanowires using a mask-less, chemical/electrochemical etching technique. The etching mechanism of the nanowires is investigated analytically (utilizing COMSOL) and experimentally. Detail studies on growth mechanism of the nano-tip structures helped us to adjust the fabrication parameters to control the characteristic as well as the density and concentration of the structure arrays.

In summary, it is demonstrated that positive carriers (holes) current density greatly influences the etching rate of the silicon during the electrochemical etching process. Using modeling of the pyramids and simulations of electric fields between electrodes, it is shown that due to non-uniform electric field intensity (resulting in a non-uniform hole current), the etching rate is not uniform along the surface of the textured silicon sample. Etching of the samples is first started by generating narrow cavities at the perimeters of the hillocks, where the electric filed has the

maximum value due to edge effect. The results of the simulations and experiments show that as the process continues, the depth and the width of these cavities become larger, initiating the growth of the structures.

It was also concluded that the aspect ratios as well as the concentrations of the silicon nanostructures are very dependent on size and concentration of the pyramids, which are prepared in the first step (anisotropic etching process). Therefore, in this study anisotropic etching of silicon in various combinations of TMAH/IPA solutions is studied emphasizing on how to control the average size and the concentration of the hillocks. Generally, as more TMAH is added to the etchant solution, larger pyramids are generated on the surface. However, the results show that samples etched in a very low concentration of TMAH are covered with non-uniform and low concentration of the pyramids, while the samples etched in very high concentration of TMAH give rise to collapsing pyramids, merging into the surface and leaving rough patches on the surface.

The process followed by isotropic etching of the textured silicon samples in HF/ethanol solutions to generate pores along the height of the pyramids. The experimental results show that the formation of pores happens at any applied current density in the anhydrous electrolyte. However, as the large pores may eliminate many small nanostructures, to optimize the population of the nanowires, the applied current should be adjusted to produce pores with sizes comparable with the size of pyramid perimeters.

At the final stage of fabrication, we may need a fine etching to remove the un-etched sidewalls grown between the pyramids. The results showed that there is a correlation between the number of pyramids generated in the first step of the process and nanostructures produced at the last stage of the process.

Chapter 4
Theoretical background on Gas Ionization Sensors

4.1 Gas Ionization

Gas Ionization sensors are based on fingerprinting the discharge properties of the gases. These properties such as breakdown voltage and tunneling current are unique values for each gas at specific pressure. So in this section the discharge characteristics of the gases in a parallel plate system is elaborated. Breakdown voltages in parallel plate systems for both cm-scale and μm-scale separation gaps is reported base on Paschen's law and modified Paschen's Law and finally the field enhancement approaches to reduce the breakdown voltages is explained. *Gas ionization* is the process in which gas atoms lose electron and form negative ions. Ionization, under the effect of applied electric field; result in a flow of electric current, which is called *electric discharge of the gas*.

Under normal condition, due to cosmic rays and ultraviolet radiations, there are some ionized atoms in the air. Applied electric field separates the charges and generates a current proportional to electric field strength. The current due to radiation-generated particles is extremely small so the gas is considered as an insulating medium. By increasing the electric field to a certain value, a sudden rise of current occurs. The transform of the insulating state to the conductive state is called *gas breakdown* [23], [71].

4.2 Discharge Characteristic of the Gases

Figure 4.1 shows the insulation-to-conduction transformation of the gas, using voltage-current (V-A) characteristics of electrical discharge. This is a general V-A curve when uniform electric field is induced between two parallel electrodes [71].

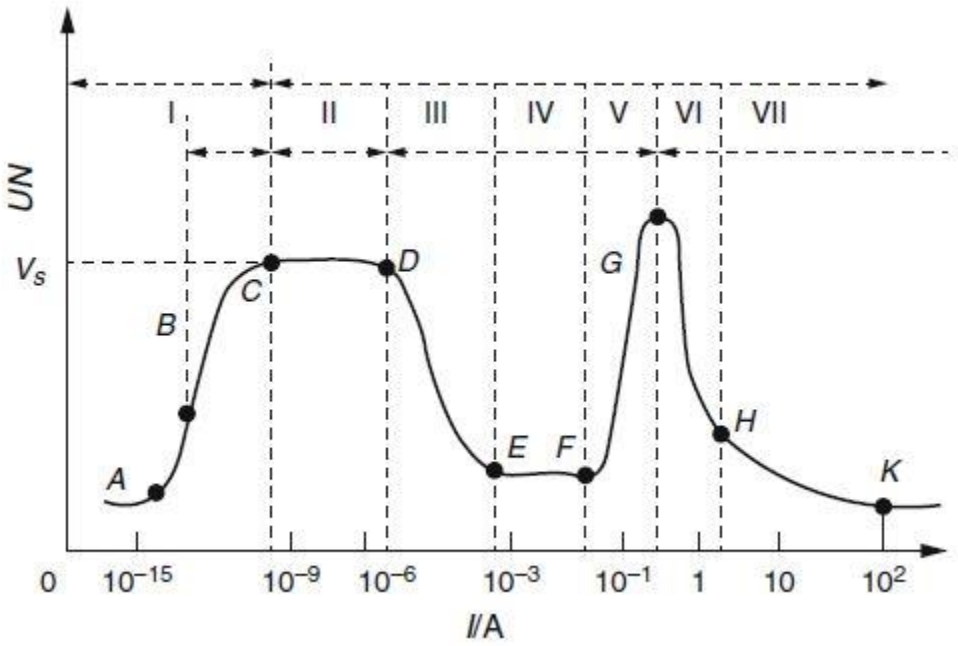

Figure 4. 1 (Adopted from Xiao [71]). Different states of gas discharge in a uniform electric field.

The V-A can be divided into seven regions. In region I, when the voltage is applied to the electrodes, the radiation-generated charged particles generate current as charged particles are travelling toward the electrodes (electrons migrate to anode and ions move toward cathode, they will be neutralized through external circuit). This region is also called a non-self-sustaining discharge, as the ionizing source is an external radiation such as cosmic ray or ultraviolet light (applied voltage just stops the recombination and separates the charged particles). In this region the current is increasing with the increase of applied voltage. Between points A and B the current

reaches its saturated value which means that all radiation-generated particles are attracted to the electrodes. By increasing the applied voltage, the current raises exponentially (BC segment) which is called Townsend discharge phase. At this phase the electric field strength would be enough to accelerate the electrons and result an ionizing collision. In region II (CD segment) the discharge can be maintained only by the ionizing collisions without any external ionization source, so this region is called self-sustaining dark discharge. Point C of this region corresponds to the breakdown voltage. In region III the system is showing a negative resistance property due to reduced voltage drop across the gap, which reaches a steady state on region IV (sub-glow discharge and eventually glow discharge). In the next region (V) the current increases exponentially with voltage, this area is called the abnormal glow discharge area. If the discharge current continues to increase, the discharge converts to an arc discharge region, which has negative resistance properties. Discharging gas in arc discharge is high-energy plasma (VI and VII) [71].

4.3 Gas Breakdown

In figure 4.1, the transition from region “I” (known as non-self-sustaining discharge) to region “II” (known as self-sustaining discharge) is called gas breakdown. This transition is called Townsend discharge. Due to Townsend mechanism, applied electric field accelerates the liberated electrons and results in subsequent ionizing collisions. These collisions result in an avalanche multiplication of electrons, which contributes in gas electrical conduction.

4.4 Townsend Discharge Theory

In 1903, John Sealy Townsend proposed a discharge theory (known as Townsend discharge theory), which based on three concurrent processes:

1) Impact ionization: Electrons are energized and accelerated due to high electric field and collide with other gas atoms, ionize and generate large number of electrons.

2) In like manner, positive ions have ionizing collisions when moving toward the cathode.

3) Secondary emission: Bombardment of the cathode by energized positive ions induces an electron emission from the cathode surface.

Townsend allocated α, β and γ coefficients to above mentioned ionizing processes respectively. These coefficients characterize the quantity of gas ionization in each process. α, *Townsend's first ionization coefficient*, defines as average number of ionizing collision by an electron travelling 1 cm. *Townsend's second ionization coefficient*, β, is the positive ion ionization coefficient per 1cm displacement (in normal discharge β≈0 as positive ions are much larger than electrons the probability of gaining sufficient acceleration to make ionizing collisions is very small). γ, *Townsend's third ionization coefficient*, is the average number of secondary emitted electrons from the cathode when positive ions strike the cathode surface [23].

Regarding α process (impact ionization), if d_x is considered as a thin layer inside the gap between the electrodes, and n_{e0} is the number of electrons coming into the layer, d_x layer produces dn_{ex} electrons due to α process:

$$dn_{ex} = n_{e0} \times \alpha \times d_x \tag{4.1}$$

At x=0, n_{e0} is the total number of electrons emitting the cathode, an integration of equation 4.1 is:

$$n_{ex} = n_{e0} e^{\alpha x} \tag{4.2}$$

The total number of electrons due to α process in the discharge region (when d is the total inter-electrode separation gap) can be calculated by:

$$n_{ea} = n_{e0} e^{\alpha d} \tag{4.3}$$

The α process-current at the anode is:

$$i_{e\alpha} = i_{e0} e^{\alpha d} \tag{4.4}$$

As it can be seen the current is exponentially growing with distance from cathode.

At this point, there are $n_0(e^{ad} - 1)$ positive ions generated during the α process, which strike the cathode and induce secondary electrons (known as secondary emission). The concentration of secondary emitted electrons is the concentration of positive ions increased by a factor of γ:

$$n_0(e^{ad} - 1) \times \gamma \tag{4.5}$$

Each of these released electrons contributes in α process again and accordingly (considering several generations) equation 4.6 gives the total electron current reaching the anode for planar electrodes.

$$i_{ea} = \frac{i_{e0} e^{ad}}{1 - \gamma(e^{ad} - 1)} \tag{4.6}$$

4.5 Self-Sustained Discharge Condition

In equation 4.6 if it is considered that there is no initial carrier generation, $i_{e0} = 0$, the electron current would be zero unless the denominator becomes zero:

$$\gamma(e^{ad} - 1) = 1 \tag{4.7}$$

Equation 4.7 states the self-sustained discharge condition proposed by Townsend. This condition states that if primary electrons produce secondary emitted electrons, a self-sustaining discharge takes place. If they do not induce secondary emitted electrons the current will terminate after neutralization of α produced electrons through the external circuit. This condition is also known as breakdown criterion.

4.6 Paschen's Law

Townsend's first ionization coefficient, α, is a function of electric field (E), gas pressure (P) and gas characteristics (A, B are constants defining the gas properties). It can be written as:

$$\frac{\alpha}{P} = A \exp\left(\frac{-B}{E/P}\right) \tag{4.8}$$

Neglecting -1 (very initial electron) in equation 4.7 we have:

$$ad = ln(1/\gamma) \tag{4.9}$$

Considering uniform electric field inside a planar electrode discharge system, $E = \frac{V_s}{d}$, and equations 3.8 and 3.9, the equation for breakdown voltage is:

$$V_s = \frac{BPd}{ln\left[\frac{APd}{\ln(1/\gamma)}\right]} \tag{4.10}$$

Where A, B and γ are constants and the breakdown potential, V_s, is a function of Pd product. The relationship of V_s and Pd is known as Paschen's law. Figure 4.2 shows the relationship of V_s and Pd for various gas with planar electrodes.

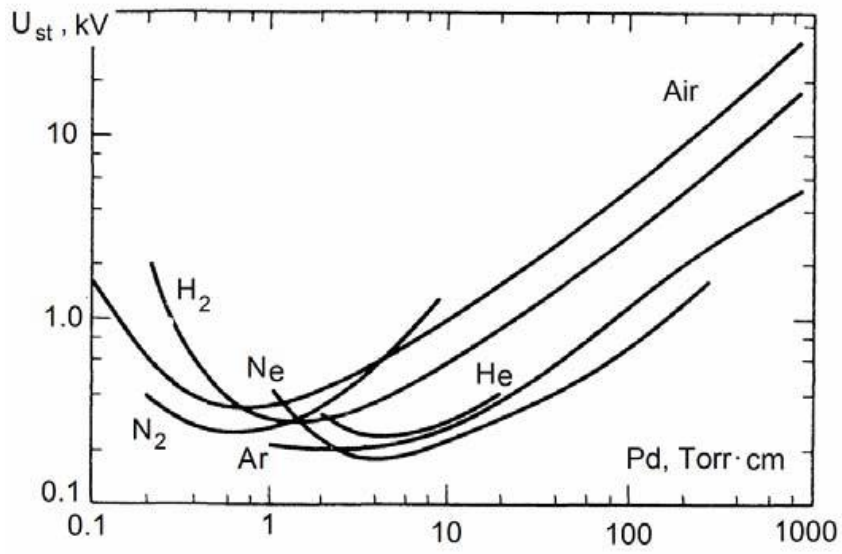

Figure 4. 2 Breakdown voltage vs Pd [72].

4.7 Modified Paschen's Law

In later experimental studies [26] , it was revealed that Paschen's Law is applicable when the electrode separation is in cm range (large scale systems) and the breakdown voltage is lower (in several hundred-volt range) than Paschen's Law for micro-gap devices. It was marked that extremely high electric fields in micro-gap systems results in field emission from the cathode. Field emission effect causes the reduced breakdown voltage in micro-gap systems.

Lisovskii *et al.* [24] obtained a modified Paschen's law as a function of both $p \times L$ (product of pressure and inter-electrode gap width) and L/R (inter-electrode gap width/ radii of the discharge chamber). They also claimed that Paschen's law is valid only for discharge tubes in which, electrodes radii and gap width have similar dimensions. The breakdown of argon in approximately 10^{-2} Torr was reported around 800 V, which is much lower than predicted values by Paschen's law.

Boyle *et al.* [25] reported the failure of Paschen's law for small inter-electrode gaps and formulated a new criterion for this case. Figure 4.3 shows the breakdown voltage of the gases against $p \times L$ (product of pressure and inter-electrode gap width) and the region of the failure of the Paschen's law.

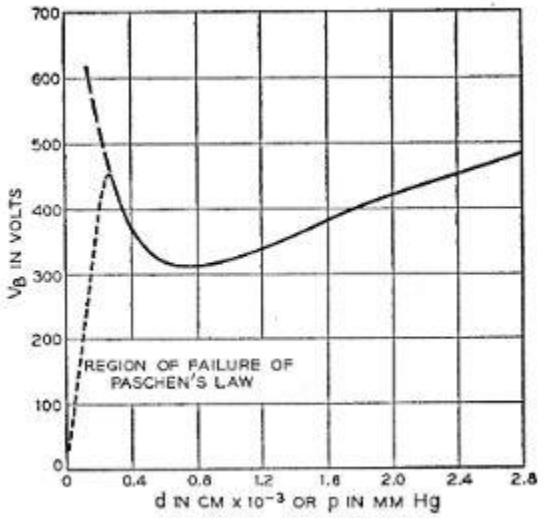

Figure 4. 3 (Adopted from Boyle *et al.* [25]). Breakdown voltage of the air vs L at 1mmHg (shown by dashed line), and against pressure at L=1cm (long-dashed line) to show the failure of Paschen's Law. Solid line shows the valid section of Paschen's law.

4.8 Geometrical Field Enhancement

As it is explained in the previous sections, electric field strength in the parallel-electrode gap is responsible for the breakdown of the gases. To scale down the breakdown voltage of the gases, 1D nanostructures could be applied as one of the electrodes. Enhanced local electric field is created at the tip of the structures due to non-uniform distribution of charged carriers.

In a conductive object, charged carriers are distributed in a way to reduce the effect of their repulsive forces. The force between two charged points (magnitudes of q and Q) can be calculated by Coulomb's law;

$$F = \frac{1}{4\pi\varepsilon_0}\frac{qQ}{r^2} \tag{4.11}$$

which states that the force between the charged carriers is inversely proportional to the square of the distance (r) between them. According to equation 4.11 charges carriers would position themselves with the most distance from each other.

Potential of the conductor is the same all over the surface of the object. Charge distribution takes place until all the structure is at the same potential. In a uniformly shaped structure, such as spheres or absolutely flat surfaces, the carrier distribution is the same at any location along the surface. In an irregular shaped electrode, to preserve a constant potential, it implies that the surface charge density is higher at sharper edges. This can be explained by the potential due to point charge:

$$V = \frac{kQ}{r} \tag{4.12}$$

(where k is constant equal to 9×10^9 N· m^2/C^2), which shows as the object gets smaller (reducing radii, r), the surface charge concentration is increasing in order to keep the potential constant. The electric field is proportional to the local charge density so it would be maximum at sharp edges of the structure.

4.8.1 Effect of aspect ratio of 1D structures on electric field

The applied electric field between planar electrodes is a uniform electric field known as *applied macroscopic field* and is defined as:

$$E_{app} = \frac{V}{d} \tag{4.13}$$

Where V is the applied potential and d is the separation gap between the planar electrodes. Applying 1D nanostructures as one of the electrodes creates nonlinear electric field, enhanced at the vicinity of the tips of the structures. The field enhancement factor is defined as the ratio of E_{loc} to E_{app},

$$\beta = \frac{E_{loc}}{E_{app}} \tag{4.14}$$

Miller *et al.* [73] mathematically predicted the field enhancement factor of a protrusion situated on a planar surface with geometries shown in figure 4.4. In this study the scale of the protrusion was assumed much smaller than the scale of the experimental apparatus.

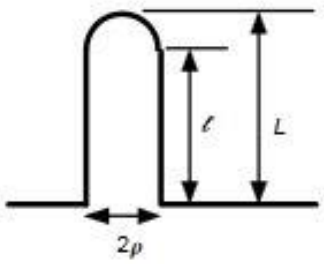

Figure 4. 4 Hemisphere on a post is geometrical/mathematical models for a field enhancing 1D nanostructure.[74]

Regarding the structure shown in figure 4.4, β is calculated by

$$\beta(d) = \beta|_{d=\infty}\left[1 - \frac{L}{d}\right] \tag{4.15}$$

Where d is the anode-cathode distance and $L = l + \rho$, in which l is the length of the post.

A unified expression of β can be written as:

$$\beta \approx 2 + \frac{L}{\rho} \tag{4.16}$$

If L>>ρ equation 4.16 reduces to a rough approximation:

$$\beta \approx \frac{L}{\rho} \tag{4.17}$$

The best estimation of the value of enhancement factor within ±3% can be calculated by:

$$\beta \approx 1.2(2.15 + \frac{L}{\rho})^{0.90} \text{ if } 4 \leq \frac{L}{\rho} \leq 3000 \tag{4.18}$$

And is valid within ±25% can be calculated by:

$$\beta \approx 0.7\frac{L}{\rho} \quad \text{if } 30 \leq \frac{L}{\rho} \leq 2000 \tag{4.19}$$

Figure 4.5 compares equations 4.18 and 4.19 and according to the author statement, equation 4.18 is a good approximation for smaller aspect ratios. [74]

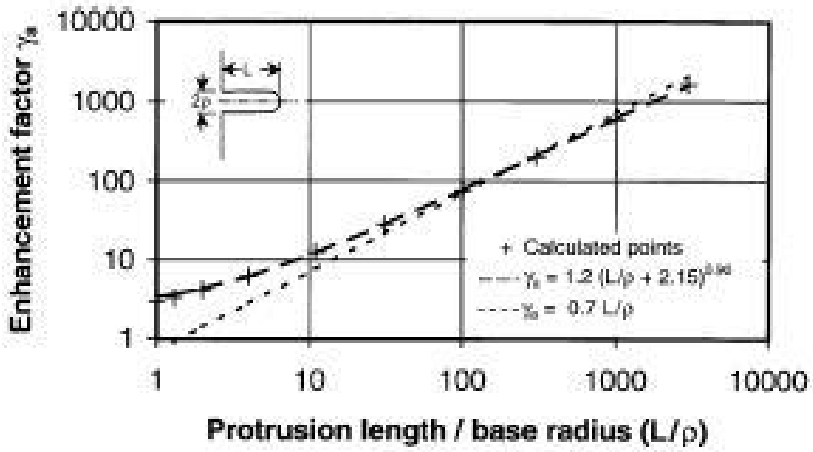

Figure 4. 5 Field enhancement factor of the apex of a *hemisphere on the post.* The graph compares equations 4.18 and 4.19. Equation 4.18 is a better approximation of the smaller aspect ratio ($\frac{L}{\rho}$) [74]

4.8.2 Effect of the shape of nanowire tips

Chivu *et al.* [46], [75] simulated the effect of the nanowire shapes on the intensity of the local electric field around the structures. In their research different tip shapes (such as semi spherical, ellipsoid, sharp triangle and T-shape) of an individual nanowire are considered as the

geometry in COMSOL simulation tool. According to their results the ellipsoid nanowire tip (figure 4.6.b) provided the best electric field enhancement of maximum 7×10^7 V/m compare to the triangle shape that produced maximum 3×10^7 V/m local electric field (figure 4.6.c).

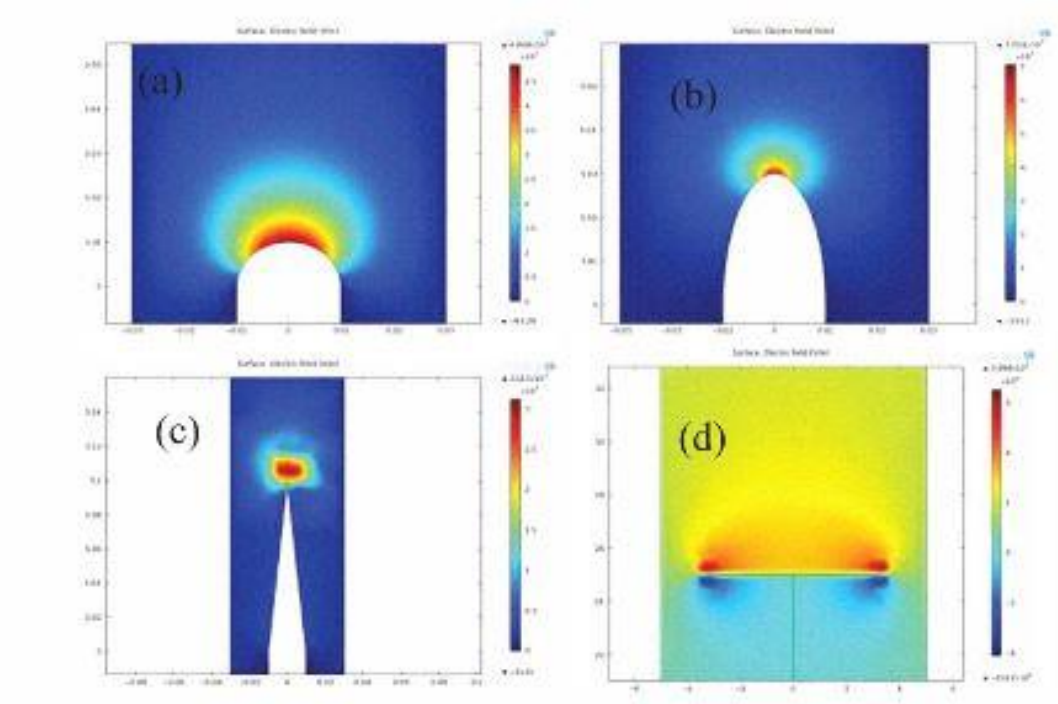

Figure 4. 6 Electric filed density around an individual nanowires. a) hemispherical tip, b) ellipsoid shape tip, c) sharp triangle tip, d) T-shape tip [75]

4.9 Total Field Enhancement of the Devices

As explained in section 4.8, there are several analytical studies reported in literature to calculate field enhancement factor (β) of the nanostructures. These studies mathematically predicted the field enhancement factor of a single protrusion; however, the interpretation of the average field gain coefficient (β_{tol}), considering constructive/destructive interferences of the local

electric field of thousands of nanowires in the whole structure, is desired to optimize the design and structure of the gas sensors.

In field emission based gas sensors, Fowler Nordheim (FN) theory of electron emission from a metallic or semi-metallic roughly predicts β_{tol} based on the field induced emission current and can be experimentally calculated by plotting $\ln(J/V^2)$ against (1/V) where J is the emission current density and V is the applied voltage [76], [77].

In the second approach, this factor can be estimated practically using the slope of the gas discharge graph (I - V characteristics) in the ohmic region of the curves (for field emission gas sensors as well as field ionization tunneling sensors). Figure 4.7 shows different regions of discharge characteristic of gases in a uniform electric field generated between planer parallel plates. Any gas contains free-floating negative electrons and positive ions due to the ionization of the gas atoms by cosmic radiation. In region I of the discharge curve, when the voltage is applied to the electrodes, the traveling radiation-generated charged particles produce current as electrons migrate to the anode and the ions move toward the cathode. The current in this region shows strong electric field dependence and increases as the applied voltage is increased. In this region the discharge current density is expressed as:

$$J_{GIS} = \sigma_{Gas} E_{app} = (n_e \mu_e + n_i \mu_i) e E_{app} \tag{4.20}$$

where σ_{Gas} is the gas conductivity, e the electron charge, E_{app} the applied electric field, n_e and n_i the electron and ion concentrations respectively, and μ_e, and μ_i are the electron and ion mobility respectively.

In saturation region (II), the current reaches its saturated value which means that all radiation-generated particles are attracting to the electrodes. At the last phase the electric field strength would be enough to accelerate the electrons, resulting ionizing collisions. At breakdown

voltage (V_b) the discharge current is self-sustainable and is maintained due to ionizing collisions without any external ionization source.

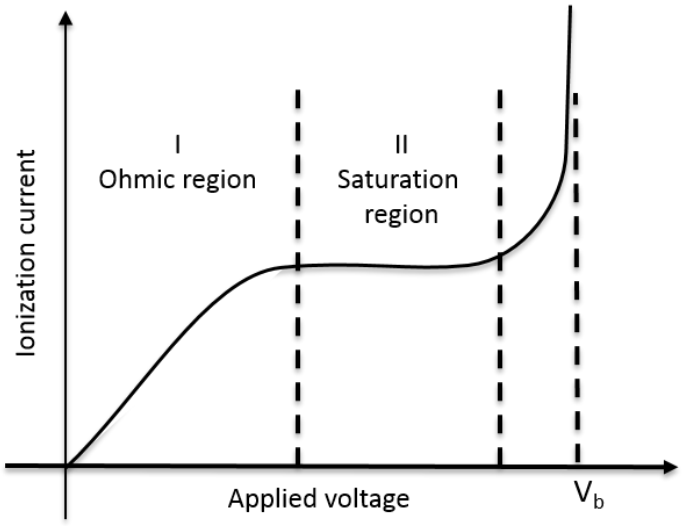

Figure 4. 7 (Reproduced from [3]) I - V characteristics of gas discharge in a uniform electric field.

According to equation (4.20) in the ohmic region, the traveling radiation-generated charged particles produce current proportional to applied field. As in this region there is no ionization-induced current, the current density exclusively depends on the strength of the electric field. The current density of nanowire based gas ionization sensor (J_{GIS}) due to enhanced electric field can be expressed as

$$J_{GIS} = \sigma_{Gas} E_{eff} = (n_e \mu_e + n_i \mu_i) e \beta_{tol} E_{app} \tag{4.21}$$

where E_{eff} is the enhanced electric field and β_{tol} is average field gain coefficient.

By comparing equations (4.20) and (4.21) and considering a constant σ_{Gas}, β_{tol} of gas ionization sensors can be estimated by dividing the slopes of I - V characteristics of the device with a parallel-plates in the ohmic region.

$$\beta_{tol} = \frac{Slope_{GIS}}{Slope_{PPL}} \tag{4.22}$$

where $Slope_{GIS}$ is the slope of I - V discharge graph of the nanowire based GIS and $Slope_{PPL}$ is the slope of the I - V discharge graph of the parallel plate in their ohmic regions.

Chapter 5

Synthesis and Characterization of Gas Ionization Sensor based on the Fabricated Si nanostructures

5.1 Fabrication of the Gas Sensor

Schematic illustration of the proposed gas sensor is presented in figure 5.1. It is made of two parallel electrodes. Nanostructures grown on a silicon wafer is used as one of the plates, the anode, and the cathode is a piece of silicon wafer coated with few micrometers of aluminum. The two plates are separated by pieces of insulating double-sided adhesive tape such a way that there was enough opening between the two electrodes to allow the gas flow between them (d is referred to gas spacing or inter-electrode spacing). The tape should be high temperature resistant as ion bombardment heats up the sensor. Conductive silver epoxy was used to make the wire connections. I-V characterization of the device was performed using HP4155 parameter analyzer. Applied voltage across the device was swept from 0 V to 100 V with 1 V steps and 1 s delay.

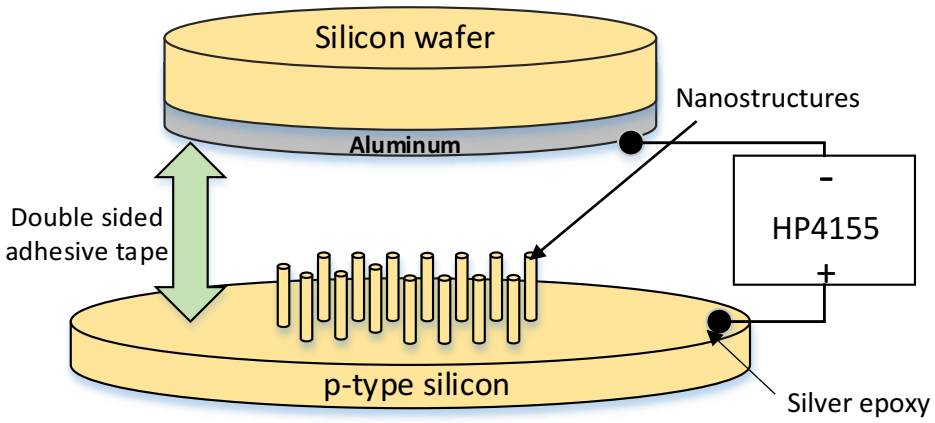

Figure 5. 1 **(**After Abedini Sohi and Kahrizi [34]) Schematic of the fabricated gas sensor device.

The sensor was placed in a gas chamber and the chamber was vacuumed to 10^{-5} Torr before each test. The sensor was tested for oxygen (O_2), helium (He), nitrogen (N_2) and argon (Ar) gases, under pressures from 10^{-2} to 10 Torr.

5.2 Fabrication of the silicon nanostructures (anode electrode)

Details of growing silicon nanowires using chemical/electrochemical technique are previously reported in chapter III. However, we used variety of Si nanowire structures in term of geometry and aspect ratio in GIS fabrication, only a specific structure suits to operate the device. Remarked structures should encompass the lateral edges of the pyramids.

In the first approach samples of p-type (100) silicon wafers (380±10μm thickness with resistivity about 5-10 Ω·cm from Silicon Material Inc.) were cut in 1×1 cm^2 pieces and cleaned using RCA technique. Solution for anisotropic etching, made of equal amount of tetramethylammonium hydroxide (TMAH) and isopropyl alcohol (IPA) (5 wt% each), was used to etch the samples for 20 minutes. The temperature of the solution was kept constant at 90°C

using an oil bath system. A condenser covered the etchant container in order to keep the etchant concentration constant throughout the experiment.

Figure 5.2 shows the SEM image of square based pyramidal structures after anisotropic etching step. According to the figure the average tip-to-tip separation of the large pyramids is about 5μm.

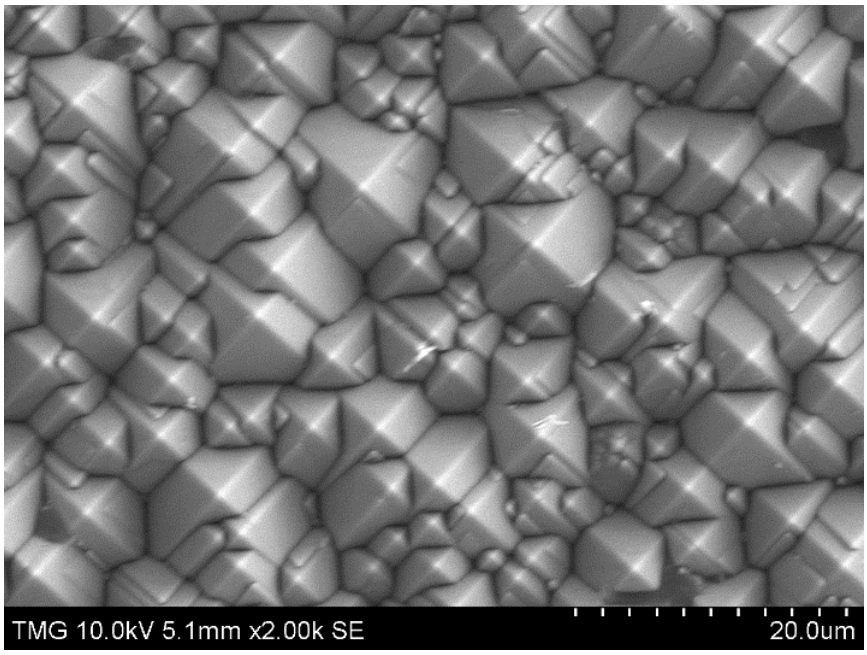

Figure 5. 2 (After Abedini Sohi and Kahrizi [34]) Anisotropic etching of (100) p-type silicon at 90°C for 20 minutes in 5 wt% TMAH and 5 wt% IPA resulted in formation of pyramids that covers the surface completely.

The samples were subsequently exposed to electrochemical isotropic etching. In this step the textured silicon samples, are placed in a two-electrode cell of anodic etching. The etching was done in an electrolyte consisting of 1:3 hydrofluoric acid and ethanol for 70 minutes under a 15 mA/cm^2 applied anodic current density[1]. At this current density porous silicon starts to form by

[1] In this work the potentiostat/galvanostat that has been used to apply anodic current is prinston-273A. This device is following American polarity convention in which negative current is anodic. 15 mA/cm^2 anodic current is provided by applying -15 mA/cm^2 to the working electrode.

electrochemical etching, all around the pyramids. Porosity of silicon depends on anodization conditions such as HF concentration, current density and resistivity of the sample. It is found (and reported in chapter III) that the average pores diameter depends on applied current density and it increases with increasing current density [78], [79]. As it is shown in figure 5.3.a, the pores formation starts at the edges of the pyramids due to the higher hole current density. As the etching continues, the pyramid faces are etched away (shown in Figure 5.3.b), while lateral edges remain unetched. To narrow down the lateral edges, samples are subjected to another anisotropic etching in a weak etchant (low concentration of 1 wt% of TMAH and 1 wt% of IPA) for 30 seconds (it should be noted that this value was 2 minutes to remove the residuals entirely). The final structures are shown in figure 5.4. They have pyramid shapes with lateral edges with the thickness about 100 nm. The grown nanostructures are fairly uniform. This was achieved by texturing silicon surface uniformly in the first step of the fabrication. The structures are separated by almost 5 μm with an average height of 10 μm.

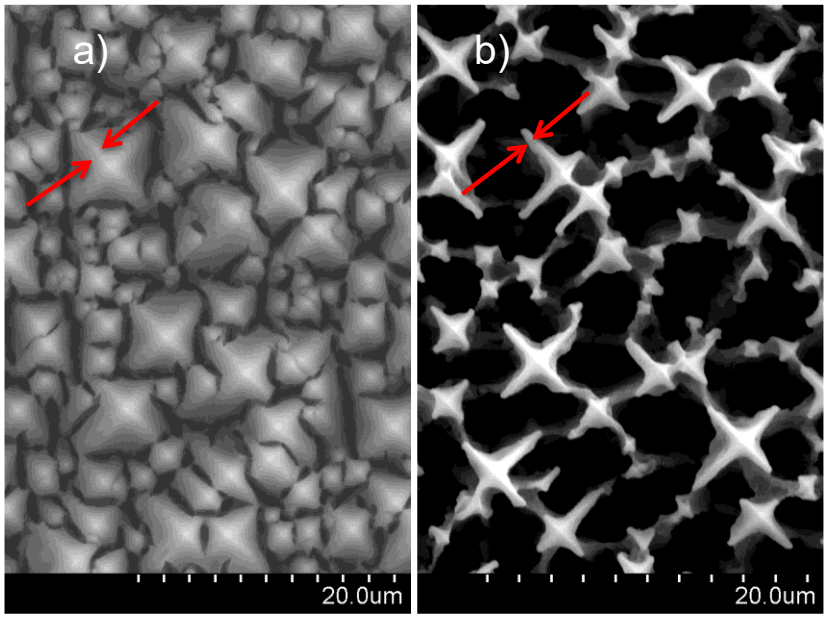

Figure 5. 3 (After Abedini Sohi and Kahrizi [34]) Top view of the electrochemically etched textured silicon. a) After 10 minutes etching: Pore formation starts at pyramid perimeters. b) After 70 minutes etching: Pyramid faces are etched away while lateral edges shown by red arrows remained unetched.

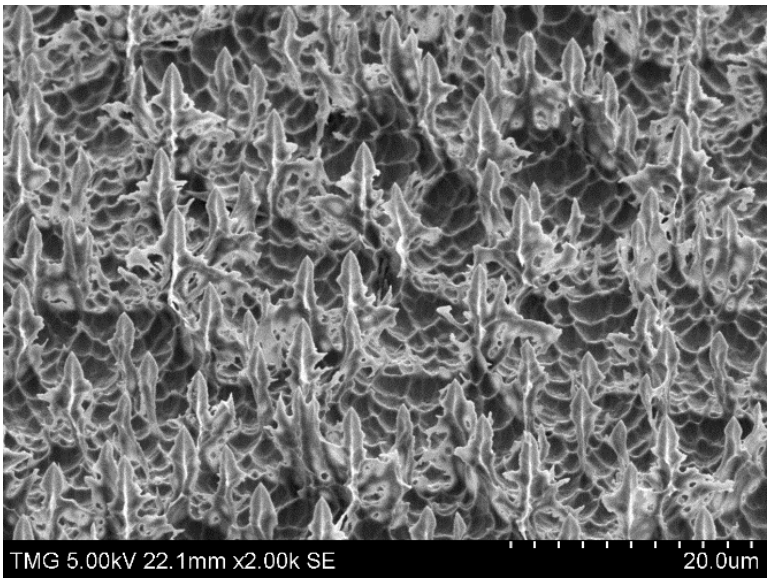

Figure 5. 4 (After Abedini Sohi and Kahrizi [34]) Tilted view of the final nanostructures, illustrates the existence of residual walls around the structures with the thickness of 100 nm

5.3 Measurement Setup

HP 4155A parameter analyzer is the measurement instrument utilized to characterize the gas sensing devices. HP 4155A has four triaxial source-measurement unites (SMU) as shown in figure 5.5. Each SMU can be either in *voltage source and current monitor mode* or *current source and voltage monitor mode.*

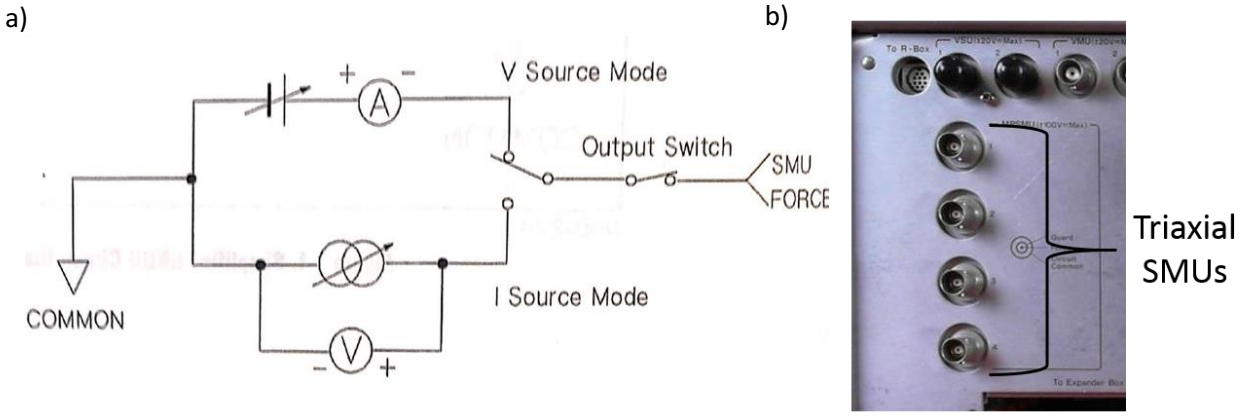

Figure 5. 5 a) Simplified SMU Circuit diagram, b) Rear view of the HP 4155A

SMU#1 and SMU#2 are connected to the anode and cathode respectively. Both SMUs are connected to the device using triaxial cables. These guard shield cables are employed for precise low-current measurements (less than nA) as in this range it is affected by leakage current. Triaxial cables prevents the current leakage by keeping Guard as a low-impedance point in the circuit that is at the same potential as force. Force and Guard have the same voltage thus prevent any leakage current between center conductor and outermost ground. Figure 5.6 compares an un-guarded SMU (connected to coaxial cable) and a guarded SMU using triaxial cable. As it can be seen using coaxial cables the measured current is

$$I_{measurement} = I_{DUT} + I_{leakage} \tag{5.1}$$

Where I_{DUT} is the current of device under test. $I_{leakage}$ is zero in guarded SMUs because the same potentials as the force is applied to the shield through a unity- gain amplifier. As there is no

potential difference between the central conductor and the shield, therefore no leakage current flows through the insulation resistor (R_L).

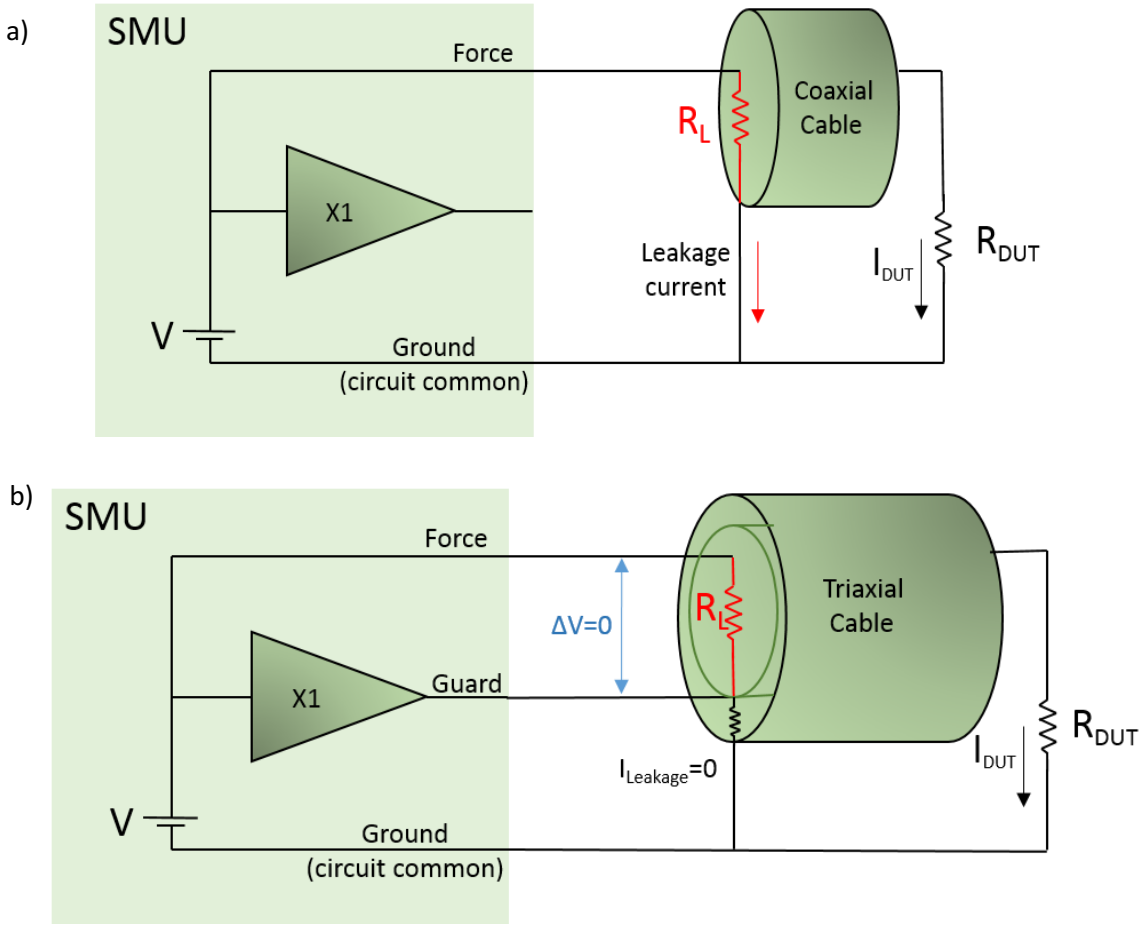

Figure 5. 6 a) Unguarded coaxial cable, b) Guarded triaxial cable

A staircase voltage sweep was applied through SMU#1 from 0 V to 100 V with 1 V steps (note that an individual SMU of HP 4155A is capable of sourcing up to 100 V). At each voltage

a 1 second delay was considered before performing the measurements. A 0 V constant voltage is applied to SMU#2[1]. SMUs set up window is shown in figure 5.7.

[1] Cathode is not grounded as it is desired to have cathode current measurements. Both anode and cathode should show equal currents as generated charged carriers are neutralized through the external circuit. So the cathode is considered as a voltage source to be able to measure its current simultaneously.

Figure 5. 7 a) In sweep measurements mode, both SMUs are considered in voltage mode, SMU#1 is a sweeping source (VAR1 function) while SMU#2 is in constant mode. b) The sweep setup window, in which delay time is 1 second and the sweep stops at the compliance (20 mA).

Sensor characterization was performed in the gas chamber of MagSput-2G2 sputtering machine. This equipment contains a vacuum pump, which provides 10^{-6} Torr vacuum and a gas flow controller that can be connected to various gas tanks. The vent pipe is always connected to nitrogen tank.

There are two connectors inside the chamber as shown in figure 5.8. These concertos are connected to the sensor as shown in the figure. Two custom made adapter were used to connect interior connections to the cables of the SMUs.

Figure 5. 8 Device characterization setup.

5.4 Estimation of β_{tol}

To calculate the total field gain coefficient (β_{tol}) based on equation (4.22), I-V characteristics of a PPL sensor is compared to that of the GITS. The parallel-plates sensor consists of two plates, one perfectly smooth p-type Si wafer as the anode and an aluminum coated Si wafer as the cathode, separated by 100 μm gap. GITS sensor is fabricated as explained in section 5 with the same separation gap of 100 μm between the electrodes.

Ohmic regions of both PPL sensor and fabricated GITS, under vacuumed air (10^{-5} Torr), are shown in figure 5.9. The total enhancement factor of the device is calculated using equation 5.2. Accordingly, the enhancement factor of the device is equal to:

$$\beta_{tol} = \frac{Slope_{GIS}}{Slope_{PPL}} \cup \frac{3 \leftrightarrow 10^{-5}}{8 \leftrightarrow 10^{-9}} = 3,750 \qquad (5.2)$$

Theoretically, no tunneling occurs at electric fields less than 10^9 V/m. The electric filed strength in the parallel plate sensor is in the range of 10^5 to 10^6 V/m according to applied voltage (100 V is the maximum voltage of HP4155-SMU). This value should at least increases by 1000 times to make the tunneling possible. Our estimated value of β_{tol}, indicates that the geometrical field enhancement of fabricated GITS induces the required electric field for the field ionization tunneling.

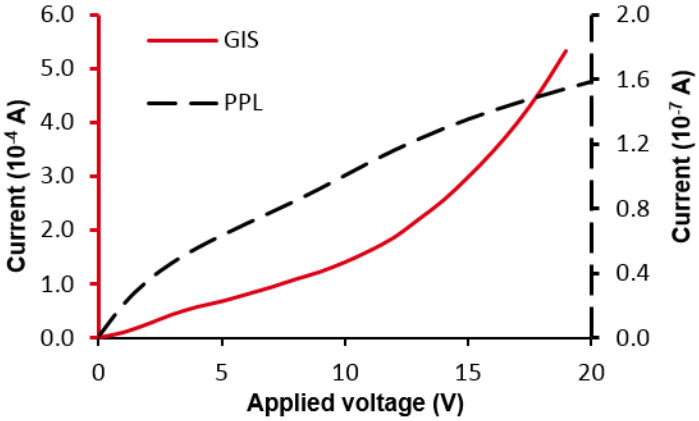

Figure 5. 9 (After Abedini Sohi and Kahrizi [69]) Ohmic regions of the PPL sensor and the fabricated GITS at 10^{-5} Torr vacuumed air. The slopes of the curves are used to calculate the enhancement factor of the system.

5.5 Characterization of the Gas Sensors

Field ionization tunneling tests were performed while separation gap between the electrodes was first set at 200 μm. Figure 5.10 shows I-V characteristic of the gas sensor for Ar, under a pressure of 1×10^{-2} Torr. The figure shows four distinct regions in I-V curve.

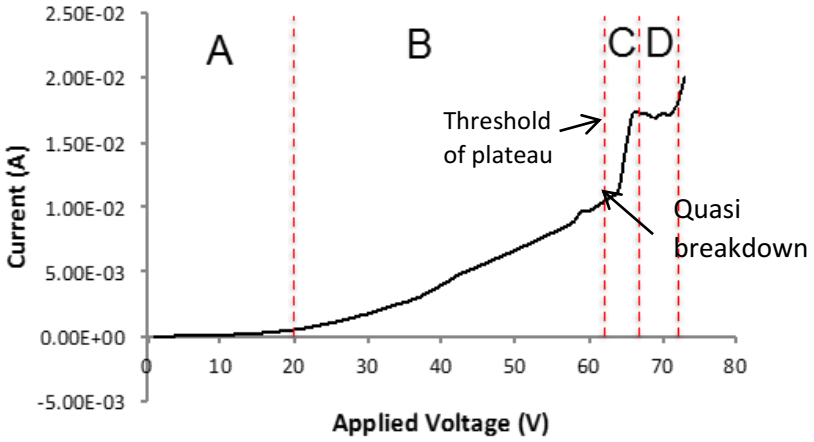

Figure 5. 10 (After Abedini Sohi and Kahrizi [34]) I-V characteristic of the gas sensor for Ar in a pressure of 1×10^{-2} Torr.

Normally due to cosmic ray ionization, the sensor chamber contains number of free charged particles (positive ions and electrons). Applied electric field separates the charges and generates a current proportional to electric field strength. In region A (figure 5.10) the current is due to the electric field-induced charge transport. These charges will get neutralized through the external circuit.

As the applied voltage is increased (region B), electric field at the tip of the nanostructures is higher than ionization threshold, so valence electrons of the gas tunnel through the potential barrier of the gas atoms into the surface states of the nanostructures. As it was explained in

section 1.2.3, according to equation 5.3 tunneling current increases rapidly as the voltage increases.

$$X_c = \frac{U_I - (\varphi + \varphi_s)}{E} \tag{5.3}$$

It is evident from equation 5.3 (parameters are discussed in section 1.2.3) that at high electric fields the critical distance will be reduced, resulting a higher tunneling probability. In region C tunneling current shows a sharp rise at a specific voltage. Electric field at this voltage is sufficiently high; so all particles approaching the tip of the structures become ionized

Cathode electrode bombarded by generated positive ions, induces secondary emissions to amplify the gas ionization, causing a sharp rise of current. However, generated positive-negative charges are not self-sustainable (for this reason we cannot say that complete breakdown has happened, and we call the voltage at this point quasi-breakdown voltage, V_{qbr}), and current reaches a plateau phase (region D) in which the growth rate of current slows down or may even stop. In this region, as large number of ions is suddenly generated at V_{qbr}, the number of positive ions on cathode electrode increases, resulting an internal electric field in opposite direction to the applied electric field. Consequently, the total electric field inside the chamber is reduced to a point where there is no further ionization. Eventually, accumulated positive ions gradually get neutralized and current start increasing again (beyond the region D). To avoid damaging the nanostructures, we have applied limitation to the maximum current between the electrodes.

The existence of V_{qbr} and threshold of current plateau, allows the device to be calibrated to identify the nature of gases.

In order to check the effect of gas pressure on the I-V characteristic of the sensor, the experiment is repeated for Ar and He under various pressures, and the results are shown in figure 5.11. The figures show that the tunneling current (region B, in figure 5.10) is not a function of

the gas pressure and no specific trend can be remareked for this region. The reason is that at low pressures, the concentration of the gas molecules near the structures is independent of gas pressure and mostly depends on the gas properties, such as stickiness and compressibility. Therefore the concentration of electrons that are tunneling through the potential barrier of the nanostructures remains almost the same. On the other hand, as the gas pressure increases, the number of gas molecules will increase, therefore impacts between electrons and gas molecules happens at shorter distances, so electrons must acquire higher energy before the impact, in order to generate secondary emissions. Higher energy means higher electric field between the parallel plates. In other words the applied voltage must be larger. This is quite consistent with our experimental results. As the gas pressure is increased V_{qbr} is increased as it is shown in figure 5.11.

Contrary to region C that is strongly dependent on the gas pressure, region D is independent of gas pressure and only depends on concentration of the generated ions that are accumulated at the surface of the cathode.

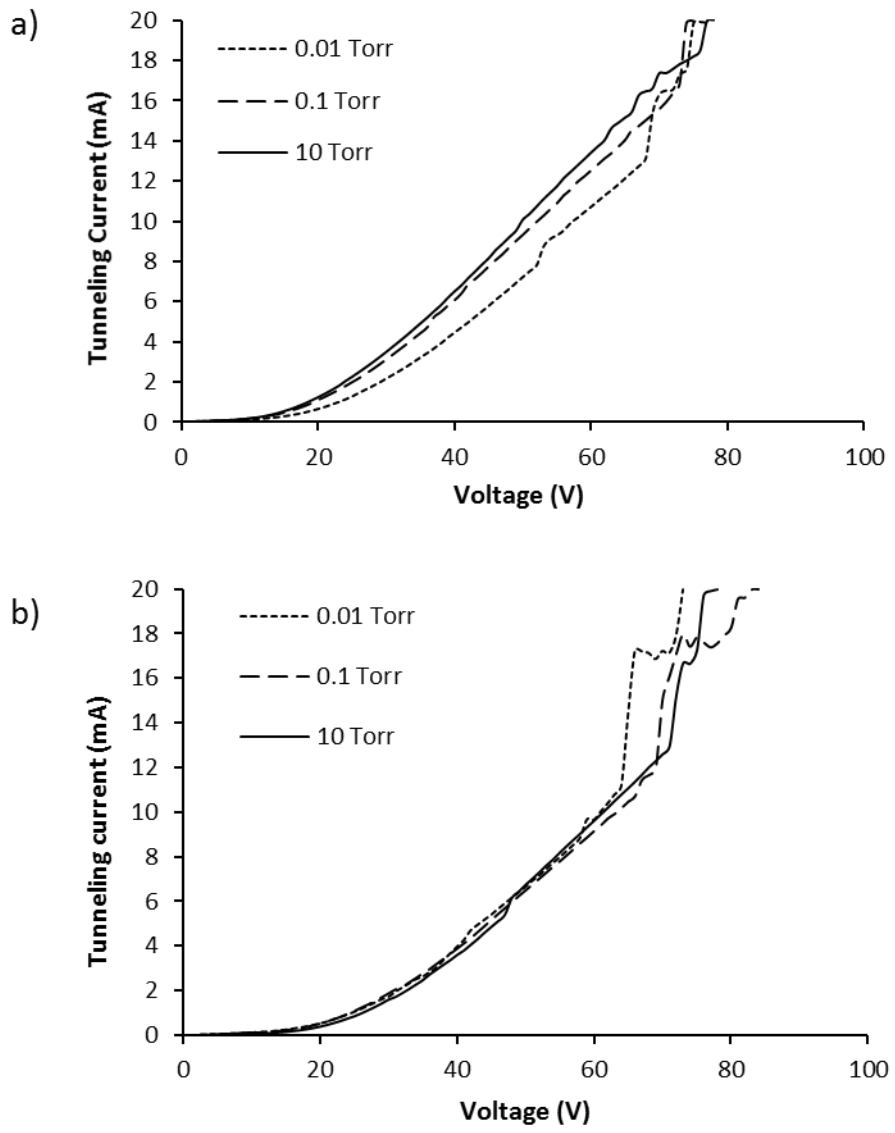

Figure 5. 11 **(**After Abedini Sohi and Kahrizi [69]) I-V characteristics of the device for a) He and b) Ar under different pressures.

The I-V characteristics of the sensor was tested for other gases like He, N_2 and O_2. Figure 5.12 shows the results when the gases were under pressure of 1×10^{-2} Torr. The variation of current with respect to voltage shows the same trend for all gases.

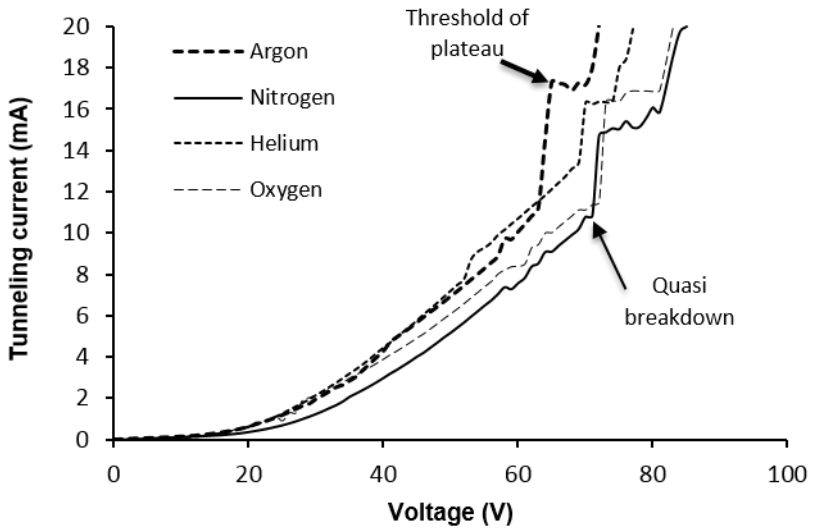

Figure 5. 12 **(**After Abedini Sohi and Kahrizi [69]) I-V characteristics of the device for Ar, N_2, He and O_2 gases under 1×10^{-2} Torr.

In Table 5.1 we have summarized the V_{qbr}, its corresponding current and the threshold plateau for tested gases.

Table 5. 1 Calibrating data at 10^{-2} Torr

Gas	Quasi breakdown voltage (V)	V_{qbr} Corresponding current (A)	Threshold of plateau current (A)
He	68	1.31E-2	1.63E-2
N_2	70	1.08E-2	1.51E-2
O_2	72	1.15E-2	1.64E-2
Ar	62	1.13E-2	1.73E-2

We have further extended our experiments to test the devices with separation gap of 50 μm between the parallel electrodes. Obviously, as the gap is reduced, the electric field will be higher for the same applied voltages, causing the breakdown happens at lower voltages. Figure 5.13 shows the I-V characteristics of the device for considered gases. Due to the narrower gap between the electrodes, ions reach the cathode plate faster, and it is reasonable to suggest that the

ion bombardment heats up the cathode surface, and begins to emit electrons thermionically. The impact of ions with the cathode surface liberates significant number of electrons and the discharge becomes self-sustaining. As a result, as it is shown in figure 5.13, we could observe the breakdown for these gases. No plateau region was detected for these devices, as the inversion of the electric field between the parallel plates was not possible due to the large number of emitted electrons from the cathode surface. The detected breakdown voltages are lower compared to those reported for sensors fabricated using metallic nanowires.

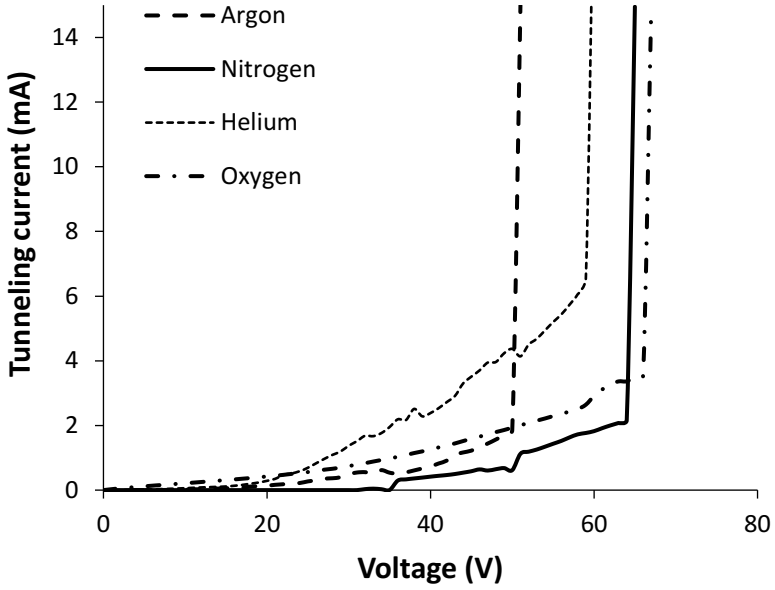

Figure 5. 13 (After Abedini Sohi and Kahrizi [69]) I-V characteristics of sensor for N_2, Ar, He, O_2 gases under 1×10^{-2} Torr with 50 μm separation gap. Gas breakdown happens at lower voltages compared to 200μm gap.

5.6 Conclusion

In this chapter we described design and fabrication of field ionization gas sensor. The sensor is made of silicon nanostructures sandwiched between two parallel plates. The silicon nanostructures with crossed shape (containing lateral edges) are grown on one of the plates using three-step chemical/electrochemical technique. The thickness of the crossed walls is about 100 nm.

The I-V measurements of the device revealed different characteristics when we changed the gap between the plates from 200 to 50μm.

For the devices with gaps of 200μm a quasi-breakdown was observed due to bombardment of the cathode electrode by generated positive ions, which induces secondary emissions and generates gas amplification. Threshold plateau was also observed which was due to accumulation of positive ions near the cathode induces an internal electric field in opposite direction to the external applied field. There would be no more ionization at reduced fields results in a plateau in ionization current.

For the devices with gaps of 50 μm we could observe the complete field ionization breakdown of the several gases. The detected breakdown voltages were much lower compared to those, reported using devices fabricated by metallic nanostructures.

In order to avoid possible damages to the nanostructures, maximum current of 20 mA was allowed through the device during the test operation. The devices were tested for several times for each run. The results were reproducible, and it seems that the nanostructure are quite robust and remain intact inside the device, no damages were observed to the nanostructures.

In this work fabricated Si nanostructures showed tunneling ionization and breakdown properties simultaneously. This can be attributed to the p-type nature of the samples and the ` fabrication technique which retains its original crystalline structure of the bulk silicon.

Chapter 6

Conclusion, Contributions and Future Works

6.1 Conclusion and Contributions

In this work we designed, fabricated and successfully tested a new generation of gas field ionization sensor, which works based on measuring the tunneling field ionization currents of the unknown gas.

This sensor is based on field amplifying element of Si nanostructures to reduce the gas ionization required voltage.

These free-standing nanostructures are fabricated using a cost effective, non-lithography three-step etching technique. This technique was invented and developed in our group, however further research was needed to analytically study the mechanism of formation and development of the structures. The freestanding silicon nanostructures with high aspect ratio are fabricated using a chemical/electrochemical etching technique. (100) silicon samples first are textured, covered with hillocks with pyramid shapes via anisotropic wet etching of the samples in TMAH/IPA solutions. Effects of various combinations of TMAH/IPA on the pyramidal texture of silicon are studied in detail. Then, the textured silicon samples are subjected in an electrochemical etching in HF/Ethanol solution to form the nanostructures. A third step of fine etching of the samples in diluted TMAH/IPA solutions was necessary to remove unexpected residual and un-etched walls between the structures. Effect of various fabrication parameters controlling the length and tip-to-tip separation of the final structures are investigated. For the first time, analytical study was carried out through COMSOL multiphysics simulation software. The pyramidal structure fabricated in the first step of chemical etching is considered as the

simulation geometry to study the anodic etching step. The results revealed that the non-uniform electric field distribution inside the anode electrode is responsible to fabricate arrow shape tip structures.

Fabricated silicon nanostructures were placed between two parallel plates separated by a small gap. The sensor works based on the field ionization tunneling effect. For the first time, it is shown that pure silicon nanostructures can be used for this purpose. The device was tested for Ar, N_2 , O_2 , and He gases in a pressure range of $0.01 < P < 10$ torr. The device demonstrated a distinctive I-V curve and the ionization voltages for the considered gases. Detected breakdown voltages were much lower than those reported in the literature for gas ionization sensors based on metallic nanowires.

6.2 Future Works

The concept of Gas Field Ionization Tunneling Sensor based on self-standing Si nanostructures to detect unknown gases, can be developed further. The investigations can be extended in the following areas:

- As it is expected to obtain more sensitive and stable device with a lower response voltage, it is worth to improve the nanostructures morphology. Based on our findings the structures containing pyramidal lateral edges are suitable to operate the device. These structures resemble freestanding 2D thin walls with approximately 100 nm thicknesses. Therefore, a mask-based etching technique can be used to fabricate uniform arrays of Si thin walls. A rectangular long and narrow mask opening can be used to etch (110) silicon sample anisotropically to create the vertical grooves with {111} sidewalls. The width of the grooves should be designed such a way that facilitate the gas flow into the channels.

- A MEMS based design can be used to reduce the inter-electrode gap to about 10-20 μm to increase the electric field and reduce the ionization voltage. However an extensive research is required to ensure flow of gas particles between the electrodes to generate current.
- The sensing properties and tunneling ionization can be studied in gas mixtures.
- An array of GITSs with various inter-electrode gaps can be used to detect the mixture of the gases with various ionization voltages while the amount of each substance can be determined by comparing the ionization currents of each of the gas detectors.

References

[1] A. Mandelis and C. Christofides, *Physics, Chemistry and Technology of Solid State Gas Sensor Devices*. New York: Wiely, 1993.

[2] G. Korotcenkov, *Handbook of Gas Sensor Materials*, vol. 2. New york: Springer, 2014.

[3] R. B. Sadeghian, "A field effect Gas Sensor based on Self-Standing Nanowire Array," Ph.D thesis, Concordia University, 2007.

[4] J. Homola, *Surface plasmon resonance based sensors*. New york: Springer, 2006.

[5] B. D. Gupta and R. K. Verma, "Surface plasmon resonance-based fiber optic sensors: Principle, probe designs, and some applications," *Journal of Sensors*, pp. 1–12, 2009.

[6] D. Michel, F. Xiao, and K. Alameh, "A compact, flexible fiber-optic Surface Plasmon Resonance sensor with changeable sensor chips," *Sensors and Actuators, B: Chemical*, vol. 246, pp. 258–261, 2017.

[7] D. Zhang, L. Men, Q. Chen, and A. Science, "Microfabrication and Applications of Opto-Microfluidic Sensors," *Sensors*, vol. 11, no. 5, pp. 5360–5382, 2011.

[8] A. K. Sharma and B. D. Gupta, "On the performance of different bimetallic combinations in surface plasmon resonance based fiber optic sensors," *Journal of Applied Physics*, vol. 101, no. 9, 2007.

[9] D. Tosi, S. Poeggel, I. Iordachita, and E. Schena, "Fiber Optic Sensors for Biomedical Applications," *Opto-Mechanical Fiber Optic Sensors*, pp. 301–333, Jan. 2018.

[10] Y. T. Long and C. Jing, "Localized surface plasmon resonance based nanobiosensors.," in *SpringerBriefs in Molecular Science*, New york: Springer, 2014, pp. 63–82.

[11] J. Liang, "Surface Plasmon Resonance: An Introduction to a Surface Spectroscopy Technique," *Journal of Chemical Education*, vol. 87, no. 7, pp. 742–746, 2011.

[12] N. B. Agbor, J. P. Cresswell, M. C. Petty, and A. P. Monkman, "An optical gas sensor based on polyaniline Langmuir-Blodgett films," *Sensors and Actuators, B: Chemical*, vol. 41, no. 1–3, pp. 137–141, 1997.

[13] P. K. Maharana, R. Jha, and P. Padhy, "On the electric field enhancement and performance of SPR gas sensor based on graphene for visible and near infrared," *Sensors and Actuators, B: Chemical*, vol. 207, pp. 117–122, 2015.

[14] A. Nooke *et al.*, "On the application of gold based SPR sensors for the detection of

hazardous gases," *Sensors and Actuators, B: Chemical*, vol. 149, no. 1, pp. 194–198, 2010.

[15] S. Roh, T. Chung, and B. Lee, "Overview of the characteristics of micro- and nano-structured surface plasmon resonance sensors," *Sensors*, vol. 11, no. 2, pp. 1565–1588, 2011.

[16] C. Elosua, I. R. Matias, C. Bariain, and F. J. Arregui, "Volatile organic compound optical fiber sensors: A review," *Sensors*, vol. 6, no. 11, pp. 1440–1465, 2006.

[17] G. Stewart, C. Tandy, D. Moodie, M. A. Morante, and F. Dong, "Design of a fibre optic multi-point sensor for gas detection," *Sensors and Actuators, B: Chemical*, vol. 51, no. 1–3, pp. 227–232, 1998.

[18] J. Shemshad, "Design of a fibre optic sequential multipoint sensor for methane detection using a single tunable diode laser near 1666 nm," *Sensors and Actuators, B: Chemical*, vol. 186, pp. 466–477, 2013.

[19] J. Shemshad, S. M. Aminossadati, and M. S. Kizil, "A review of developments in near infrared methane detection based on tunable diode laser," *Sensors and Actuators, B: Chemical*, vol. 171–172, pp. 77–92, 2012.

[20] G. Schwotzer, I. Latka, H. Lehmann, and R. Willsch, "Optical sensing of hydrocarbons in air or in water using UV absorption in the evanescent field of fibers," *Sensors and Actuators B*, vol. 39, pp. 38–39, 1997.

[21] S. K. Mishra, S. N. Tripathi, V. Choudhary, and B. D. Gupta, "SPR based fibre optic ammonia gas sensor utilizing nanocomposite film of PMMA/reduced graphene oxide prepared by in situ polymerization," *Sensors and Actuators, B: Chemical*, vol. 199, pp. 190–200, 2014.

[22] G. Korotcenkov, *Handbook of Gas Sensor Materials*, vol. 1. New: Springer, 2014.

[23] A. M. Howaston, *An Introduction To Gas Discharges*, Second. Oxford: pergamon press, 1976.

[24] V. a. Lisovskii and S. D. Yakovin, "A modified Paschen law for the initiation of a dc glow discharge in inert gases," *Technical Physics*, vol. 45, no. 6, pp. 727–731, 2000.

[25] W. S. Boyle and P. Kisliuk, "Departure from Paschen's law of breakdown in gases," *Physical Review*, vol. 97, no. 2, pp. 255–259, 1955.

[26] M. Radmilović-Radjenović and B. Radjenović, "An analytical relation describing the

dramatic reduction of the breakdown voltage for the microgap devices," *Europhysics Letters*, vol. 83, no. 2, p. 25001 (1-4), 2008.

[27] A. Modi, N. Koratkar, E. Lass, B. Wei, and P. M. Ajayan, "Miniturized gas ionization sensors using carbon nanotubes," *Nature*, vol. 424, pp. 171–174, 2003.

[28] G. Hui, L. Wu, M. Pan, Y. Chen, T. Li, and X. Zhang, "A novel gas-ionization sensor based on aligned multi-walled carbon nanotubes," *Measurement Science and Technology*, vol. 17, no. 10, pp. 2799–2805, 2006.

[29] Q. Wan, C. L. Lin, X. B. Yu, and T. H. Wang, "Room-temperature hydrogen storage characteristics of ZnO nanowires," *Applied Physics Letters*, vol. 84, no. 1, pp. 124–126, 2004.

[30] S. Spitsina and M. Kahrizi, "ZnO crystalline nanowires array for application in gas ionization sensor," *IECON Proceedings (Industrial Electronics Conference)*, pp. 3997–4002, 2012.

[31] R. B. Sadeghian and M. Kahrizi, "A low voltage gas ionization sensor based on sparse gold nanorods," *Proceedings of IEEE Sensors*, pp. 648–651, 2007.

[32] N. Azmoodeh, N. Chivu, R. B. Sadeghian, and M. Kahrizi, "A silver nanowire based gas ionization sensor," in *Sensors, EUROCON*, 2009, no. 1, pp. 1231–1235.

[33] S. Bader, *solid states physics:surfaces*, 22nd ed. London: Academic Press, 1986.

[34] P. Abedini Sohi and M. Kahrizi, "Low-voltage gas field ionization tunneling sensor using silicon nanostructures," *IEEE Sensors Journal*, vol. 18, no. 15, pp. 6092–6096, 2018.

[35] Y. Ohno, S. Nakamura, and T. Kuroda, "Mechanisms of Field Ionization and Field Evaporation on Semiconductor Surfaces," *Japanese Journal of Applied Physics, Part 1: Regular Papers and Short Notes and Review Papers*, vol. 17, no. 11, pp. 2013–2022, 1978.

[36] R. B. Sadeghian and M. Kahrizi, "A novel gas sensor based on tunneling-field-ionization on whisker-covered gold nanowires," *IEEE Sensors Journal*, vol. 8, no. 2, pp. 161–169, 2008.

[37] S. Spitsina and M. Kahrizi, "Application of Single-Crystalline N-type and P-type ZnO Nanowires in Miniaturized Gas Ionization Sensor," *Sensors and Materials*, vol. 28, no. 1, pp. 43–54, 2016.

[38] M. Esfahani Fard, "Effect of fabrication parameters on porous silicon structure with some

potential applications," Ph.D thesis, Concordia University, 2009.

[39] B. Yaghootkar, M. Amouzgar, and M. Kahrizi, "A novel and low-cost multi-stage approach for the fabrication of silicon nano-structures," *Sensors and Actuators, A: Physical*, vol. 199, pp. 209–215, 2013.

[40] B. Yaghootkar, "A Study of Novel Fabrication Techniques for Development of 3-D Silicon Nano- structure Array," Ph.D thesis, Concordia University, 2014.

[41] S. Spitsina, "Growth, Doping, and Characterization of ZnO Nanowires: Application in a Miniaturized Gas Ionization Sensor," Ph.D thesis, Concordia University, 2013.

[42] E. Garnett and P. Yang, "Light trapping in silicon nanowire solar cells," *Nano Letters*, vol. 10, no. 3, pp. 1082–1087, 2010.

[43] Y. Cui, Z. Zhong, D. Wang, W. U. Wang, and C. M. Lieber, "High performance silicon nanowire field effect transistors," *Nano Letters*, vol. 3, no. 2, pp. 149–152, 2003.

[44] L. Tsakalakos, J. Balch, J. Fronheiser, B. A. Korevaar, O. Sulima, and J. Rand, "Silicon nanowire solar cells," *Applied Physics Letters*, vol. 91, no. 23, 2007.

[45] X. T. Zhou, J. Q. Hu, C. P. Li, D. D. D. Ma, C. S. Lee, and S. T. Lee, "Silicon nanowires as chemical sensors," *Chemical Physics Letters*, vol. 369, no. 1–2, pp. 220–224, 2003.

[46] N. Chivu and M. Kahrizi, "Modeling and Simulation of a Miniaturized Gas Ionization Sensor : Detection of Greenhouse Gases," *Sensors & Transducers*, vol. 153, no. 6, pp. 105–110, 2013.

[47] C. Heitzinger and G. Klimeck, "Computational aspects of the three-dimensional feature-scale simulation of silicon-nanowire field-effect sensors for DNA detection," *Journal of Computational Electronics*, vol. 6, no. 1–3, pp. 387–390, 2007.

[48] Z. Huang, N. Geyer, P. Werner, J. De Boor, and U. Gösele, "Metal-assisted chemical etching of silicon: A review," *Advanced Materials*, vol. 23, no. 2, pp. 285–308, 2011.

[49] X. Li and P. W. Bohn, "Metal-assisted chemical etching in HF/H2O2 produces porous silicon," *Applied Physics Letters*, vol. 77, no. 16, pp. 28–31, 2012.

[50] C. Chartier, S. Bastide, and C. Lévy-Clément, "Metal-assisted chemical etching of silicon in HF–H2O2," *Electrochimica Acta*, vol. 53, no. 17, pp. 5509–5516, 2008.

[51] J. B. Hannon, S. Kodambaka, F. M. Ross, and R. M. Tromp, "The influence of the surface migration of gold on the growth of silicon nanowires.," *Nature*, vol. 440, no. 7080, pp. 69–71, 2006.

[52] A. I. Hochbaum, R. Fan, R. He, and P. Yang, “Controlled growth of Si nanowire arrays for device integration,” *Nano Letters*, vol. 5, no. 3, pp. 457–460, 2005.

[53] E. I. Givargizov, “Fundamental aspects of VLS growth,” *Journal of Crystal Growth*, vol. 31, no. C, pp. 20–30, 1975.

[54] I. Lombardi, A. I. Hochbaum, P. Yang, and C. Carraro, “Synthesis of High Density, Size-Controlled Si Nanowire Arrays via Porous Anodic Alumina Mask,” *American Chemical Society*, no. 16, pp. 988–991, 2006.

[55] M. J.Madou, *fundamentals of microfacrication and nanotechnology, manufacturing techniques.*, 3rd ed. New york: CRC Press, 2012.

[56] B. Yu and L. Qian, “Effect of crystal plane orientation on the friction-induced nanofabrication on monocrystalline silicon,” *Nanoscale Research Letters*, vol. 8, no. 137, pp. 1–8, 2013.

[57] M. J.Madou, *fundamentals of microfabrication and nanotechology, Solid-state Physics, Fluidics and analytical techniques in Micro and Nanotechnology*, 3rd ed. New york: CRC Press, 2012.

[58] J. T. L. Thong, P. Luo, W. K. Choi, and S. C. Tan, “Evolution of hillocks during silicon etching in TMAH,” *Journal of Micromechanics and Microengineering*, vol. 11, no. 1, pp. 61–69, 2001.

[59] J. M. Łysko, “Anisotropic etching of the silicon crystal-surface free energy model,” *Materials Science in Semiconductor Processing*, vol. 6, no. 4, pp. 235–241, 2003.

[60] O. Tabata, R. Asahi, H. Funabashi, K. Shimaoka, and S. Sugiyama, “Anisotropic etching of silicon in TMAH solutions,” *Sensors and Actuators A: Physical*, vol. 34, no. 111, pp. 51–57, 1992.

[61] a. Merlos, M. Acero, M. H. Bao, J. Bausells, and J. Esteve, “TMAH/IPA anisotropic etching characteristics,” *Sensors and Actuators A: Physical*, vol. 37–38, pp. 737–743, 1993.

[62] P. Papet *et al.*, “Pyramidal texturing of silicon solar cell with TMAH chemical anisotropic etching,” *Solar Energy Materials and Solar Cells*, vol. 90, no. 15, pp. 2319–2328, 2006.

[63] L. M. Landsberger, S. Naseh, M. Kahrizi, and M. Paranjape, “On hillocks generated during anisotropic etching of Si in TMAH,” *Journal of Microelectromechanical systems*, vol. 5, no. 2, pp. 106–116, 1996.

[64] D. a. Kim *et al.*, “Structural and optical features of nanoporous silicon prepared by electrochemical anodic etching,” *Applied Surface Science*, vol. 230, no. 1–4, pp. 125–130, 2004.

[65] P. Abedini Sohi and M. Kahrizi, “Controlled growth of freestanding silicon nanostructures with high aspect ratio,” in *IEEE-CCECE*, 2018, pp. 1–4.

[66] P. Abedini Sohi and M. Kahrizi, “Formation Mechanism of Silicon Nanowires Using Chemical / Electrochemical Process,” *IEEE Tranactions on nanotechnology*, vol. 16, no. 3, pp. 507–513, 2017.

[67] R. Chudley and R. Greeno, “Fundamentals of Porous Silicon Preparation,” in *Porous Silicon in Practice Preparation Characterization and Applications*, M. Sailor, Ed. Wiley, 2012, pp. 1–42.

[68] X. G. Zhang, “Morphology and Formation Mechanisms of Porous Silicon,” *Journal of The Electrochemical Society*, vol. 151, no. 1, p. C69, 2004.

[69] P. Abedini Sohi and M. Kahrizi, “Miniaturized Gas Ionization Sensor Based on Field Enhancement Properties of Silicon Nanostructures,” in *Nanostructures*, IntechOpen, 2019, pp. 1–16.

[70] R. L. Smith and S. D. Collinsa, “Porous silicon formation mechanisms,” *Journal of Applied Physics*, vol. 71, no. April, pp. R1–R22, 1992.

[71] D. Xiao, *Gas Discharge and Gas Insulation*, vol. 6. New york: Springer, 2016.

[72] L. P. Babich and T. V Loˇ, “Generalized Paschen ’ s Law for Overvoltage Conditions,” *IEEE Transactions on Plasma Science*, vol. 44, no. 12, pp. 3243–3248, 2016.

[73] H. C. Miller, “Change in field intensification factor β of an electrode projection (whisker) at short gap lengths,” *Journal of Applied Physics*, vol. 38, pp. 4501–4504, 1967.

[74] R. G. Forbes, C. Edgcombe, and U. Valdrè, “Some comments on models for field enhancement,” *Ultramicroscopy*, vol. 95, pp. 57–65, 2003.

[75] N. Chivu and M. Kahrizi, “Design , Modeling and Simulation of a Miniaturized Gas Ionization Sensor : Optimization of the Structure and Operation,” in *IEEE-ICIT*, 2012, pp. 178–183.

[76] R. Zou, G. He, K. Xu, Q. Liu, Z. Zhang, and J. Hu, “ZnO nanorods on reduced graphene sheets with excellent field emission, gas sensor and photocatalytic properties,” *Journal of Materials Chemistry A*, vol. 1, no. 29, pp. 8445–8452, 2013.

[77] J. C. Charlier *et al.*, “Enhanced Electron Field Emission in B-doped Carbon Nanotubes,” *Nano Letters*, vol. 2, no. 11, pp. 1191–1195, 2002.

[78] J. Peckham and G. T. Andrews, “Effect of anodization current density on pore geometry in macroporous silicon,” *Semiconductor Science and Technology*, vol. 28, no. 10, p. 105027, 2013.

[79] O. Bisi, S. Ossicini and L. Pavesi, “Porous silicon: a quantum sponge structure for silicon based optoelectronics,” *Surface Science Reports*, vol. 38, no. 1, pp. 1–126, 2005.